Physics-Based Modeling of Direct Coupled Hybrid Energy Storage Modules in Electrified Vehicles

PHYSICS-BASED MODELING OF DIRECT COUPLED HYBRID ENERGY STORAGE MODULES IN ELECTRIFIED VEHICLES

BY

RAN GU, B.Sc., M.S.

A THESIS

SUBMITTED TO THE DEPARTMENT OF ELECTRICAL & COMPUTER ENGINEERING

AND THE SCHOOL OF GRADUATE STUDIES

OF MCMASTER UNIVERSITY

IN PARTIAL FULFILMENT OF THE REQUIREMENTS

FOR THE DEGREE OF

DOCTOR OF PHILOSOPHY

Doctor of Philosophy (2016) McMaster University

(Electrical & Computer Engineering) Hamilton, Ontario, Canada

TITLE:	Physics-Based Modeling of Direct Coupled Hybrid Energy Storage Modules in Electrified Vehicles
AUTHOR:	Ran Gu B.Sc., (Electrical Engineering) Beijing Information Science and Technology University, Beijing, China M.S., (Electrical Engineering) Illinois Institute of Technology, Chicago, United States
SUPERVISOR:	Dr. Ali Emadi
NUMBER OF PAGES:	xxiii, 210

To my parents Wen Gu and Chaomei Xie

Abstract

In this thesis, a physics-based single particle modeling is presented to analyze a proposed direct coupled hybrid energy storage modules using lithium-ion battery and ultracapacitor.

Firstly, a state of the art for the energy storage system in the electrified vehicles are summarized. Several energy storage elements including lead-acid battery, nickel-metal hydride battery, lithium-ion battery, ultracapacitor, and lithium-ion capacitor are reviewed. Requirements of the energy storage systems in electric, hybrid electric, and plug-in hybrid electric vehicles are generalized. Typical hybrid energy storage system topologies are also reviewed. Moreover, these energy storage elements and hybrid energy storage system topologies are compared to the requirements of the energy storage systems in terms of specific power and specific energy.

Secondly, the performance of different battery balancing topologies, including line shunting, ring shunting, synchronous flyback, multi-winding, and dissipative shunting are analyzed based on a linear programming methodology. As a traction battery in an electric or plug-in electric vehicle, high voltage lithium-ion packs are typically configured in a modular fashion, therefore, the analysis considers the balancing topologies at module level and cell level and focuses on minimum balancing time, minimum plug-in charge time, minimum energy loss, and component counts of every balancing

topology for the entire battery pack.

Thirdly, different modeling techniques for the lithium-ion battery and ultracapacitor are presented. One of the main contributions of this thesis is the development of a physics-based single particle modeling embedded with a solid-electrolyte interface growth model for a lithium-ion battery in battery management system. This development considers the numerical solution of diffusion equation, cell level quantities, parametrization method, effects of number of shells in a spherical particle, SOC-SOH estimation algorithms, and aging effects. The accuracy of the modeling is validated by experimental results of a Panasonic NCR18650A lithium-ion battery cell.

Fourthly, the physics-based modeling is applied to analyze the performance of a proposed direct coupled hybrid energy storage module topology based on the Panasonic NCR18650A lithium-ion battery and Maxwell BCAP0350 ultracapacitor. There are many ways to directly connect battery cells and ultracapacitor cells in a module which would influence the performance of the module. The results show that a module has 9 cells in a battery string and 14 cells in an ultracapacitor string can obtain the highest power capability and utilize the most of the energy in an ultracapacitor. More ultracapacitor strings connected in parallel would increase the power density but reduce the energy density. Moreover, the simulation and experimental results indicate that the direct coupled hybrid modules can extend the operating range and slow the capacity fade of lithium-ion battery. An SOC-SOH estimation algorithm for the hybrid module is also developed based on the physics-based modeling.

Finally, a pack design methodology is proposed to meet U.S. Advanced Battery Consortium LLC PHEV-40, power-assist, and 48V HEV performance targets for the

battery packs or the proposed direct coupled topologies. In order to explore replacement tradeoffs between the battery and ultracapacitor, a case study of the direct coupled topologies is presented. From the case study, ultracapacitors enhance the power capability for short term pulse power and marginally reduce the cost of an entire energy storage system. Moreover, the hybrid module topologies can keep a relatively long all-electric range when the batteries degrade.

Acknowledgements

I would like to express my gratitude to my advisor Dr. Ali Emadi for his guidance, support, and encouragement throughout my four years' Ph.D. research at McMaster University.

I convey special acknowledgment and gratitude to Dr. Pawel Malysz and Dr. Hong Yang for their advice, support, and suggestions. I also would like to thank all my colleagues in McMaster Automotive Resource Centre (MARC) for their accompaniment and concerns. Especially I would like to appreciate Jin Ye, Fei Peng, Deqiang Wang, and Weizhong Wang for their help during my research.

This research was undertaken, in part, thanks to funding from the Canada Excellence Research Chairs Program.

Finally, special thanks must go to my family and my parents for their support and understanding during my four years' Ph.D. research experience.

Notation and abbreviations

Symbol/Acronym	Description
A	Electrode plate area (m^2)
a_i, i=p, n	Specific surface area of electrode (m^2/m^3)
$c_{e,i}$, i=p, s, n	Lithium ion concentration in electrolyte phase (mol/m^3)
$\bar{c}_{s,i}$, i=p, n	Average lithium ion concentration of spherical particle in SPM (mol/m^3)
$c_{s,i}^m$, i=p, n	Lithium ion concentration on the m^{th} shell of spherical particle in SPM (mol/m^3)
$c_{s,i}^{surf}$, i=p, n	Lithium ion concentration on surface of spherical particle in SPM (mol/m^3)
$c_{s,i}$, i=p, n	Lithium ion concentration in solid phase (mol/m^3)
$c_{s,max,i}$, i=p, n	Maximum lithium ion concentration in the solid phase (mol/m^3)
$D_{eff,i}$, i=p, s, n	Diffusion coefficient in the electrolyte phase (m^2/s)
$D_{s,i}$, i=p, n	Diffusion coefficient in the solid phase (m^2/s)
F	Faraday's constant (C/mol)
I	Input current (A)

j_i, i=p, n	Molar flux of lithium ions $(mol/(m^2 s))$
$k_{f,s}$	Reaction rate for side reaction (m/s)
$k_{eff,i}$, i=p, s, n	Effective ionic conductivity of the electrolyte (S/m)
k_i, i=p, n	Reaction rate
L_i, i=p, s, n	Length of the three cell dimension layers (m)
M_{SEI}	Molecular weight of SEI (kg/mol)
r	Radial coordinate (m)
R	Universal gas constant $(J/(molK))$
R_f	Internal resistance (Ω)
$R_{s,i}$, i=p, n	Radius of the spherical particle (m)
T	Absolute temperature (K)
U_i, i=p, n	Open circuit potential of electrode (V)
V_{cell}	Terminal voltage (V)
x	Spatial coordinate (m)
ε_i, i=p, n	Porosity of electrolyte phase
$\varepsilon_{s,i}$, i=p, n	Volume fraction of the solid phase
η_i, i=p, n	Overpotential (V)
κ_{SEI}	SEI ionic conductivity (S/m)
ρ_{SEI}	SEI density (kg/m^3)
$\sigma_{eff,i}$, i=p, n	Effective conductivity (S/m)
$\phi_{e,i}$, i=p, n	Potential of electrolyte phase (V)
$\phi_{s,i}$, i=p, n	Potential of solid phase (V)

BMS	Battery management system
ESS	Energy storage system
DAE	Differential algebraic equation
DRA	Discrete-time realization algorithm
ECM	Equivalent circuit model
EDLC	Electrochemical double layer capacitor
EKF	Extended Kalman filter
ESPM	Enhanced single particle model
FDM	Finite difference method
HESS	Hybrid energy storage system
HPPC	Hybrid pulse power characterization
HSPM	Hybrid single particle model
ODE	Ordinary differential equation
PDE	Partial differential equation
POD	Proper orthogonal decomposition
POM	Proper orthogonal mode
P2D	Pseudo-two dimensional
SEI	Solid-electrolyte interface
SLI	Starting, lighting, ignition
SOC	State of charge
SOH	State of health
SPM	Single particle model

SVD	Singular value decomposition
VRLA	Valve-regulated lead-acid

Contents

List of Figures

Chapter 1

Introduction

1.1 Motivation

With high economic growth, air pollution and energy consumption are primary environmental challenges facing the world. According to United States Environmental Protection Agency's investigation (EPA, 2016), 26% U.S. greenhouse gas emissions in 2014 are from transportation when burning fossil fuel which is the second largest sector of U.S. greenhouse gas emissions after the electricity sector as show in Fig. 1.1.

Due to the limited gains in fuel efficiency and increased demand for travel, greenhouse gas emissions from transportation in 2014 is higher 17% than 1990 as shown in Fig. 1.2. However, there was a turning point in 2005 that greenhouse gas emissions from transportation began to decrease due to the higher fuel economy standard. According to (Emadi, 2011), the most practical sustainable solution for greenhouse gas emissions from transportation is that replace petroleum based transportation by electrified vehicles. Using electric or hybrid vehicles can generate energy with non-fossil fuels or lower-carbon and improve fuel efficiency by storing energy from braking

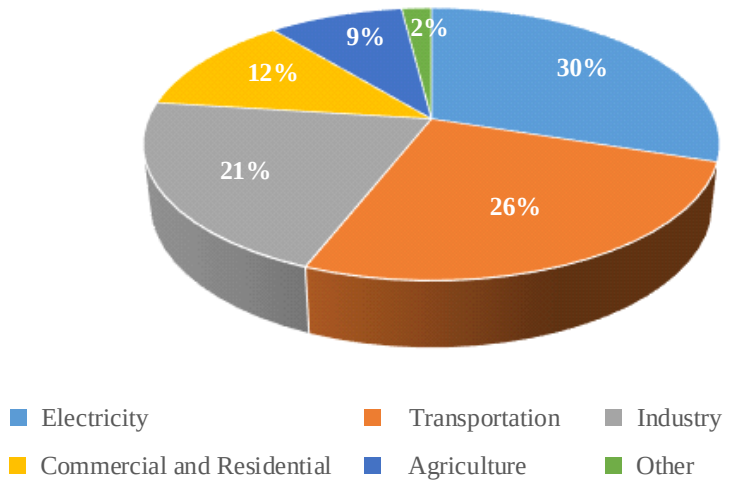

Figure 1.1: Total U.S. Greenhouse Gas Emissions by Economic Sector in 2014 (EPA, 2016)

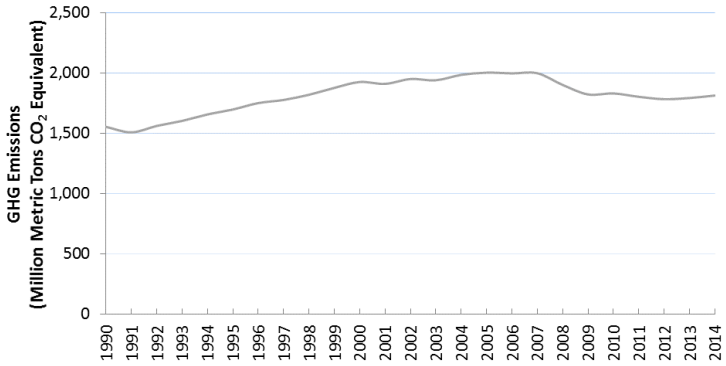

Figure 1.2: Greenhouse gas emissions from transportation sector (EPA, 2016)

and reducing engine-idling (Metz *et al.*, 2007). Even though there are emissions of EV and PHEV from the electricity which is the largest sector of U.S. greenhouse gas emissions, overall emissions of electrified vehicles are still lower than gasoline vehicles. Fig. 1.3 compares annual emissions of EV, PHEV, HEV, and gasoline which include emissions from vehicle and electrical power.

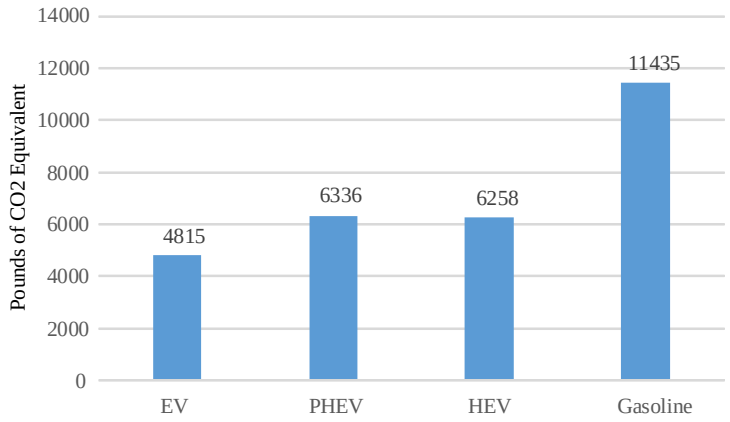

Figure 1.3: Annual Emissions per Vehicle (Elgowainy *et al.*, 2009)

To become strong competitors when compared with gasoline vehicles, an energy storage system plays an important role in an electrified vehicle powertrain which is also a bottleneck of recently electrified vehicle technologies. An energy storage system (ESS) needs the capability to not only store a large amount of energy for a long distance travel but also absorb the regenerative braking power and supply the accelerating power. Unfortunately, recent energy storage technologies are difficult to satisfy the energy and power requirements of energy storage systems in electrified vehicles appropriately. The poor power density of battery always leads to an oversized energy storage system. For an energy storage system using battery cells, even though

this system has achieved the energy target, the system needs more battery cells to meet the power requirement. Oversized energy storage systems lead to the high cost of electrified vehicles. From (Kochhan *et al.*, 2014; Simpson and Markel, 2006), about $40\% \sim 60\%$ of the cost of an electric vehicle or a plug-in hybrid vehicle is from the battery pack. In a hybrid vehicle, around 30% of the cost is from the battery pack.

To avoid an oversized ESS, a hybrid energy storage system which combines two or multiple sources is widely researched. Common options for a hybrid energy storage system (HESS) are battery and ultracapacitor. The battery can store enormous energy as the high energy density storage device. The ultracapacitor has high power density and presents the feature of long lifespan.

Many studies investigated different HESS configurations. In (Dougal *et al.*, 2002; Lukic *et al.*, 2006), a battery pack is directly connected with an ultracapacitor pack in parallel. Advantages of this topology are easy to implement, no power electronic circuit and control strategies are needed. The major drawback of this topology is that the energy stored in the ultracapacitors cannot be effectively utilized. In practice, this system needs more external circuit to protect these two packs.

In (Cao and Emadi, 2011; Gu *et al.*, 2015b; Khaligh *et al.*, 2009; Li *et al.*, 2009; Onar and Khaligh, 2008; Ortuzar *et al.*, 2007; Solero *et al.*, 2005; Tu and Emadi, 2012), one or multiple bi-directional DC/DC converters are involved into the battery pack and ultracapacitor pack for optimizing the power split between them. In (Cao and Emadi, 2011; Gu *et al.*, 2015b; Onar and Khaligh, 2008; Ortuzar *et al.*, 2007; Tu and Emadi, 2012), a bidirectional DC/DC converter is used to interface the battery pack and the ultracapacitor pack. In (Li *et al.*, 2009; Solero *et al.*, 2005), both of battery pack and ultracapacitor pack are connected to the DC link in parallel

by using two independent DC/DC converters. To simplified and reduced the cost of the multiple converters configuration, multiple-input converter configuration is proposed in (Khaligh *et al.*, 2009). These topologies can control the power flow to meet the power requirement but increase the size of the system, cost, mass, and control complexity.

Besides the passive HESS and active HESS on pack level, a lithium-ion capacitor which combines a lithium-ion with the cathode of an electric double-layer capacitor in a cell has commercialized (Ronasmans and Lalande, 2015). The energy density of this hybrid electrochemical energy storage device is two to three times higher than conventional ultracapacitor (Omar *et al.*, 2012). However, the energy density of it is still much lower than a lithium-ion battery.

Inspired by the principle of the lithium-ion capacitor, this thesis focuses on combining battery cells and ultracapacitor cells at the cell level. Firstly, an active hybrid module is proposed which connects one battery and one ultracapacitor through a half-bridge DC-DC converter. Although this topology can improve the performance of the battery and prolong battery's lifespan, the complicated topology and control strategy are not suitable for a large energy storage system. Then the thesis proposes a hybrid energy storage module designs employing lithium-ion battery cells direct coupled with ultracapacitor cells. Combining batteries and ultracapacitors at the cell level increases the utilization efficiency of ultracapacitors and does not need the complicated power electronic circuits to control the power flow. Taking advantages of the ultracapacitor, the power capability of the hybrid module is increased, operating range is wider and lifespan is prolonged.

In order to obverse the influences and aging effects of a lithium-ion battery with

coupled ultracapacitors, an accurate battery model is needed. Common modeling techniques for lithium-ion batteries are categorized into equivalent circuit model (ECM), empirical model, and physics-based model (Seaman *et al.*, 2014). ECM approximates the performance of the battery by several resistor-capacitor networks. Due to simplicity and low computational complexity, ECMs are widely used for the online state of charge (SOC) and state of health (SOH) estimation and control applications. To approximate high dynamic electrochemical processes and aging effects, ECM needs to be extended to higher orders (more RC pairs). Many look-up tables are needed for parameters in this model dependent on SOC, temperature, current amplitude, and current direction. Fig. 1.4 presents a structure of an n-RC pair ECM with changing parameters dependent on SOC and temperature. Moreover, the RC pairs cannot accurately represent physics and electrochemical phenomena.

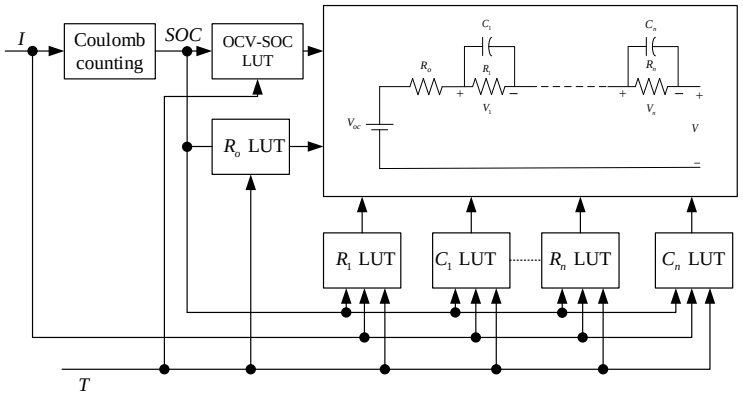

Figure 1.4: An nRC pairs ECM which considers parameters of it are changing dependent on SOC and temperature

Unlike the equivalent circuit model using look-up tables, empirical models describe the behavior by using various functions and formulas. Since these models employ past experimental data, predictions may be poor for other battery operating

conditions (Plett, 2004; Ramadesigan *et al.*, 2012).

As a model in an advanced battery management system, the physics-based model is expected to replace the equivalent circuit model for observing and estimating states and properties of the battery as the battery ages (Chaturvedi *et al.*, 2010; Rahn and Wang, 2013; Seaman *et al.*, 2014). To describe internal electrochemical processes in the lithium-ion battery, several coupled differential equations compose a nonlinear pseudo-two dimensional (P2D) model (Doyle *et al.*, 1993, 1996; Fuller *et al.*, 1994). There are more than 20 parameters in the P2D model. High computational cost and parametrization are challenges for using the physics-based model in a BMS in real-time. In (Ahmed *et al.*, 2014a,b; Baba *et al.*, 2014; Boovaragavan *et al.*, 2008; Cai and White, 2009; Dao *et al.*, 2012; Domenico *et al.*, 2008, 2010; Forman *et al.*, 2011; Guo *et al.*, 2011; Leea *et al.*, 2012a,b; Rahimian *et al.*, 2013; Smith *et al.*, 2007, 2008; Subramanian *et al.*, 2005, 2007, 2009), several reduced order models are proposed. Different methods are utilized to solve or approach differential equations in the P2D model in (Boovaragavan *et al.*, 2008; Cai and White, 2009; Dao *et al.*, 2012; Forman *et al.*, 2011; Leea *et al.*, 2012a,b; Smith *et al.*, 2007, 2008; Subramanian *et al.*, 2005, 2007, 2009). In (Ahmed *et al.*, 2014a,b; Baba *et al.*, 2014; Domenico *et al.*, 2008, 2010; Guo *et al.*, 2011; Kemper and Kum, 2013; Lee *et al.*, 2011; Rahimian *et al.*, 2013), the structure of the P2D model is simplified to a single particle model(SPM) or an enhanced single particle model. In (Lin *et al.*, 2013; Ramadass *et al.*, 2004; Safari *et al.*, 2009), the solid-electrolyte interface (SEI) layer growth phenomena is modeled and used as an aging mechanism to model battery impedance growth and capacity fade.

This thesis utilizes the single particle model with SEI layer growth model to observe internal states of a battery cell and a battery cell in the direct coupled hybrid energy storage modules. Contributions for the lithium-ion battery physics-based modeling are the development of SPM for BSM in terms of the numerical solution of the diffusion equation in SPM, sensitivity on the numerical solution accuracy with a different number of shell partitions and a new parameterization method for SPM. Through experimental results validation, the mean absolute error (MAE) of the single particle model for an NCR18650A cell can achieve 3.811mV under UDDS drive cycle. For the direct coupled hybrid module, the single particle model for the battery is combined with the equivalent circuit model for the ultracapacitor. The mean absolute error of the hybrid module model can achieve 4.5mV. It needs to emphasize that this model in the thesis focuses on the internal states of a battery at room temperature (25^oC). Therefore, the effects of different temperatures on the lithium-ion battery are not considered.

The number of battery cells and ultracapacitor cells and connection topologies will influence the performance of the hybrid module. Based on the accurate physics-based modeling, different combinations of hybrid modules are analyzed in the time domain and frequency domain. Due to the passive connection, the voltage of battery and ultracapacitor branches should be matched. The number of battery cells in series and number of ultracapacitor cells in series affect the energy utilization ratio of the ultracapacitor and power capability of the hybrid module. For a hybrid module consists of NCR18650A battery cell and BCAP0350 ultracapacitor cell, the optimal combination is 9 battery cells in series and 14 ultracapacitor cells in series which can utilize 65% energy of an ultracapacitor. To improve the power density of the hybrid module,

more ultracapacitor cells in parallel are needed. However, more ultracapacitor strings will reduce the energy density of the hybrid module.

Another advantage is that the hybrid module can prolong the lifespan of the battery since the ultracapacitor cells can receive higher regenerative current pulses which thicken the SEI layer and lead to the capacity fade. The SEI layer growth model in the single particle model is built and compared to the experimentally observed capacity fade and resistance growth.

An energy management system in automotive applications needs to estimate SOC and SOH of the energy storage devices. For the equivalent circuit model, recursive least squares and derivatives of Kalman filter are popular algorithms for online battery state estimation (Malysz *et al.*, 2016). For a nonlinear physics-based modeling, Santhanagopalan (Santhanagopalan and White, 2006) used EKF to estimate SOC of a simplified SPM which used an average value instead of internal states of each electrode. Di Domenico (Domenico *et al.*, 2008) focused on the difference between the open circuit voltage of positive and negative electrodes and estimated SOC by focusing on the positive electrode. In this research, a hybrid SPM (HSPM) which has strong observability with EKF is proposed for SOC estimation. To estimate SOH of battery, the internal impedance is estimated by EKF which is integrated into the SOC estimation EKF. For the hybrid modules, a corresponding SOC and SOH estimation algorithm without additional current sensors is also developed and validated by experimental results.

To explore the replacement tradeoffs between battery and UC cells, a direct coupled hybrid energy storage system pack design methodology is proposed and used in a case study for energy storage systems of PHEV-40, full HEV, and 48V mild HEV.

Hybrid modules have higher power capability, especially for a short term power pulse. The energy utilization efficiency is also increased which is helpful to offset the oversize. The cost of an energy storage system could be marginally reduced and weight is similar to a battery pack, even though the energy specific cost and weight of an ultracapacitor cell are much higher than a lithium-ion battery. A battery pack and a direct coupled HESS pack which are designed for PHEV-40 are tested under UDDS and HWY driving cycles based on simulation. Comparative analysis results illustrate that the HESS pack significantly extends the all-electric range when the battery cells are aged. Therefore, the replacement cost could be also reduced.

1.2 Contributions

The author has contributed to a number of original developments in physics-based modeling for lithium-ion battery and performance analysis of the developed direct coupled hybrid energy storage module. These contributions are briefly described below.

1. The performance of battery pack balancing topologies at the module and cell levels are analyzed by using linear programming; published in (Gu *et al.*, 2015a).

2. A single particle model (SPM) with the solid-electrolyte interface (SEI) growth model of lithium-ion battery is developed for BMS in terms of the numerical solution of the diffusion equation, definitions of cell level quantities, parametrization method, effects of the number of shells in a spherical particle, and SOC-SOH joint estimation algorithm; submitted in (Gu *et al.*, 2016b).

3. The single particle model is applied to analyze the performance and SEI growth

of an active hybrid module which connects a battery cell and an ultracapacitor cell through a bidirectional DC-DC converter under driving cycles; published in (Gu *et al.*, 2015b).

4. A direct coupled hybrid energy storage module and its corresponding SOC-SOH estimation algorithms are proposed and analyzed based on the single particle model with SEI growth model;

5. A pack design methodology is proposed to meet USABC performance targets using battery and ultracapacitor energy storage elements in direct coupled topologies; accepted for publication in (Gu *et al.*, 2016a).

1.3 Outline of the Thesis

Chapter 2 briefly introduces state of the art of the energy storage system and hybrid energy storage system in the electric vehicles. The features of different types of batteries and electric double-layer capacitors are presented and compared with the requirement of energy storage systems in the electrified vehicles. To compensate drawbacks of these energy storage devices by each other, the architectures of the hybrid energy storage systems which combine the batteries and electric double-layer capacitors in different topologies are reviewed.

Chapter 3 analyzes the performance of battery pack balancing topologies at the module and pack levels. The design of a battery pack is typically performed in a modular fashion where multiple cells in series form modules and multiple modules are connected in series to achieve desired pack voltage. Two-level balancing topologies comprised of combinations of line shunting, ring shunting, synchronous fly-back,

multi-winding, and dissipative shunting are considered in the analysis. Aspects of battery pack balancing performance, such as minimum balancing time, minimum plug-in charge time, and minimal energy loss in balancing are calculated using linear programming. Component counts of each pack design topology are also compared.

Chapter 4 presents different modeling techniques for the lithium-ion battery and ultracapacitor. For the lithium-ion batteries, the equivalent circuit modeling and physics-based modeling techniques are introduced. The lithium-ion battery equivalent circuit models have been widely used due to the simple structure. The physics-based approaches enable modeling of internal electrochemical processes within the lithium-ion cell. Several reduced order physics-based modeling approaches amenable for online battery state estimation are reviewed in this chapter. In particular, aging effects such as the solid-electrolyte-interface layer growth is modeled. The single particle model method is extended using the following novelties: 1) numerical solution of the diffusion equation in the solid phase, 2) sensitivity on the numerical solution accuracy considering the number of shell partitions, 3) a new parameterization method that identifies pertinent parameters, 4) state-of-charge and state-of-health estimation algorithms based on hybrid SPM (HSPM), and 5) validations of SPM and HSPM based estimation algorithms using drive cycle data.

Chapter 5 analyzes performance of an active hybrid energy storage system and a direct coupled hybrid energy storage module based on the single particle model. Combining with ultracapacitors improves power capability and prolongs the lifespan of batteries. However, the active hybrid energy storage system needs complicated power electronics and control strategy to control the power flow. Directly connecting battery cells and ultracapacitor cells in parallel either improves the performance of

energy storage system in an electrified vehicle or does not need additional power electronics. As an important motivation of HESS, the power density of the direct coupled hybrid modules with a different number of the energy storage elements and connection topologies are compared. Experimental results of a battery cell and a hybrid module validate that the improvement of a hybrid module in respect of the operating range, voltage profile, and lifespan.

Chapter 6 proposes a pack design methodology to meet USABC PHEV-40, full HEV, and 48V mild HEV performance targets using battery and ultracapacitor energy storage elements in direct coupled topologies. Simulated responses of temperature dependent power capability and cold cranking requirements are embedded in the hybrid pack analysis and design process. A case study based on an 18650 NMC lithium-ion battery cell and a non-aqueous symmetric ultracapacitor is presented to investigate replacement tradeoffs between the two energy storage components. Among the performance metrics in the case study, ultracapacitors give the greatest improvement for short term two-second power. Moreover, for a PHEV-40 vehicle, the hybrid modules with aged battery cells still maintain a long all-electric range (37.5km), while an aged battery pack just can propel the vehicle for 13.4km under UDDS driving cycle.

Conclusions are made in Chapter 7.

Chapter 2

Energy Storage Systems in Electrified Vehicles

2.1 Introduction

In this chapter, features and performance of the lead-acid battery, nickel-metal hydride battery, lithium-ion battery, ultracapacitor, and lithium-ion capacitor are introduced in terms of power density, energy density, cycle life, self-discharge rate, cost, and efficiency. Owing to the high energy density and low self-discharge rate, the global market share of lithium-ion battery has a fast growing. The lithium-ion battery becomes the battery of choice for the traction battery in the electric powertrain. A challenge is that the poor power density of the lithium-ion battery always causes an oversized energy storage system, even though the power density of it is much higher than the lead-acid and nickel-metal hydride batteries. The ultracapacitor and lithium-ion capacitor own excellent power density, but they cannot be a candidate for energy storage system alone in an electric powertrain due to their poor energy density.

The requirements of an energy storage system about power and energy capabilities in different powertrains are introduced based on the goals from U.S. Advanced Battery Consortium LLC (USABC). For PHEV and EV, an energy storage system should have high power and energy capabilities. An energy storage system in HEV does not need high energy capability but high power capability. Moreover, state of the art of hybrid energy storage systems is reviewed in this chapter. In addition, the performance of the single energy storage components and hybrid energy storage systems are compared with the requirements of energy storage systems for HEV, PHEV, and EV.

2.2 Energy storage devices for electrified vehicles

2.2.1 Lead-acid battery

The lead-acid battery is a mature technology. There are different types of lead-acid batteries available. The standard flooded lead-acid battery has applied to the automobile starting, lighting and ignition (SLI) battery for many years. In the past 50 years, a sealed valve regulated lead-acid battery (VRLA) was developed by minimizing the amount of electrolyte and making more negative electrode active material than positive electrode active material. The VRLA battery does not need to release liquids or gasses, therefore, the battery no longer needs maintenance (ALABC, 2013).

A schematic diagram of a lead-acid battery is shown in Fig. 2.1. In a fully charged battery, the positive electrode is the lead oxide (PbO_2) and the negative electrode is lead (Pb). In the electrolyte, sulfuric acid (H_2SO_4) dilutes with water(H_2O). During discharge, PbO_2 reacts with HSO_4^- ion, three H^+ ions, and two electrons to generate

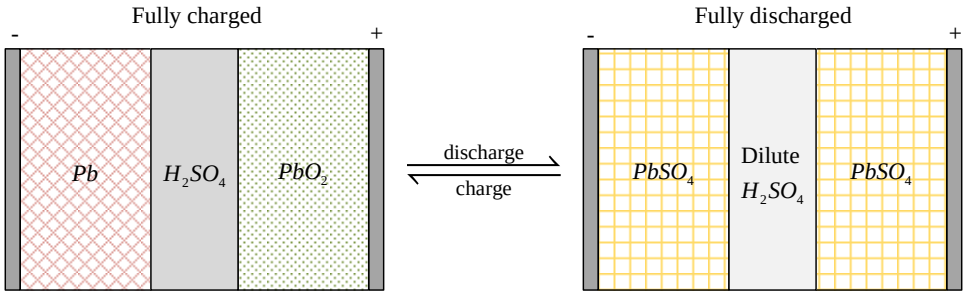

Figure 2.1: Schematic diagram of a lead-acid battery

$PbSO_4$ and two H_2O molecules at the positive electrode. At the negative electrode, Pb reacts with one HSO_4^- ion to form $PbSO_4$, one H^+ ion, and 2 electrons. Therefore, in a full discharge battery, the positive electrode, and the negative electrode are $PbSO_4$. The charging reaction returns $PbSO_4$ to Pb and PbO_2. The reactions can be written as (Emadi, 2014):

Positive electrode:

$$PbO_2 + SO_4^{2-} + 4H^+ + 2e^- \underset{\text{Charge}}{\overset{\text{Discharge}}{\rightleftharpoons}} PbSO_4 + 2H_2O \tag{2.1}$$

Negative electrode:

$$Pb + SO_4^{2-} \underset{\text{Charge}}{\overset{\text{Discharge}}{\rightleftharpoons}} PbSO_4 + 2e^- \tag{2.2}$$

The total reaction:

$$Pb + PbO_2 + 2H_2SO_4 \underset{\text{Charge}}{\overset{\text{Discharge}}{\rightleftharpoons}} 2PbSO_4 + 2H_2O \tag{2.3}$$

Even though the specific energy and specific power of lead-acid batteries are low,

they maintain $40\% - 45\%$ of the battery market (Rahn and Wang, 2013) due to they are widely used for starting, lighting, and ignition functions in conventional ICE vehicles and even electrified vehicles, like Toyota Prius hybrid and Ford Fusion hybrid (ALABC, 2013). Moreover, their round-trip efficiencies are around $70 - 80\%$, they are good candidates for traction batteries in HEV (Khaligh and Li, 2010; Rahn and Wang, 2013).

2.2.2 Nickel-metal hydride battery

Fig. 2.2 shows the schematic diagram of a NiMH battery. The mainly active material

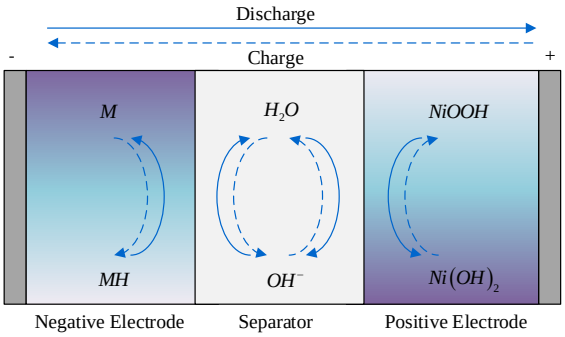

Figure 2.2: Schematic diagram of a NiMH battery

in the positive electrode is nickel oxyhydroxide ($NiOOH$) and the active material in the negative electrode is hydrogen-absorbing nickel alloy. The separator contains an alkaline electrolyte, like a solution of potassium hydroxide (KOH). During discharge, metal hydride (MH) is oxidized to the metal alloy (M), one H_2O molecule, and one electron in the negative electrode. In the positive electrode, $NiOOH$ is reduced to nickel hydroxide ($Ni(OH)_2$)with one OH^- ion. The reactions that drive the cell are (Emadi, 2014)

Positive electrode:

$$NiOOH + H_2O + e^- \underset{\text{Charge}}{\overset{\text{Discharge}}{\rightleftharpoons}} Ni(OH)_2 + OH^- \tag{2.4}$$

Negative electrode:

$$MH + OH^- \underset{\text{Charge}}{\overset{\text{Discharge}}{\rightleftharpoons}} M + H_2O + e^- \tag{2.5}$$

The total reaction:

$$MH + NiOOH \underset{\text{Charge}}{\overset{\text{Discharge}}{\rightleftharpoons}} M + Ni(OH)_2 \tag{2.6}$$

Nickel-metal hydride batteries have higher specific energy, specific power, and longer cycle life than lead-acid batteries. They have been used in hybrid electric vehicles as traction batteries, like Toyota Prius C hybrid. However, the main drawback is that nickel-metal hydride batteries have a relatively high self-discharge rate. The self-discharge rate is $5 - 20\%$ in the first 24 hours and stabilizes around 10% per month at room temperature. Moreover, they will self-discharge faster at high temperature (Buchmann, 2011).

2.2.3 Lithium-ion battery

Lithium-ion batteries have been successfully used in laptop, mobile phone, and other portable electronics. In recent years, they are becoming attractive for electrified vehicles. There are many types of lithium-ion batteries consisting of different active materials with different features (Emadi, 2014). Lithium cobalt oxide ($LiCoO_2$) is

widely used on the laptop due to the high specific energy. However, it has a short lifespan, low thermal stability, and low specific power. Lithium manganese oxide ($LiMn_2O_4$) is popular for cell phones. Although it has high power, but the specific energy, cycle life and calendar life are limited. Lithium iron phosphate ($LiFeP_4$) has a relatively high power capability and outstanding abuse tolerance, but the drawbacks of it are low capacity, low voltage, and short calendar life. Lithium nickel manganese cobalt oxide ($LiNi_xMn_yCo_zO_2$) and lithium nickel cobalt aluminum oxide ($LiNi_xCo_yAl_zO_2$) are new types of lithium-ion batteries which have the excellent specific energy and reasonable specific power. Different combination of three metals can provide different features. Their families are growing into strong competitors for electric powertrains. In the negative electrode, lithiated carbon (Li_xC) is a common active material. It has a high specific energy and low cost, but the unstable SEI layer causes a fast growth resistance and short cycle life. Another negative electrode material is lithium titanate ($Li_4Ti_5O_{12}$). Even though this material can provide a longer cycle life and calendar life than graphite, a relatively low specific energy and high potential become big challenges for electric vehicles and plug-in electric vehicles.

To explain the electrochemical reactions in lithium-ion batteries, $LiCoO_2$ could be an example. Fig. 2.3 shows a schematic diagram of a lithium-ion battery. In the negative electrode during discharge, Li_xC is oxidized and lithium ions are deintercalated and migrate to the positive electrode through the separator. Moreover, electrons flow to the positive electrode through an external circuit. In the positive electrode, lithium ions are intercalated and generate $LiCoO2$. These reversible reactions that govern this cell are

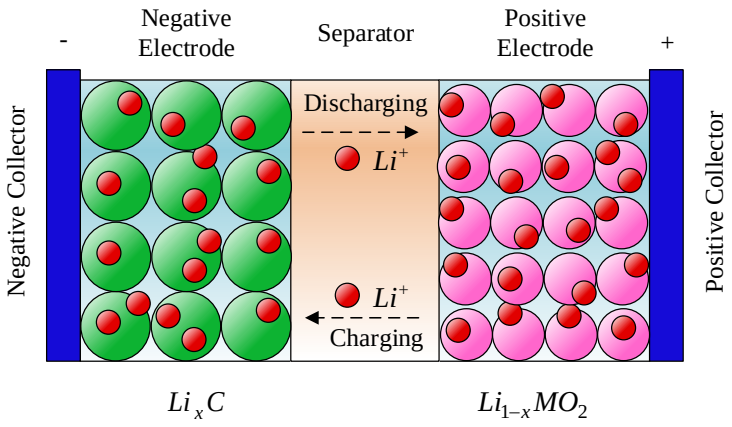

Figure 2.3: Schematic diagram of a lithium-ion battery

Positive electrode:

$$Li_{1-x}CoO_2 + xLi^+ + xe^- \underset{\text{Charge}}{\overset{\text{Discharge}}{\rightleftharpoons}} LiCoO_2 \tag{2.7}$$

Negative electrode:

$$Li_xC \underset{\text{Charge}}{\overset{\text{Discharge}}{\rightleftharpoons}} C + xLi^+ + xe^- \tag{2.8}$$

The total reaction:

$$Li_{1-x}CoO_2 + Li_xC \underset{\text{Charge}}{\overset{\text{Discharge}}{\rightleftharpoons}} LiCoO_2 + C \tag{2.9}$$

Overall, lithium-ion batteries' specific energy, terminal voltage, and round-trip efficiencies are typically higher than those of lead-acid and NiMH batteries. Due to the high energy density, lithium-ion batteries are becoming the battery of choice for plug-in hybrid electric vehicles and electric vehicles. The 85kWh battery pack of

Tesla Model S consists of more than 7,000 Panasonic 18650 lithium ion battery with NCA cathodes (Rawlinson, 2012, 2014; Straubel *et al.*, 2007).

2.2.4 Ultracapacitor

Ultracapacitor is a type of electrochemical capacitor with a high energy density which stores charges in the electrical field within two conductors. Therefore, it is also known as electrochemical double layer capacitor (EDLC). The structure of an ultracapacitor is shown in Fig. 2.4. A porous and spongy material with a large surface area, such as

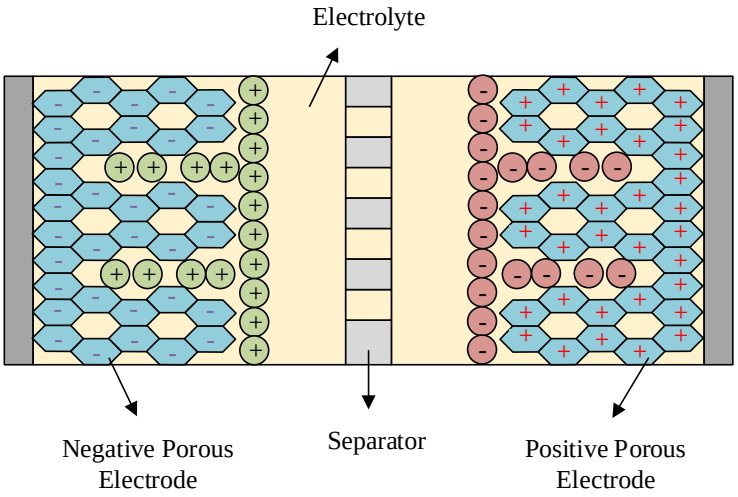

Figure 2.4: Structure of ultracapacitor

activated carbon, forms two electrodes of an ultracapacitor. The charge separation in the interface between the electrode and electrolyte is extremely small. Therefore, the ultracapacitor has a larger energy density than conventional capacitors. The energy stored in an ultracapacitor is related to the voltage and can be calculated by this

equation:

$$E = \frac{1}{2}C(V^2 - V_{min}^2) \tag{2.10}$$

C is the capacitance of a cell, V is the voltage of the cell, and V_{min} is the minimum voltage of the cell. Usually, an ultracapacitor's lower voltage limit is $\frac{1}{2}V_{max}$. Therefore, the useable energy in a cell is

$$E = \frac{1}{2}C(\frac{3}{4}V_{max}^2) \tag{2.11}$$

The energy utilization of an ultracapacitor is 75%. The energy density of the Maxwell BCAP0350 cell is 5.9Wh/kg which is higher than conventional capacitors but still much lower than batteries (Maxwell, 2013).

The main advantage of ultracapacitor is the high power density. The maximum power density of product in Maxwell can achieve 14000 W/kg (Maxwell, 2013). The extremely high power density and relatively high energy density cause a lot of research focus on utilizing ultracapacitor in the regenerative braking system and the start-stop system. In 2010, the second-generation micro-hybrid (e-HDi) system of PSA Peugeot-Citroën used a 600F/5V Maxwell ultracapacitor module to provide power for the scant 400 milliseconds to restart the engine. Maxwell Technologies has announced that 2016 Cadillac will also use an ultracapacitor module in ATS and CST sedans and ATS coupes.

2.2.5 Lithium-ion capacitor

To increase the energy density of ultracapacitors and power density of lithium-ion batteries, an innovative energy storage technology, lithium-ion capacitor, has been

proposed to close the gap between the ultracapacitors and lithium-ion batteries in the last few years (Ronasmans and Lalande, 2015).

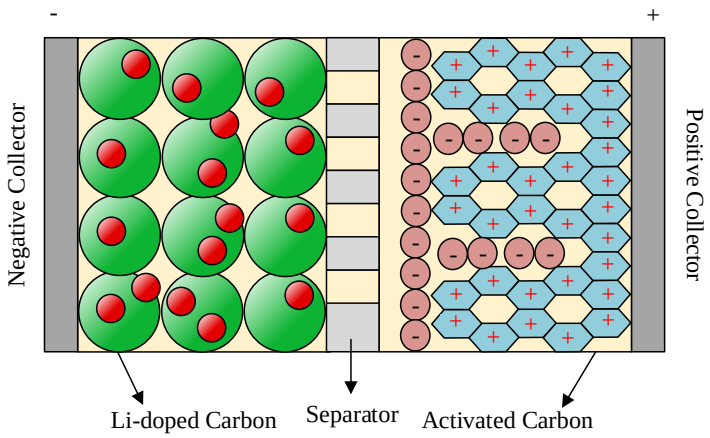

Figure 2.5: Structure of ultracapacitor

Fig. 2.5 shows the structure of a lithium-ion capacitor. In order to store more energy in the device, lithium ions are doped in the carbon in the negative electrode, which is similar to a lithium-ion battery, as known as Faradaic electrode. In the positive electrode, the activated carbon is used for a high power density and long lifespan, which is similar to an ultracapacitor, as known as the non-Faradaic electrode. Due to Faradaic electrode, the voltage range of a lithium-ion capacitor is from 2.2 to 3.8V. The energy density of lithium-ion capacitor can achieve 12Wh/kg which is twice as ultracapacitor. Lithium-ion capacitors from JSR Micro have been commercially used in hybrid buses in Europe.

2.2.6 Comparison table of energy storage devices

The characteristics of above energy storage devices are compared in Table 2.1. Compared to other battery devices, lithium-ion battery is outstanding for all characteristics in this table. However, ultracapacitor and lithium-ion capacitor are superior on the specific power and power density. Although both of lithium-ion battery and EDLC are popular candidates for electrified vehicles, an energy storage system consists of one of them alone may not provide abundant power or energy to propel the vehicle unless the energy storage system is oversized. In the next subsection, the requirements of energy storage systems in different electrified vehicles are discussed.

Table 2.1: Comparison table of energy storage devices (Bradbury, 2010; Emadi, 2014; Maxwell, 2013)

Specifications	Lead-acid	NiMH	Lithium-ion battery	UC	Lithium-ion capacitor
Specific energy (Wh/kg)	30-50	60-120	75-250	0.7-6	12
Energy density (Wh/L)	50-80	60-150	200-500	1.6-5.7	15-20
Specific power (W/kg)	75-300	150-300	150-315	2k-14k	16k
Power density (W/L)	10-400	80-300	100-210	4k-12k	23k
Round-trip efficiency (%)	70-80	60-70	85-98	90-98	95-99
Self-discharge (%/day)	0.033-0.3	0.067-0.6	0.1-0.3	20-40	0.1-12.5
Cycle lifetime (cycles)	100-2000	800-3500	400-1200	10k-500k	200k-300k
Power capacity cost ($/kW)	175-600	150-1500	175-4000	100-360	50-320
Energy capacity cost ($/kWh)	150-400	150-1500	500-2500	300-94k	600-50k

2.3 Energy storage system requirements in electrified vehicles

According to the degree of hybridization, the electrified vehicles could be divided into various hybrid electric vehicles, plug-in hybrid electric vehicles, and battery electric vehicles. A hybridization factor which defines the percentage of the electric propulsion system in a hybrid electrical and mechanical propulsion system could be from 5% for the micro hybrid to 100% for the electric vehicles (Lukic *et al.*, 2008). This section summarizes the power and energy requirements of the energy storage systems in different electrified vehicles.

2.3.1 Hybrid electric vehicles

Compared to the conventional powertrains, hybrid powertrains integrate electric power systems into vehicle platforms and assist the ICE to propel the vehicles. According to the configurations of connecting the electric power path with mechanical power path, hybrid powertrains can be classified as series, parallel, or series-parallel (Emadi, 2011).

- Series hybrid powertrain

  A hybrid electric vehicle with a series hybrid powertrain architecture is shown in Fig. 2.6 (a). In this configuration, only the motor/generator drives the wheels and the ICE is mechanically decoupled from the wheels. The ICE is used to generate electrical energy to drive the motor/generator and charge the energy storage system. During regenerative braking and deceleration, the motor/generator is also used to charge the energy storage system. This series powertrain could

be used in plug-in hybrid vehicles with a large battery pack so that the ICE just provides energy for long journeys.

- Parallel hybrid powertrain

  Fig. 2.6 (b) shows the architecture of a parallel hybrid powertrain. Unlike the series hybrid powertrain, the ICE is coupled with the motor/generator and connects to the transmission to drive the vehicle. The energy storage system could be charged by the motor/generator and the ICE through the mechanical coupling. However, a limitation of the parallel hybrid powertrains in the all-electric mode is that it is difficult to operate at high speed.

- Series-parallel hybrid powertrain

  The architecture of a series-parallel hybrid powertrain is shown in Fig. 2.6 (c). The ICE can drive the vehicle either through the mechanical coupling in the parallel path or through the generator in the series path.

According to the functions performed by the mechanical and electrical propulsion systems, the hybrid electric vehicles could be classified as micro hybrid powertrains, mild hybrid powertrains, and full hybrid powertrains. The requirements of the energy storage system are different with respect to the degree of hybridization. The capabilities of different powertrains are summarized in Table 2.2.

- Micro hybrid powertrains

  The micro hybrid powertrains have the lowest degree of hybridization and are not a technically hybrid powertrain since the vehicle is powered solely by the ICE. To reduce the ICE idling time, emissions, and fuel consumption, a stop-start system is involved in shutting down the ICE when the vehicle goes to stop

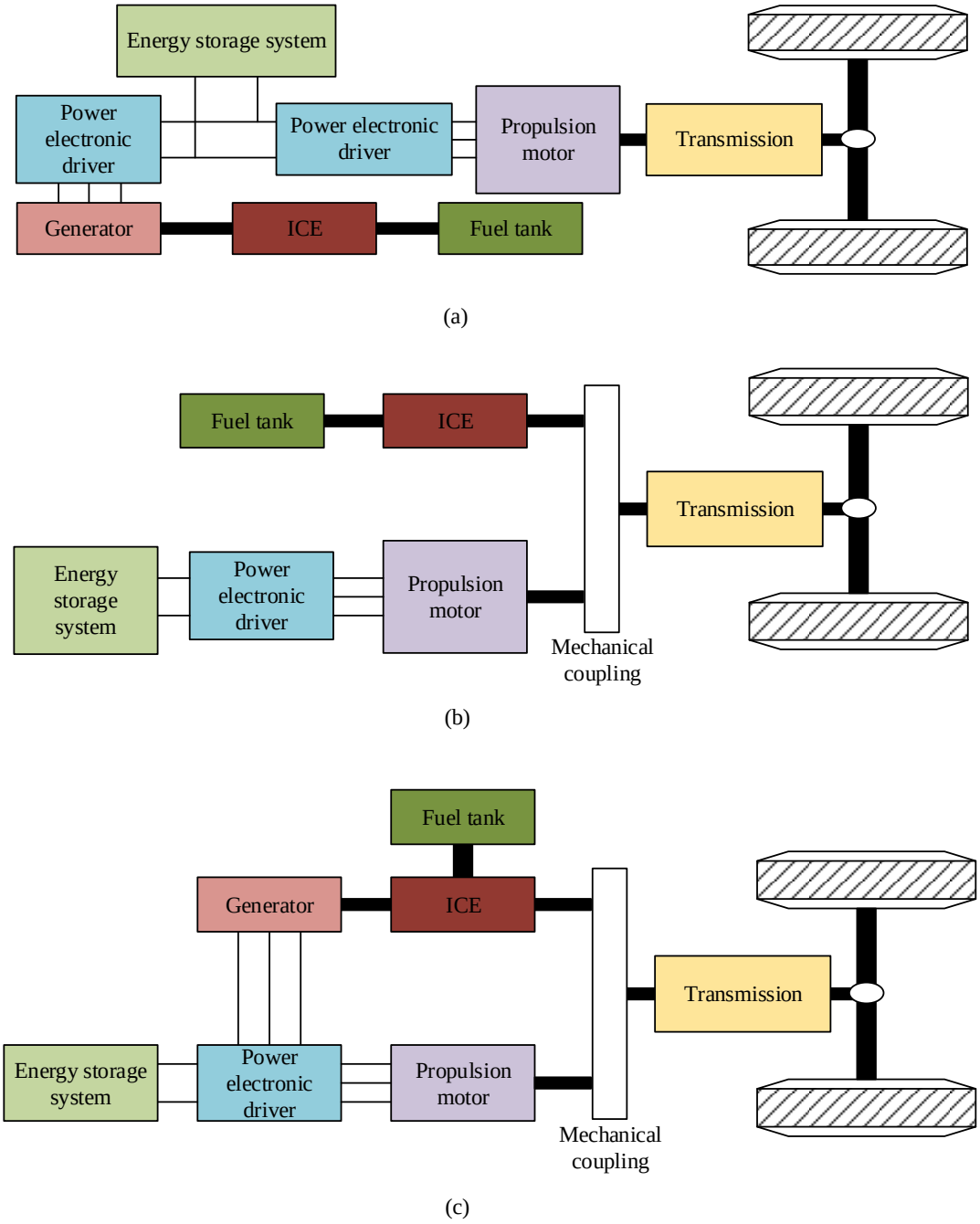

Figure 2.6: Examples of series, parallel, and series-parallel hybrid powertrain architectures

Table 2.2: Capabilities of different powertrain types (Hutchinson *et al.*, 2014)

Capability	Micro hybrid	Mild hybrid	Full hybrid	Plug-in hybrid
Stop-start	Yes	Yes	Yes	Yes
Regenerative braking	No	Yes	Yes	Yes
Power-assist	No	Yes	Yes	Yes
All-electric drive mode	No	No	Yes	Yes
External battery charging	No	No	No	Yes

for a jam or a red light and restarting the ICE immediately once the clutch is pressed. The micro hybrid powertrains do not need a large energy storage system. According to USABC (USABC, 2014b), a 360Wh energy storage system with 6kW discharge pulse power capability (1s) can satisfy the requirements of the 12V stop-start system.

- Mild hybrid powertrains

  Generally, in a mild hybrid powertrain, one ICE and one motor/generator are coupled to a mechanical coupling in a parallel hybrid architecture as shown in Fig. 2.6 (b). The mild hybrid powertrains can capture regenerative braking and provide electric power assist besides an engine stop-start system. Even though a mild hybrid powertrain is incapable of driving a vehicle in an all-electric driving mode, the energy storage system of it is still much higher than in the micro hybrid powertrains.

  Honda developed a mild hybrid technology with an integrated motor assist (IMA) system and applied to the Honda Civic. In the second generation (2006-2011), a 158.4V ($132 \times 1.2V$) 5.5Ah capacity NiMH battery pack was used to power a 15kW permanent magnet motor. According to the FreedomCAR

energy storage system performance goals for power-assist hybrid electric vehicle (USABC, 2002), an energy storage system in a mild hybrid powertrain should provide 25kW power for a 10-second discharge pulse and 0.3kWh energy at 1 C-rate.

From (German, 2015), 48V mild hybrid systems would be more attractive in future since less expensive components would be used. According to a report from USABC, the development of the 48V mild HEV will reduce a 50% cost. From USABC requirements of energy storage systems for 48V HEV (USABC, 2014c), the energy storage system should provide 11kW power for a 1-second discharge pulse and 105Wh for available energy.

- Full hybrid powertrains

  A full hybrid powertrain contains a capability of all-electric driving mode besides all the features of the mild hybrid powertrains. Therefore, this vehicle needs a large energy storage system with a high energy capability to propel the vehicle in a relatively long all-electric range. The full hybrid powertrain does not have the plug-in charge capability which means the energy storage system is charged by regenerative braking and the ICE.

  The second generation Prius model is an example of a series-parallel full hybrid powertrain. The traction battery pack consists of 38 NiMH modules in series to provide a 273.6V 6.5Ah energy storage system. The operating range of the 1.77kWh battery pack is from 40% to 60% SOC, therefore, the available energy of the system is around 350Wh. Discharge and regenerative power capability of the system are around 20kW and 14.5kW in the operating range. From the USABC manual (USABC, 2002), an energy storage system for a full hybrid can

release 40 kW for a 10-second discharge pulse and receive 35kW for a 10-second regenerative pulse. The available energy of the system should reach to 500Wh at 1 C-rate.

2.3.2 Plug-in hybrid electric vehicles

A plug-in hybrid electric vehicle is a hybrid electric vehicle has a large energy storage system for longer all-electric range than full hybrid electric vehicles and can be plugged into an electrical outlet to be charged. Series, parallel, and series-parallel hybrid powertrains can be used in the plug-in hybrid electric vehicles. Fig. 2.7 shows an example architecture of the plug-in parallel hybrid powertrains.

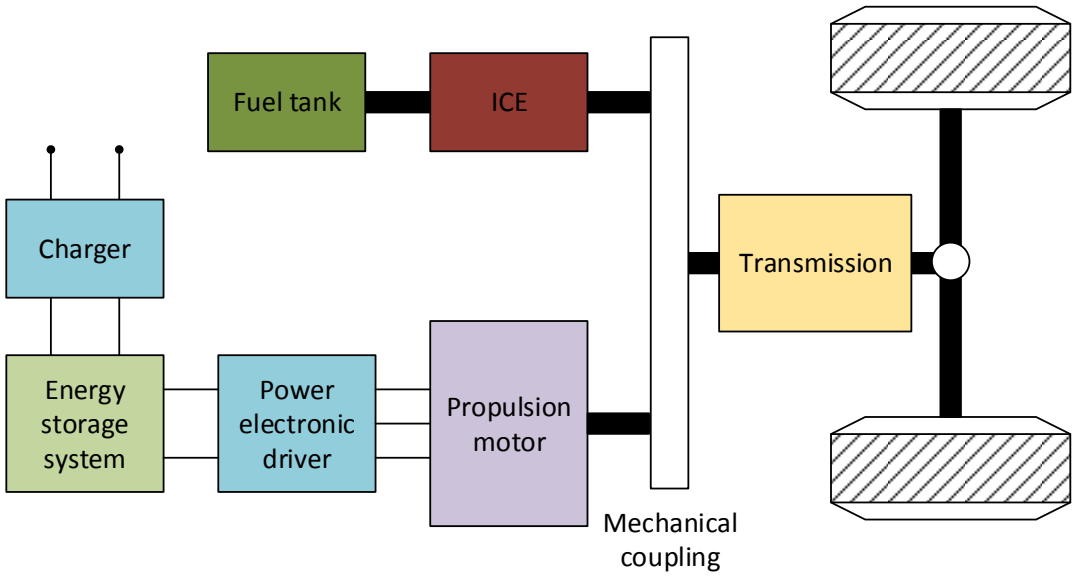

Figure 2.7: A Parallel plug-in hybrid powertrain architecture

Two operation modes in the plug-in hybrid electric vehicles are charge-depletion

(CD) mode and charge-sustaining (CS) mode (USABC, 2014a). The operating philosophy is shown in Fig. 2.8. A fully charged plug-in hybrid electric vehicle drives in the all-electric mode, or CD mode, until a predefined amount of energy for CD mode is removed. When the vehicle achieves the $AE_{CD_{Target}}$ in this figure, the vehicle switches to the power assist mode or CS mode. In this mode, the energy storage system in the vehicle works in a narrow operating window between the green line $AE_{CS_{Limit}}$ and red line $AE_{Total_{Target}}$. Therefore, the energy storage system in a plug-in hybrid electric vehicle needs to satisfy targets of discharge power, regenerative braking power, available energy for CD mode, and available energy for CS mode. Generally, a plug-

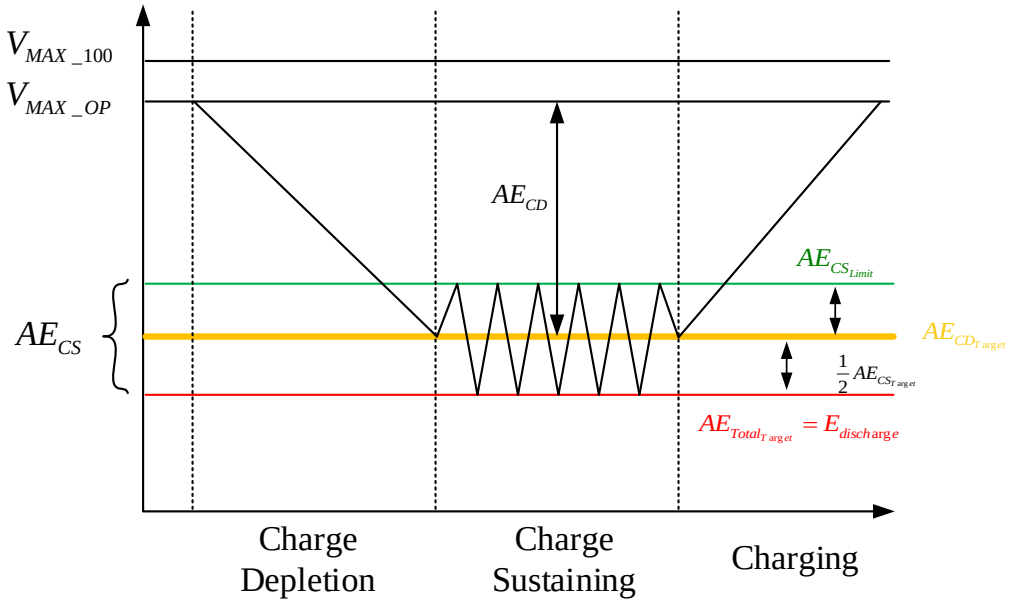

Figure 2.8: PHEV operating philosophy (USABC, 2014a)

in hybrid electric vehicle needs a larger energy storage system than full HEV for a longer all-electric mode. The Prius plug-in hybrid model shares all features of the

standard Prius full hybrid model, but increases the battery capacity to 4.5 kWh for 10-15 miles all-electric range and adds the plug-in charging capability (Hutchinson *et al.*, 2014). The Fisker Karma, a luxury sports car, uses a 20.1kWh battery bank to support 32 miles all-electric range in a series plug-in hybrid powertrain. In USABC goals (USABC, 2014d), an energy storage system for a PHEV-40 (40 miles all-electric range) should provide 38kW power for a 10-second discharge pulse and 25kW power for a 10-second regenerative pulse. The available energy for CD mode is 11.6kWh and the available energy for CS mode is 0.3kWh.

Another feature of the plug-in hybrid electric vehicles is that if a bidirectional ac-dc converter is used to charge a battery pack from the utility grid, the bidirectional converter can return power from the vehicle to grid and store energy in a smart grid.

2.3.3 Battery electric vehicles

A battery electric vehicle is a vehicle which is solely powered by electric energy. The architecture of a typical battery electric vehicle is shown in Fig. 2.9. A large capacity energy storage system is required to propel the vehicle for a reasonable long journey. The typical voltage range of the energy storage system is from 300V to 400V. The capacity of it should be higher than 20kWh. The electric vehicle Nissan Leaf has a 24kWh battery bank which was composed of 192 lithium-ion battery cells in series. The U.S. Environmental Protection Agency (EPA) official range for the Nissan Leaf 2016 model is 84 miles. The Tesla 2012 Model S had an 85kWh lithium-ion battery pack which consists of 16 battery models. Each model contains 6 groups in series and each group connects 74 cells in parallel. According to the EPA, the total 7,104 cells can support 265 miles electric range (Rawlinson, 2012, 2014; Straubel *et al.*, 2007).

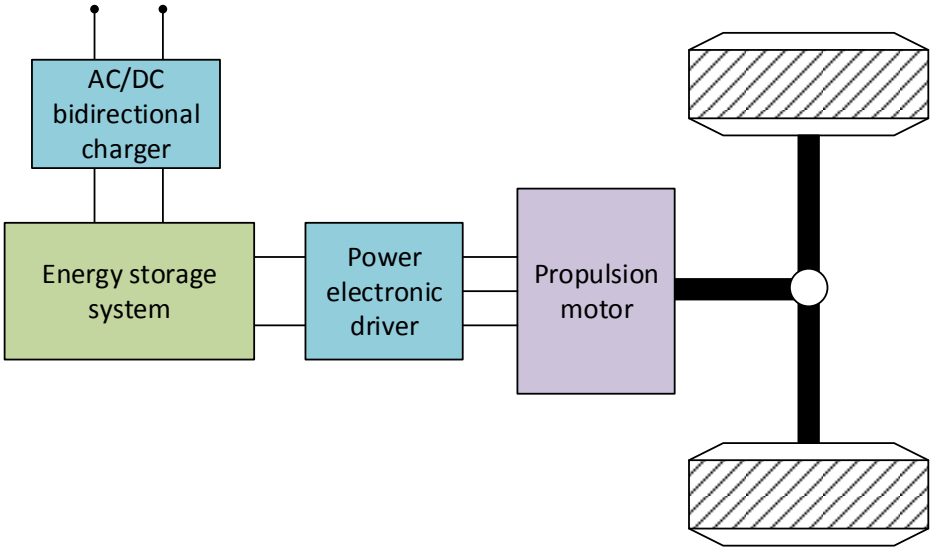

Figure 2.9: A battery electric vehicle powertrain architecture

2.3.4 Summary of energy storage system requirements in electrified vehicles

According to USABC, the energy storage system goals for different electric drive vehicles are summarized in Table 2.3.

2.4 Hybrid energy storage system

In electrified vehicles, the capability of the energy storage system (ESS) decides the efficiency and all-electric range of the system. The ESS needs the capability to not

Table 2.3: USABC Requirements of Energy Storage Systems (USABC, 2002, 2014a,b,c, 2015)

Characteristics	Micro HEV	Power-assist HEV (Min)	Mild HEV (48V)	Power-assist HEV (Max)	PHEV-40	EV (long-term)
Peak Pulse Discharge Power (kW)	6 (1s)	25 (10s)	9 (10s)	40 (10s)	38 (10s)/ 46 (2s)	90 (30s)
Peak Pulse Regen Power (kW)	-	20 (10s)	11 (5s)	35 (10s)	25 (10s)	40 (10s)
Available Energy (kWh)	0.36	0.3	0.105	0.5	11.6 (CD), 0.3 (CS)	45
Max operating voltage (V)	15	$\leqslant 400$	52	$\leqslant 400$	$\leqslant 400$	420
Min operating voltage (V)	10.5	$\geqslant 0.55V_{max}$	38	$\geqslant 0.55V_{max}$	$\geqslant 0.55V_{max}$	220
Max system weight (kg)	10	40	8	60	120	200
Max system volume (L)	7	32	8	45	80	90
Temperature (^oC)	-30$\sim$52	-30$\sim$52	-30$\sim$52	-30$\sim$52	-30$\sim$52	-30$\sim$52
Life (cycle)	450k	300k	75k	300k	5000 (CD)	1000

only store a large amount of energy for long distance driving but also quickly release energy in different demand. To design an ESS for a vehicle, energy density, power density, lifetime, cost and maintenance need be considered as the important characteristics. A single energy storage system is difficult to meet all requirements of electrified vehicles presently, hence, the hybrid energy storage system is widely researched.

Hybrid energy storage system (HESS) combines two or multiple energy storage

systems together to get beneficial parts of these energy storage systems and compensates drawbacks of them by each other. Usually, a hybrid energy storage system consists of two energy storage systems that one provides high energy density and another one provides high power density. Currently, the common options for HESS are battery and ultracapacitor. The battery can store enormous energy as the high energy density storage system. Ultracapacitor has high power density and presents the feature of a long lifespan.

The operation states could be divided by high power demand, low power demand, and negative power (Ehsani *et al.*, 2009). The high power demand happens when the vehicle is accelerating or climbing a hill. Both of the two energy storage systems need release energy to the motor. During the lower power demand as the vehicle is running at constant speed, the primary power flow is from the high specific energy system. At the same time, the high specific energy system charges to the high specific power system to restore its power lost during high power demand and prepare for the next high power demand. During a regenerating breaking, the hybrid energy storage system is working on the negative power state. The high specific power system absorbs the high peak power, and the remaining energy is stored into the high specific energy system. As a high specific power energy storage system, the ultracapacitor can release high energy in a short time and protect batteries by storing high peak current in the negative power demand. Three basic operation states are shown in Fig. 2.10.

The purpose of HESS can be summarized as a fast response for the high power demand and low response for the high energy demand. To implement those purposes in different operations, there are several topologies were proposed to manage the power flow.

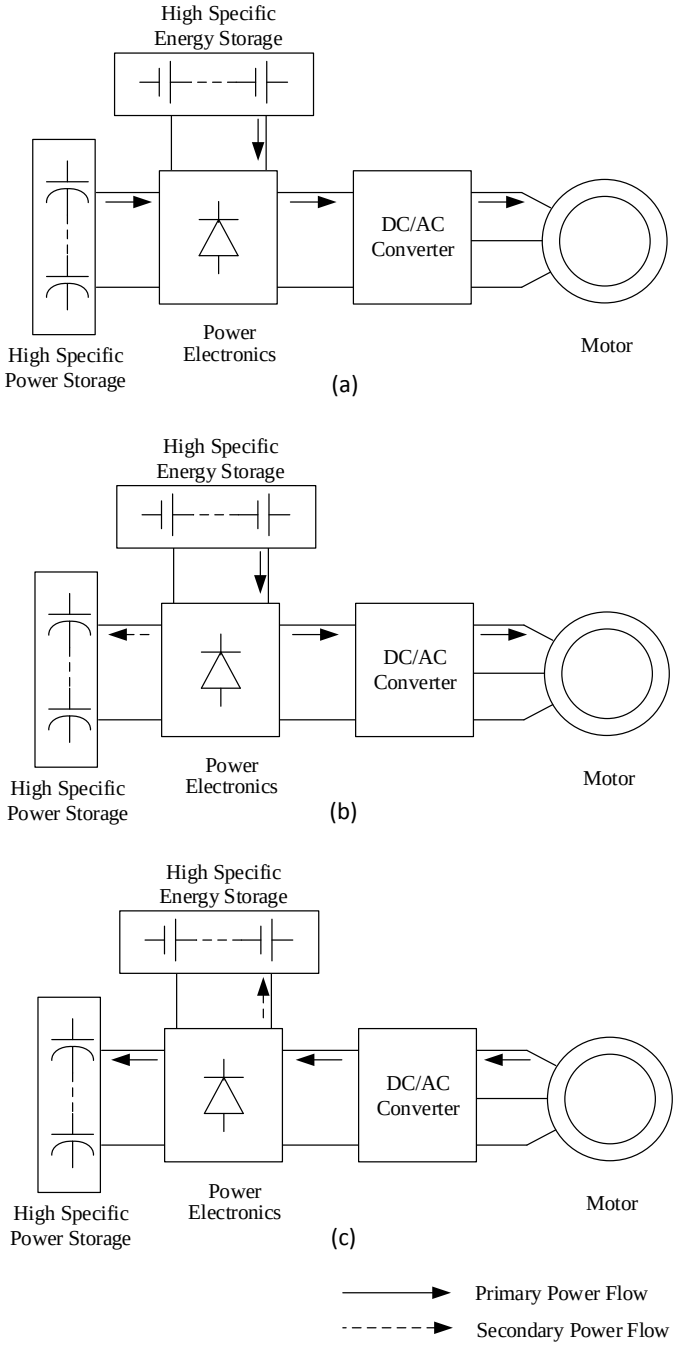

Figure 2.10: Concept of a typical paralleled hybrid energy storage system operation states. (a) high power demand, (b) low power demand, (c) negative power

2.4.1 Passive hybrid energy storage system

Fig. 2.11 shows a passive cascaded HESS. The ultracapacitor pack is directly connected with the battery pack in parallel. To control the power flow in or out the hybrid energy storage system, a bidirectional DC/DC converter connects the HESS and DC link. This topology is easy to control and implement. The energy in the ultracapacitor pack may not be sufficiently used since the voltage of the ultracapacitor pack must be the same with the voltage on the battery pack. Moreover, both of the two systems need individual cell balancing circuits.

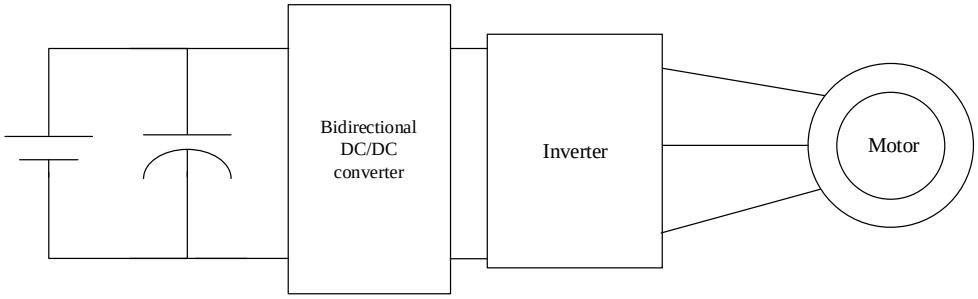

Figure 2.11: Passive HESS configuration

2.4.2 Active ultracapacitor/ battery hybrid energy storage system

To improve the controllability of the hybrid energy storage system, many active topologies have been researched. One of the widely used topologies is the ultracapacitor/ battery HESS configuration as shown in Fig. 2.12 (a). The ultracapacitor pack connects to the battery pack through a bidirectional DC/DC converter. The battery pack directly connects the DC link. The voltage of the ultracapacitor pack could be low. However, to handle the high power of the ultracapacitor pack, the size

of the bidirectional DC/DC converter should be large. The battery pack provides a relatively constant voltage to the inverter, thus the DC link cannot be varied and the operating range of the motor is limited.

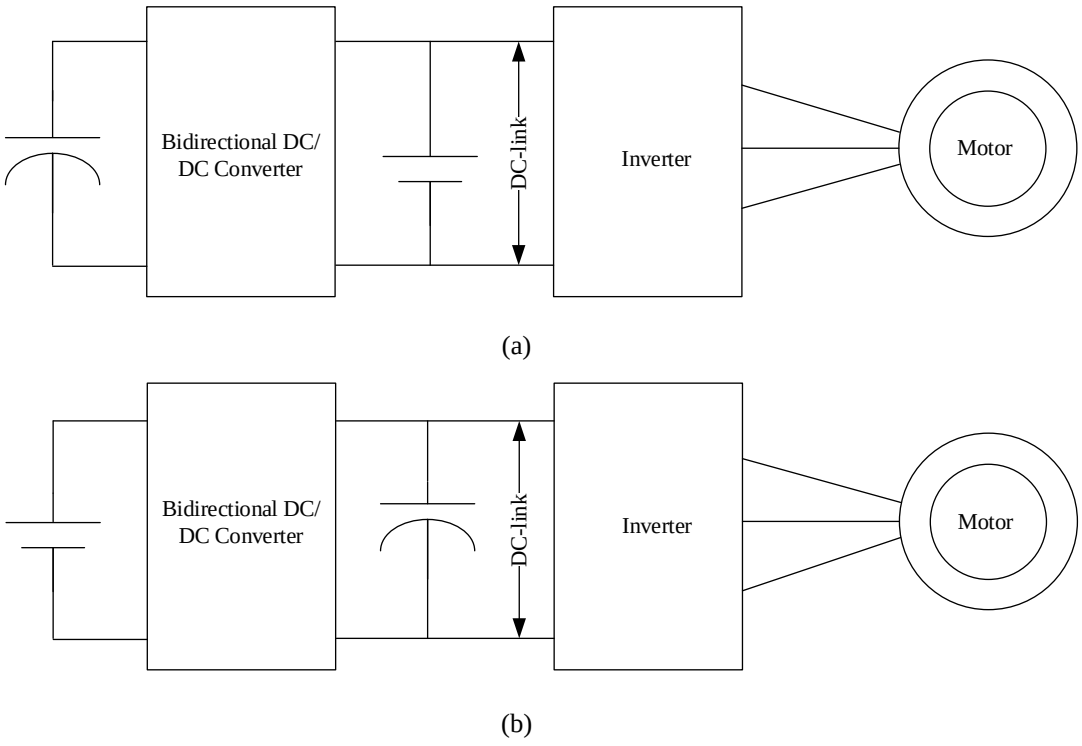

Figure 2.12: Active ultracapacitor-battery and active battery-ultracapacitor configurations, (a) active ultracapacitor/battery configuration, (b) active battery/ultracapacitor configuration

2.4.3 Active battery/ ultracapacitor hybrid energy storage system

In another configuration, the position of the battery pack and ultracapacitor is switched as shown in Fig. 2.12 (b). The functional of ultracapacitor in the topology is like a low-pass filter because it directly connects to the DC link. If the DC link voltage is varied during some operation demands, this voltage can be controlled by the bidirectional DC/DC converter. Moreover, the ultracapacitor can directly provide high power to the DC link in a high power density demand.

2.4.4 Active cascade hybrid energy storage system

To obtain a stronger power flow controllability, another two cascaded configurations were proposed from the ultracapacitor/battery topology and battery/ultracapacitor topology. The improvement of them is by adding a bidirectional DC/DC converter to interface hybrid energy storage system and the DC link as shown in Fig. 2.13 (a) and Fig. 2.13 (b). These cascaded topologies can separately control the battery pack and ultracapacitor pack with more complicated control strategies and topologies.

2.4.5 Parallel active hybrid energy storage system

In order to get higher efficiency and stability, a topology which the battery pack and ultracapacitor are independently connected to the DC link through two bidirectional DC/DC converters in a parallel structure were proposed as shown in Fig. 2.14. This topology allows that the battery pack and ultracapacitor pack have a lower voltage

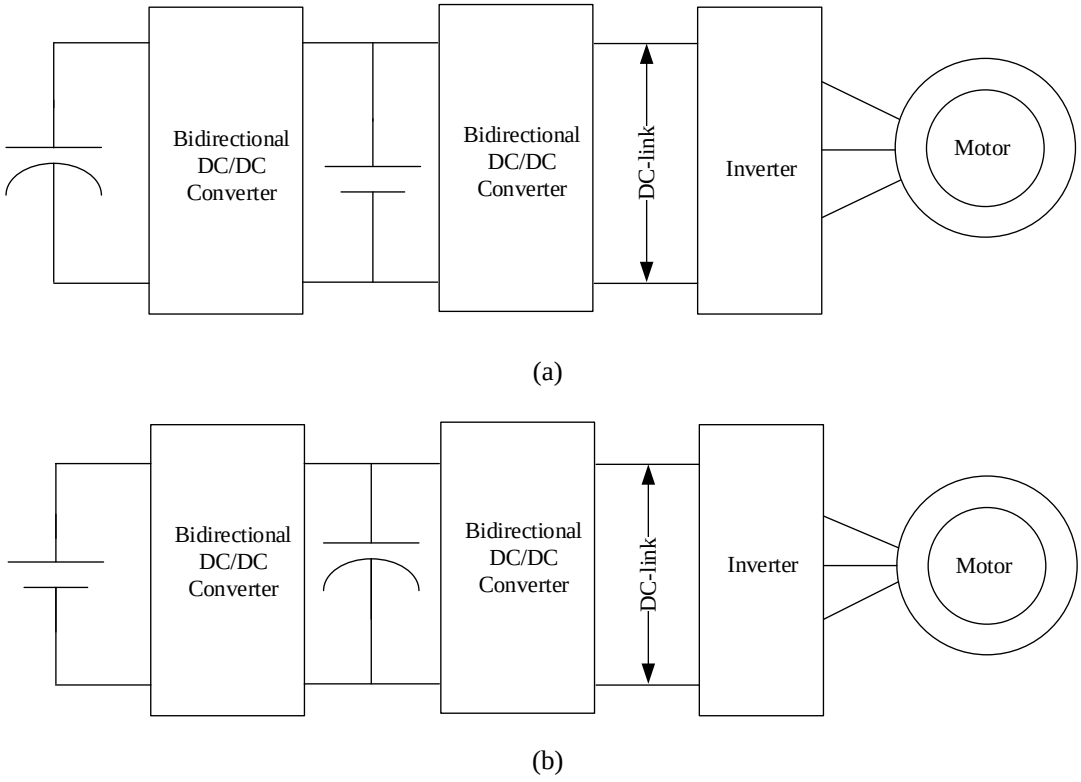

Figure 2.13: Active cascade HESS configurations, (a) active cascade ultracapacitor/ battery HESS configuration, (b) active cascade battery/ultracapacitor HESS configuration

level than the DC link. The voltage on the DC link could be stepped up by the bidirectional converters. The energy in the ultracapacitor pack can be fully utilized. Even though this topology enables a more flexible control, the size, cost, and complexity of control strategy are challenges.

2.4.6 Multi-input hybrid energy storage system

An extension of the multiple converters topology is the multiple inputs converter topologies as shown in Fig. 2.15. It integrates two full-size bidirectional DC/DC

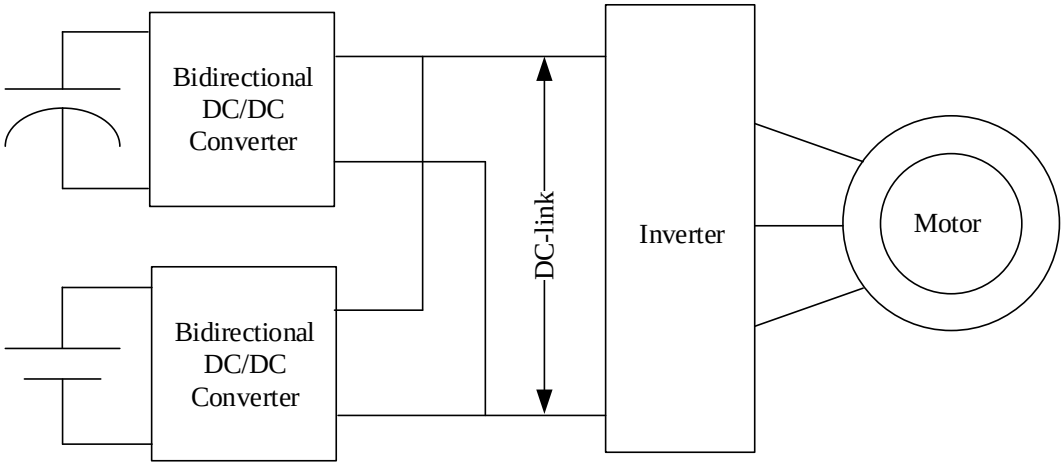

Figure 2.14: Parallel active HESS configuration

converters into a single bidirectional converter with two inputs. This topology reduces the cost, size, and weight, even if there are more inputs in this system. However, the control strategy is more complicated.

Overall, the power density of HESS topologies are higher than battery technologies, but the topologies and control strategies would be complicated. Moreover, due to the poor capacity of heavy ultracapacitors and large size power electronics, the energy density of HESS is much lower than lithium-ion battery technologies. From (Khaligh and Li, 2010), the power density and energy density of HESS topologies are around $700W/kg$ and $35Wh/kg$. The poor energy density and complicated topologies lead to the hybrid energy storage systems have not been widely involved in commercial electric vehicles and hybrid vehicles recently.

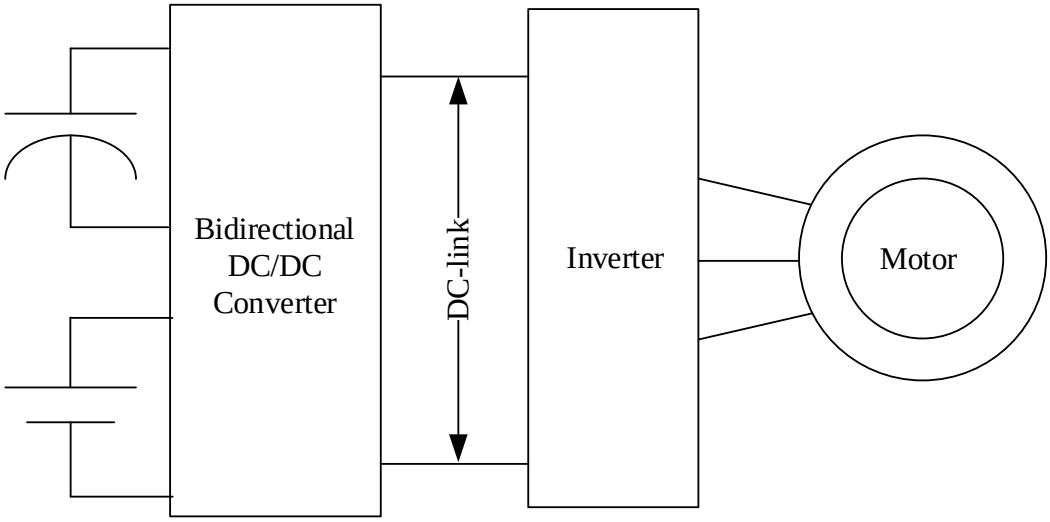

Figure 2.15: Multi-input HESS configuration

2.5 Conclusions

In order to summarize the performance of currently energy storage technologies and hybrid energy storage systems in terms of power and energy capability, specific power and specific energy of them are drawn in Fig. 2.16 and compared with the USABC ESS goals for the different types of electrified vehicles. The lithium-ion battery technologies satisfy the energy requirements of the electric and hybrid vehicles but need a higher specific power. Ultracapacitor and lithium-ion capacitor have excellent specific power, but the poor specific energy limits them to be a single energy storage system in an electrified vehicle. Typical hybrid energy storage systems combine high specific power ultracapacitor and high specific energy lithium-ion battery, but they still cannot meet the energy requirements of the EV and PHEV and the power requirement of the 48V mild HEV.

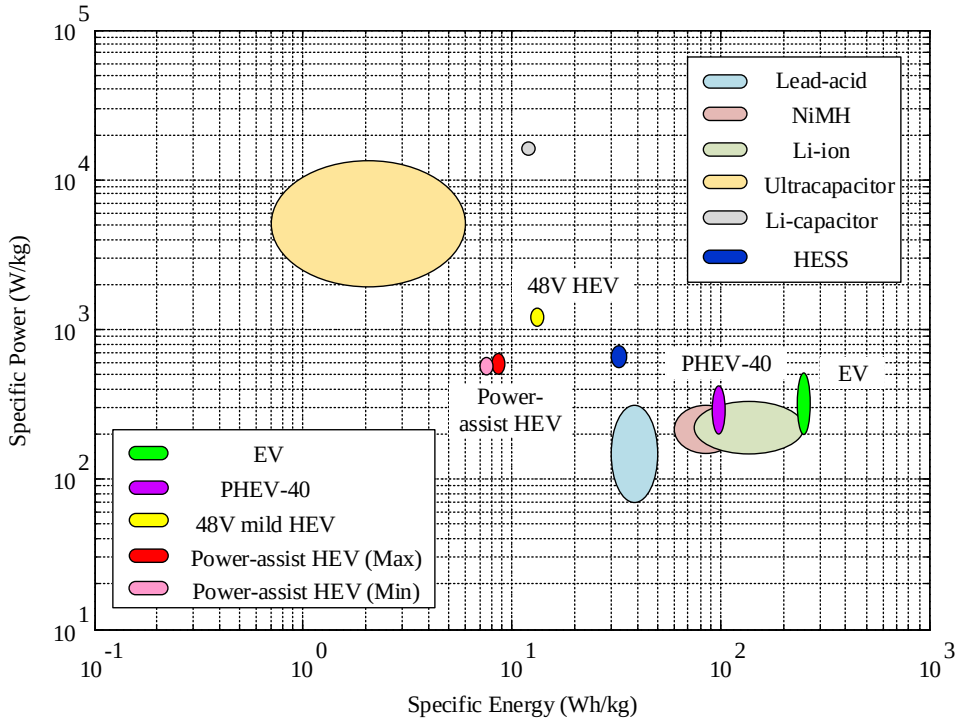

Figure 2.16: Ragone plot specific energy vs specific power

Chapter 3

Linear Programming based Battery Pack Balancing Topology Analysis

3.1 Introduction

As an energy source in electrified vehicles, the battery pack provides energy and power to the vehicle. The operational voltage of the battery pack usually requires many cells to be connected in series to optimize power, efficiency and cost of the electrified powertrain. Cell to cell differences in state of charge, capacity, and impedance are common sources of imbalance in the battery pack. Cell imbalance can lead to incomplete use of pack energy and can accelerate cell aging/degradation.

There are many balancing methods developed to handle this problem. They can be classified into passive balancing and active balancing. Passive balancing is simple, but has high energy loss. A typical passive balancing method uses dissipative shunting resistors (Cao and Emadi, 2012; Daowd *et al.*, 2011). Many active balancing topologies have been proposed (Baronti *et al.*, 2014; Bonfiglio and Roessler, 2009; Cao *et al.*,

2008; Corporation, 2013; Daowd *et al.*, 2011; Einhorn *et al.*, 2011; Nishijima *et al.*, 2000; Preindl *et al.*, 2013; Yun *et al.*, 2013), these aim for higher energy efficiency though transfer of energy between cells. However, active balancing methods typically have higher complexity and cost compared to passive balancing. Recently, Daowd et al. have proposed a pack-level balancing system using different active balancing methods at the cell and module connection levels (Daowd *et al.*, 2014).

The balancing topology should operate in an optimal manner. This is dictated by the balancing control objective. Balancing control objectives can be classified into voltage based, state of charge (SOC) based, and capacity based (Barsukov and Qian, 2013). Einhor et al. (Einhorn *et al.*, 2011) demonstrated through simulation and experimental testing that SOC and capacity based methods are more effective than a voltage based approach. The SOC and capacity based balancing approaches require high-accuracy SOC and capacity estimation algorithms to operate optimally.

The balancing control strategy and its algorithm also affect performance of active balancing. Caspar and Hohmann proposed an on-line optimization based strategy that considered a non-linear cell model and inductive balancing circuits. The goal of their approach was to reduce energy loss during the balancing process, a dynamic optimization algorithm was applied to find the optimal switching sequence and duty cycle. Fuzzy logic based control algorithms have also been proposed to adaptively control equalization currents (Lee and Cheng, 2005; Yan *et al.*, 2010). Recently, Najmabadi evaluated cell-to-cell and cell-to-pack based control approaches on an active balancing prototype (Najmabadi, 2013).

Analysis research on performance and optimal design of active balancing circuits have also been recently performed. Narayanaswamy et al. (Narayanaswamy *et al.*,

2014) used multi-objective optimization for minimizing energy dissipation losses and installation volume. Switching and conduction losses of different electronic components was considered in the design optimization. Baronti et al. (Baronti *et al.*, 2014) developed generalized models of four active balancing topologies to calculate the minimum energy loss and the balancing time. Performance of a balancing topology was analyzed numerically using probability density function distributions with many initial cell state test cases. Preindl et al. (Preindl *et al.*, 2013) proposed a linear programming based method to compute the worst case balancing time and energy loss among different balancing topologies. Symmetries and convexity properties of the topologies were exploited to make computation tractable when determining worse cast performance given ranges of initial cell SOC states.

A battery pack is typically divided into modules and balancing is needed at both module and cell level, i.e. cells are balanced within a module, and modules can be balanced at the pack level. Both battery pack configuration (number of cells in series inside a module, and number of modules in series in a battery pack) and the balancing circuit design influence the performances of the battery pack. Balancing time, plug-in charge time, and energy loss of five kinds of balancing topologies and 25 two-level combinations of these five balancing topologies are evaluated in this paper. The linear programming approach presented in (Preindl *et al.*, 2013) is extended to consider a modular battery pack design and mixed combinations of passive/active balancing. Components counts of the two-level combinations are also presented. The performance is benchmarked against conventional passive balancing.

The rest of the chapter is organized as follows. The linear programming based

analysis method is shown in Section 3.2. Section 3.3 presents the four core active balancing topologies that are used at both the module and pack levels. In Section 3.4, pack-level analysis is presented. Conclusions and future work is highlighted in Section 3.5.

3.2 Balancing Topology Analysis Method Based on Linear Programming

In this section, the linear programming based analysis method is presented. A more theoretic treatment of this approach is provided in (Preindl *et al.*, 2013). Equality constraints, inequality constraints, and the objective functions are presented. The balancing algorithm is based on balancing SOC, the stored charge in a cell at time τ can be expressed via Coulomb counting as

$$SOC(\tau) = SOC(0) + \frac{1}{Q}\int_0^{\tau} i(t)dt \tag{3.1}$$

where $SOC(0)$ is the initial SOC, Q is the total capacity, and i is current through the cell. In a battery pack system, the current includes charging/discharging current of the pack and the balancing current into/from individual cells.

Many balancing circuits work with high frequency switching power electronics. In this chapter, the analysis work ignores dynamic cell process and focuses on charge movement to find the optimal average balancing command. The distributed charge in cell i during time τ is linearized to $i_{bi}\tau$ with unit Ah, where i_{bi} is the average balancing current of the i^{th} cell. The SOC of the cells and the balancing topology is

represented in the form

$$\begin{bmatrix} SOC_1(\tau) \\ \vdots \\ SOC_n(\tau) \end{bmatrix} = \begin{bmatrix} SOC_1(0) \\ \vdots \\ SOC_n(0) \end{bmatrix} + \frac{1}{Q}\mathbf{T} \begin{bmatrix} i_{b1}\tau \\ \vdots \\ i_{bn}\tau \end{bmatrix} \tag{3.2}$$

where the $\mathbf{T}$ matrix contains interconnection information of the pack balancing circuit topology, its capabilities, and the arrangement structure of the battery modules within the pack.

An equality constraint is needed to represent a balanced system state at the terminal time τ. When all cells in a string are balanced, the SOC of all the cells satisfy

$$SOC_1 = SOC_2 = \ldots = SOC_n = \frac{1}{n}\sum_{1}^{n} SOC_i \tag{3.3}$$

This can be expressed as

$$\mathbf{L}\mathbf{x}(\tau) = 0 \tag{3.4}$$

where

$$\mathbf{x}(\tau) = [SOC_1(\tau) \;\; SOC_2(\tau) \;\; \ldots \;\; SOC_n(\tau)]^T \tag{3.5}$$

$$\mathbf{L} = \left(\mathbf{I} - \frac{1}{n}\mathbf{1}\cdot\mathbf{1}^T\right) \tag{3.6}$$

Considering the average balancing command

$$\mathbf{v} = \mathbf{u}\tau = [i_{b1}\tau \;\; i_{b2}\tau \;\; \ldots \; i_{bn}\tau]^T \tag{3.7}$$

and the initial cell SOC states $\mathbf{x}(0)$, the equality constraint becomes

$$\mathbf{L}\mathbf{x}(0) + \mathbf{L}\frac{1}{Q}\mathbf{T}\mathbf{v} = 0 \tag{3.8}$$

When considering minimum plug-in charge time the equality constraint is modified to ensure that the SOC of each cell is 1, 100% fully charged, at time τ. This leads to a simplified equality constraint

$$\mathbf{x}(0) + \frac{1}{Q}\mathbf{T}\mathbf{v} = \mathbf{1} \tag{3.9}$$

Inequality constraints are needed to represent limits of balancing currents. This leads to the balancing current vector $\mathbf{u}$ to be subject to a constraint of the form $\mathbf{H}\mathbf{u} \leq \mathbf{k}$, multiplying both sides by the balancing time τ yields

$$[\mathbf{H} \ -\mathbf{k}] \begin{bmatrix} \mathbf{v} \\ \\ \tau \end{bmatrix} \leq 0 \tag{3.10}$$

When considering energy dissipatation, it should be noted that the balancing current vector should also contain absolute values of the balancing current, i.e. $\mathbf{u} = [i_{b1}, i_{b2}, \ldots, i_{bn}, |i_{b1}|, |i_{b2}|, \ldots, |i_{bn}|]^T$. The vector $[\mathbf{v}\ \tau]^T$ becomes the vector the linear programming optimization solver computes.

Two objective functions are possible, one related to balancing time, the other to energy dissipated. The solution to the formulated linear program provides the optimal balancing command for a topology considering different sets of initial conditions, e.g. varying spreads of cell SOC. To evaluate the worst-case performance of balancing time and energy dissipated of a topology more efficiently, an approach exploiting topology

symmetries is used (Preindl *et al.*, 2013). Instead of n^2 cases, this approach considers the following $n-1$ limiting extremes cases

$$\mathbf{x}(0) = \left(\frac{SOC_{high} - SOC_{low}}{2}\right) \begin{bmatrix} \mathbf{1}_{n-k} \\ -\mathbf{1}_k \end{bmatrix} + \left(\frac{SOC_{high} + SOC_{low}}{2}\right), k = 1, \ldots, n-1 \tag{3.11}$$

The objective function for computing the worst-case balancing time or plug-in charge time is

$$\max_{k \in \{1,\ldots,n-1\}} \min \quad \tau \tag{3.12}$$

The objective function for computing the worst-case energy dissipated of a topology is

$$\max_{k \in \{1,\ldots,n-1\}} \min \quad \sum_{i=1}^{n} (1-\eta) \left| i_{bi} \right| \tau \tag{3.13}$$

where η is the link efficiency of the topology. In this chapter, an efficiency of 90% is assumed.

3.3 Balancing Topologies

In this section, passive balancing and four inductor/transformer based topologies, depicted in Fig. 3.1, are considered. A topology matrix $\mathbf{T}$ is introduced for each case to describe the relation between balancing current and SOC. A linearized analysis is performed by simplifying the dynamic process of balancing to an average balancing current signal over the balancing time-scale from 0 to τ.

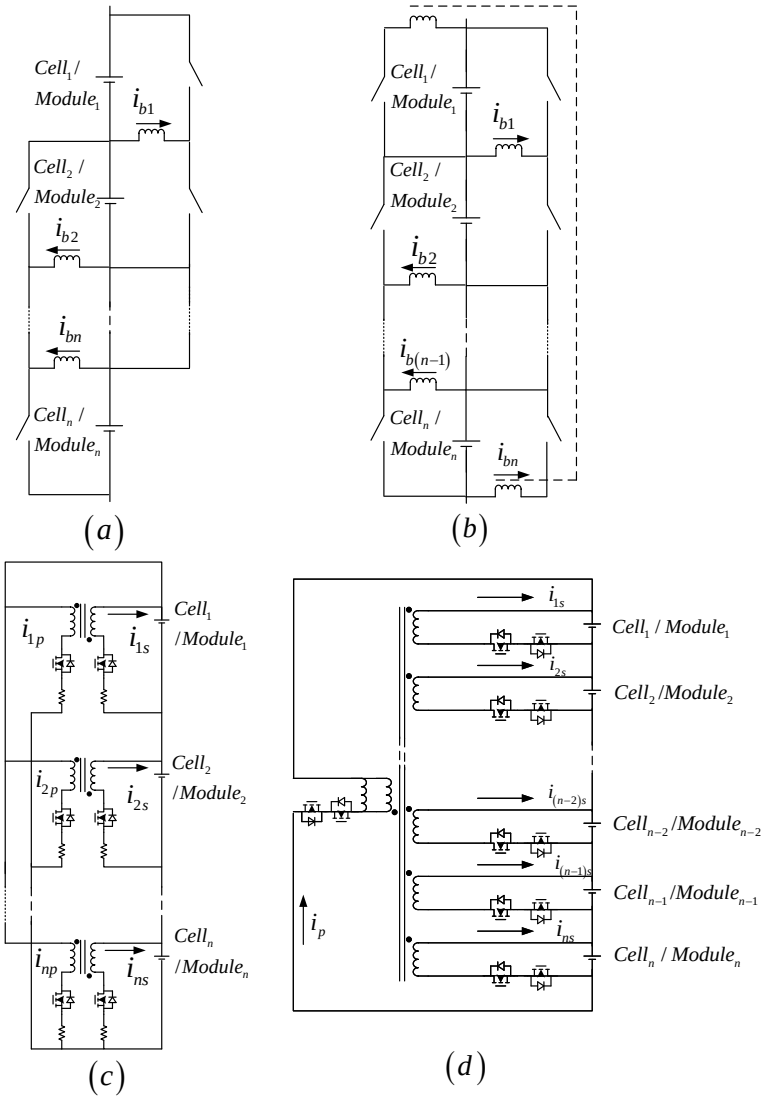

Figure 3.1: Four active balancing topologies a) Line Shunting b) Ring Shunting c) Sychronous Fly-back Converter d) Multi-winding transformer. Note each topology can balance a cell or a module.

3.3.1 Dissipative shunting

Conventional passive balancing dissipates energy through a shunting resistor for each cell. The topology matrix is a negative diagonal matrix $\mathbf{T} = diag([-1 \cdots -1])$. When balancing, the magnitude of the balancing currents i_{bi} is assumed to be constant, it value can be approximated as the nominal cell voltage divided by the shunting resistance. For a more fair comparison the same maximum magnitude is used for passive and active balancing, however charging current are not allowed when dissipative shunting is used. The inequality constraints can easily be modified to enforce this (Preindl *et al.*, 2013).

3.3.2 Line shunting

Line shunting topology is shown in Fig. 3.1(a). In this topology, charge of neighboring cells are moved by a converter (Nishijima *et al.*, 2000). Therefore, n cells in series need n-1 converters. The topology matrix for line shunting is

$$\mathbf{T} = \begin{bmatrix} 1 & & & & & \\ -1 & 1 & & & & \\ & -1 & 1 & & & \\ & & \ddots & \ddots & & \\ & & & -1 & 1 & \\ & & & & -1 & \end{bmatrix}_{n\times(n-1)} \tag{3.14}$$

The balancing current is limited by the current limits $|i_{bi}| \leq i_{limit,i}$. This leads to

the following inequality constraint

$$\overbrace{\begin{bmatrix} I_{n\times n} & -I_{n\times n} \\ -I_{n\times n} & -I_{n\times n} \\ 0_{n\times n} & I_{n\times n} \\ 0_{n\times n} & -I_{n\times n} \end{bmatrix}}^{\mathbf{H}} \begin{bmatrix} i_{b1} \\ \vdots \\ i_{bn} \\ i_{limit,1} \\ \vdots \\ i_{limit,n} \end{bmatrix} \leq \overbrace{\begin{bmatrix} 0_{n\times 1} \\ 0_{n\times 1} \\ 1_{n\times 1} \\ 0_{n\times 1} \end{bmatrix}}^{\mathbf{k}} \tag{3.15}$$

3.3.3 Ring shunting

The ring shunting topology is shown in Fig. 3.1(b). It is similar with line shunting, but the first cell and the last cell are connected by a fly-back converter (Preindl *et al.*, 2013). The topology matrix is given by

$$\mathbf{T} = \begin{bmatrix} 1 & & & & & -1 \\ -1 & 1 & & & & \\ & -1 & 1 & & & \\ & & \ddots & \ddots & & \\ & & & -1 & 1 & \end{bmatrix}_{n\times n} \tag{3.16}$$

The balancing current has the same limitation as with line shunting, so the matrix **H** and vector **k** are the same as with line shunting shown in (3.15).

3.3.4 Synchronous fly-back converter

Fig. 3.1(c) shows the circuit topology of synchronous fly-back converter based active balancing. Each cell in the string is connected with the entire module by an independent bidirectional synchronous fly-back converter (Corporation, 2013). The cell i is balanced by the secondary side current of the i^{th} fly-back converter i_{is} and the primary side current of all fly-back converters i_{ip}, where $i = 1, \ldots, n$. The cells SOC at terminal time τ is derived as

$$\begin{aligned} SOC_i(\tau) &= SOC_i(0) + \frac{1}{Q}\int_{t=0}^{\tau} i_{is}(t)dt \\ &\quad -\frac{1}{Q}\left(\int_{t=0}^{\tau} i_{1p}(t)dt + \ldots + \int_{t=0}^{\tau} i_{np}(t)dt\right) \end{aligned} \tag{3.17}$$

The relationship between average secondary side and primary side currents is given by $\mathbf{I}_s = n\mathbf{I}_p$. Therefore, the battery system in linear form is

$$\begin{bmatrix} SOC_1(\tau) \\ SOC_2(\tau) \\ \vdots \\ SOC_n(\tau) \end{bmatrix} = \begin{bmatrix} SOC_1(0) \\ SOC_2(0) \\ \vdots \\ SOC_n(0) \end{bmatrix} + \frac{1}{Q}\mathbf{T}\begin{bmatrix} i_{b1}\tau \\ i_{b2}\tau \\ \vdots \\ i_{bn}\tau \end{bmatrix} \tag{3.18}$$

where the topology matrix is

$$\mathbf{T} = \begin{bmatrix} 1-\frac{1}{n} & -\frac{1}{n} & \ldots & -\frac{1}{n} \\ -\frac{1}{n} & 1-\frac{1}{n} & \ldots & -\frac{1}{n} \\ \vdots & \vdots & \ddots & \vdots \\ -\frac{1}{n} & -\frac{1}{n} & \ldots & -1\frac{1}{n} \end{bmatrix} \tag{3.19}$$

Since the fly-back converters in the topology are independent, the balancing currents are also limited by (3.15).

3.3.5 Mulit-winding transformer

Multi-winding transformer based topology is shown in Fig. 3.1(d). It should be emphasized that only one secondary side winding works in one cycle (Bonfiglio and Roessler, 2009; Einhorn *et al.*, 2011; Yun *et al.*, 2013). In one cycle, one cell is active and other $n-1$ are inactive. The cells SOC are expressed by

$$SOC_i(k+1) = SOC_i(k) + \tfrac{1}{Q} i_{is}(t)dt - \tfrac{1}{Q} i_{ip}(t)dt \tag{3.20}$$

for one active winding, and

$$SOC_j(k+1) = SOC_j(k) - \tfrac{1}{Q} i_{jp}(t)dt \tag{3.21}$$

for n-1 inactive windings. Note $i \neq j$. Over a long time-scale τ, the state of charge of a cell can be expressed as

$$\begin{aligned} SOC_i(\tau) &= SOC_i(0) + \frac{1}{Q}\int_{t=0}^{\tau} i_{is}(t)dt \\ &\quad -\frac{1}{Q}\left(\underbrace{\int_{t=0}^{\tau} i_p(t)dt + \ldots + \int_{t=0}^{\tau} i_p(t)dt}_{n}\right) \end{aligned} \tag{3.22}$$

The topology matrix of the multi-winding transformer is derived in the same form as the synchronous fly-back converter. However since there is only one active winding in one cycle, the balancing currents should be limited by additional constraints $|i_{bi}| \leq$

$i_{limit,i}$ and $\sum_{i=1}^{n} i_{bi} \leq i_{limit,i}$. The overall inequality constraint is

$$\begin{bmatrix} I_{n\times n} & -I_{n\times n} \\ -I_{n\times n} & -I_{n\times n} \\ 0_{n\times n} & I_{n\times n} \\ 0_{n\times n} & -I_{n\times n} \\ 0_{1\times n} & 1_{1\times n} \end{bmatrix} \begin{bmatrix} i_{b1} \\ \vdots \\ i_{bn} \\ i_{limit,1} \\ \vdots \\ i_{limit,n} \end{bmatrix} \leq \begin{bmatrix} 0_{n\times 1} \\ 0_{n\times 1} \\ 1_{n\times 1} \\ 0_{n\times 1} \\ 1 \end{bmatrix} \tag{3.23}$$

3.4 Battery Pack Balancing Analysis

The overall topology of the battery pack structure, from cell to module and from module to pack, will affect the balancing performance. If a battery pack has 96 cells in series, e.g. Fig. 3.2, there are many ways to integrate multiple cells in a module and then integrate modules to form a pack. In this chapter, four kinds of configurations are considered, these include 6x16, 8x12, 12x8 and 16x6 arrangements where the former is the number of modules and the latter is cells per module. The four active topologies considered in this chapter generate 16 combinations of pure active balancing pack topologies. In addition, 8 mixed two-level passive/active balancing topologies are also considered. One passive balancing only topology is used as a benchmark.

To consider different battery pack architectures, the topology matrix for battery pack needs to be modified to account for the two level structuring. Cell SOC balanced via two levels is given by

$$SOC(\tau) = SOC(0) + \frac{1}{Q}\int i_b^{module}(t)dt + \frac{1}{Q}\int i_b^{pack}(t)dt \tag{3.24}$$

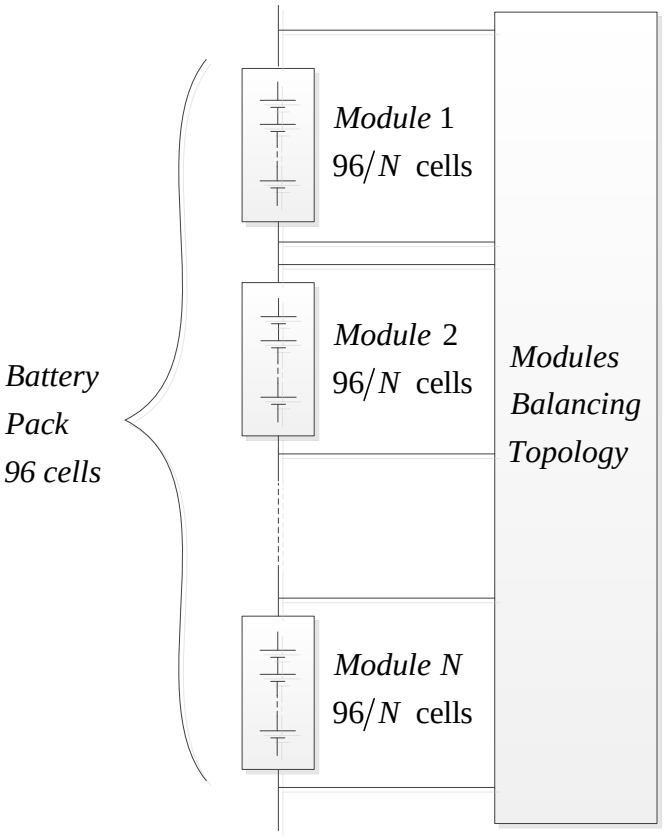

Figure 3.2: Battery pack two level balancing topology

The last two terms are controllable balancing currents in module level and pack level respectively. If a 96 cell battery pack consists of m modules and each module contains

n cell, the SOCs of the battery pack can be presented by

$$\begin{bmatrix} SOC_1(\tau) \\ \vdots \\ SOC_{96}(\tau) \end{bmatrix} = \begin{bmatrix} SOC_1(0) \\ \vdots \\ SOC_{96}(0) \end{bmatrix} + \frac{1}{Q} \begin{bmatrix} \mathbf{T}_m & & \\ & \ddots & \\ & & \mathbf{T}_m \end{bmatrix} \mathbf{T}_p \begin{bmatrix} i_{b1}^{module}\tau \\ \vdots \\ i_{b96}^{module}\tau \\ i_{b1}^{pack}\tau \\ \vdots \\ i_{bm}^{pack}\tau \end{bmatrix} \tag{3.25}$$

where $\mathbf{T}_m$ and $\mathbf{T}_p$ represent topology matrices that are described in Section 3.3. Subscript m and p denote module and pack levels, respectively. Topology matrices of these different complete pack balancing configurations are built in Matlab script and solved using linprog (Mathworks, 1998). Parameters of battey pack are summarized in Table 3.1.

Table 3.1: Parameters of battery pack

Number of cells	96
Number of modules	m
Number of cells per module	n
Maximum module/cell level balancing current	5A
Maximum initial SOC deviation	10%

3.4.1 Performance in idle mode

Performance of balancing topologies in idle mode, zero pack current, are analyzed in this section. Constraints (3.8) and (3.10) are employed. Figure 3.3a) and b) show the

worst-case balancing time and the worst-case energy dissipation for different balancing combinations. Note that the x-axis represents one passive cell balancing topology, 16 active balancing combinations, and 8 mixed balancing combinations. The capital letter before slash represents module level balancing topology and the capital letter after slash represents pack level balancing topology. D is dissipative shunting resistor as passive balancing topology, L is line shunting, R is ring shunting, F is synchronous fly-back, and M is multi-winding transformer. Four shaded bars denote 6, 8, 12, and 16 modules structures from dark blue to light blue.

From results of these two plots, passive balancing topology has fast balancing time, but high energy loss. The multi-winding transformer topology leads to slow balancing time, because of only one channel working in one cycle. Combinations between ring shunting and synchronous fly-back converter have nice performance from these two aspects. As mixed balancing topologies, F/D configurations can provide fast balancing time. Considering energy loss, D/F and D/M topologies with 16 modules outperform other mixed configurations. The shortest balancing time is 0.4 hour from combination of F/F. The lowest energy loss is 66Wh from combination F/R with six modules.

3.4.2 Performance in plug-in charge mode

The effect of balancing topology on the plug-in charge process is described here. It is assumed the battery pack is balanced at or before its fully charged state. A constant current $\frac{1}{4}$C mode pack charging scheme is assumed. These assumptions ensure feasibility of the combined charging and balancing process in terms of the simplified linear programming based analysis. The constraints employed are (3.9)

and (3.10).

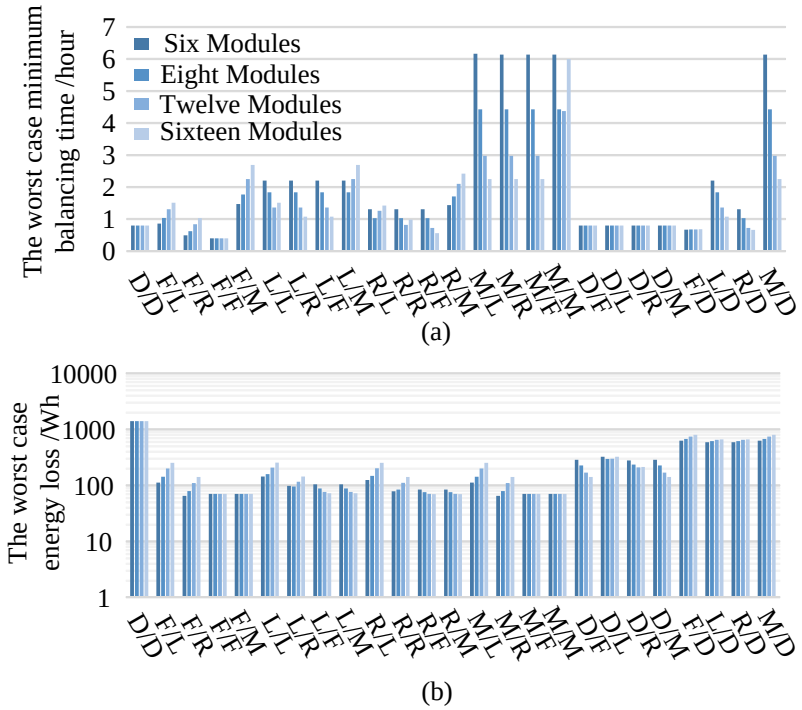

Figure 3.3: Idle-mode performance analysis a) The worst-case minimum balancing time b) The worst-case minimum energy loss.

A subset of 16 topologies are considered. The performance of 15 active-balancing enabled topologies are compared with the passive balancing topology as shown in Fig. 3.4. The results depicted in Fig. 3.4a) indicates the active balancing topologies can slightly shorten the worst case charging time. This arises since the most energy is lost during the charging process as depicted in Fig. 3.4. Active balancing enabled topologies can recover this energy to charge other cells.

3.4.3 Component counts

Major components needed for the active balancing enabled topologies are summarized in Table 3.2. Circuits containing passive balancing are the cell or module level use

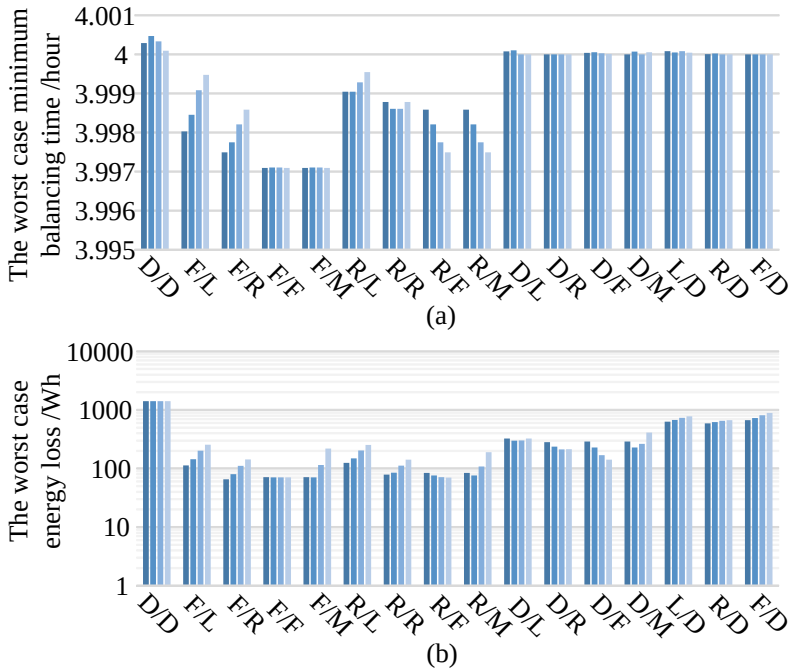

Figure 3.4: Plug-in charge mode performance analysis a) The worst-case minimum balancing time b) The worst-case minimum energy loss.

fewer components.

3.5 Conclusions

From the above analysis, overall battery pack balancing topologies can be evaluated considering balancing time, energy loss, effect on plug-in charge and component counts. A subset of 5 top performing two-level balancing topologies are compared, two are pure active balancing topologies, two are mixed balancing topologies, and remaining is pure passive balancing topology. There are compared graphically in Fig. 3.5. In the radar chart, the scoring is from 0 to 1 to represent bad to good comparative performance. Balancing time and enengy loss in two modes of F/F with 6 modules and F/R with 6 modules outperform others. Compared with other mixed topologies, F/D with 6 modules has the fastest balancing time. The passive balancing

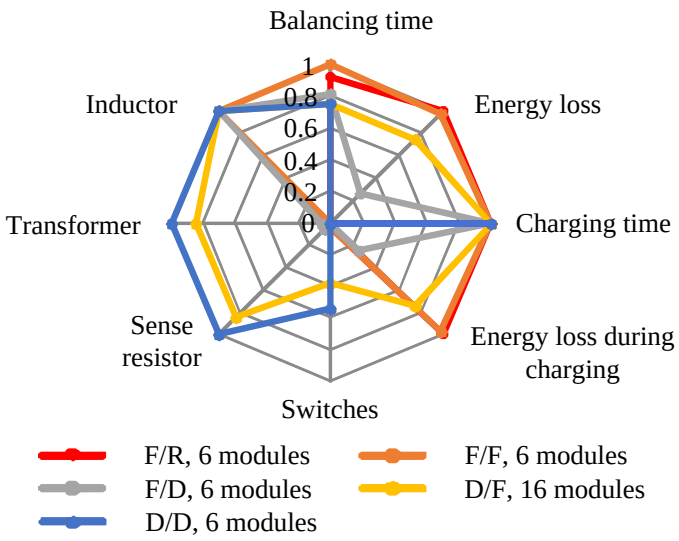

Figure 3.5: Comparison of top performing designs.

topology and D/F with 16 modules need less components than others.

A linear programming based balancing topology analysis method is presented and applied to the design of a complete battery pack balancing topology. A two-level modular design approach is considered in the analysis. Performances of different battery pack structures and balancing topologies are compared. The method is applicable to other balancing topologies with controllable current.

Table 3.2: Component Counts

Tops	Number of switches	Number of sensor resistors	Number of inductors/ transformers
F/L	$2n \cdot m + 2(m-1)$	$2n \cdot m + (m-1)$	$m-1$ indcutors, $n \cdot m$ 2-winding transformers
F/R	$2n \cdot m + 2m$	$2n \cdot m + m$	$m-1$ indcutors, $n \cdot m+1$ 2-winding transformers
F/F	$2n \cdot m + 2m$	$2n \cdot m + 2m$	$n \cdot m + m$ 2-winding transformers
F/M	$2n \cdot m + 2(m+1)$	$2n \cdot m + m$	$n \cdot m$ 2-winding transformers, 1 m-winding transformer
L/L	$2(n-1) \cdot m + 2(m-1)$	$(n-1) \cdot m + (m-1)$	$(n-1) \cdot m + m - 1$ inductors
L/R	$2(n-1) \cdot m + 2m$	$(n-1) \cdot m + m$	$(n-1) \cdot m + m - 1$ inductors, 1 2-winding transformer
L/F	$2(n-1) \cdot m + 2m$	$(n-1) \cdot m + 2m$	$(n-1) \cdot m$ inductors, m 2-winding transformers
L/M	$2(n-1) \cdot m + 2(m+1)$	$(n-1) \cdot m + 1$	$(n-1) \cdot m$ inductors, 1 m-winding transformer
R/L	$2n \cdot m + 2(m-1)$	$n \cdot m + (m-1)$	$(n-1) \cdot m + m - 1$ inductors, m 2 winding-transformers
R/R	$2n \cdot m + 2m$	$n \cdot m + m$	$(n-1) \cdot m + m - 1$ inductors, $m+1$ 2 winding-transformers
R/F	$2n \cdot m + 2m$	$n \cdot m + 2m$	$(n-1) \cdot m$ inductors, $2m$ 2-winding transformers
R/M	$2n \cdot m + 2(m+1)$	$n \cdot m + 1$	$(n-1) \cdot m$ indcutors, m 2-winding transformers, 1 m-winding transformer
M/L	$2(n-1) \cdot m + 2(m-1)$	$m + m - 1$	$m-1$ inductors, m n-winding transformers
M/R	$2(n-1) \cdot m + 2m$	$m + m$	$m-1$ inductors, 1 2-winding transformer, m n-winding transformers
M/F	$2(n-1) \cdot m + 2m$	$m + 2m$	m 2-winding transformers, m n-winding transformers
M/M	$2(n-1) \cdot m + 2(m+1)$	$m + 1$	1 m-winding transformer, m n-winding transformers
D/F	$n \cdot m + 2m$	$n \cdot m + 2m$	m 2-winding transformers
D/L	$n \cdot m + 2(m-1)$	$n \cdot m + (m-1)$	$m-1$ inductors
D/R	$n \cdot m + 2m$	$n \cdot m + m$	$m-1$ inductors, m n-winding transformers
D/M	$n \cdot m + 2(m+1)$	$n \cdot m + 1$	1 m-winding transformer
F/D	$2n \cdot m + m$	$2n \cdot m + n \cdot m$	$n \cdot m$ 2-winding transformers
L/D	$2(n-1)m + m$	$(n-1)m + n \cdot m$	(n-1)m inductors
R/D	$2n \cdot m + m$	$2n \cdot m$	$(n-1)m$ inductors, m 2-winding transformers
M/D	$2(n+1)m + m$	$m + n \cdot m$	m n-winding transformers

Chapter 4

Battery and Ultracapacitor Modeling Technologies and States Estimation

4.1 Introduction

An accurate energy storage device modeling is the fundamental of a systematic energy management system. An equivalent circuit modeling (ECM) is extensively used in the battery management system (BMS) of portable electronics since the accuracy of the equivalent circuit modeling is adequate for these applications. Although the equivalent circuit modeling technologies have been extended to lithium-ion batteries as the traction batteries in electrified vehicles, this modeling approach reveals poor performance during the battery operates in a small SOC range with high charge/discharge current (Chaturvedi *et al.*, 2010). In order to compensate these drawbacks and approximate the nonlinear behavior of a battery, the parameters in an equivalent circuit

modeling need to be fitted as functions of SOC, temperature, amplitude of the input current, and direction of the input current. This chapter reviews the equivalent circuit modeling technologies and states estimation algorithms based on extended Kalman filter.

One of the main contributions in the research is to develop the single particle model of BMS in automotive applications. In this chapter, the pseudo-two dimensional model and several reduced order model technologies are explained in details. In order to take advantages of the physics-based model in an electrified vehicle and simplify the model, the single particle model is developed for the battery management system. The definitions of the open circuit voltage, state of charge, capacity, and current in a single particle model are explained. As the numerical methods for solving differential equations, the finite difference method and discretization method for solving the diffusion equations in the negative and positive electrodes are illustrated. A parametrization method for a single particle model in a lithium-ion battery cell which reduces the number of fitted variables and simplifies the fitting process is proposed. The solid electrolyte interface (SEI) layer growth phenomena as a main battery aging mechanism is modeled and integrated with the single particle model. The capacity fade from the single particle model and the SEI layer growth model are validated by the experimentally observed capacity fade and resistance growth.

As a battery model in BMS in an automotive application, SOC and SOH for the single particle model are also developed. In this chapter, a hybrid SPM which has the strong observability with EKF is proposed for SOC estimation. To estimate SOH of battery, the internal impedance is estimated by EKF which is integrated into the SOC estimation EKF. The SOC and SOH estimation results are compared with the

experimental results.

Similar to the lithium-ion battery, the ultracapacitor also needs an accurate model to simulate the extremely high current capability. Different modeling technologies are reviewed in this chapter. Based on an equivalent circuit model, parametrization for the ultracapacitor model is also discussed.

4.2 Equivalent circuit modeling and states estimation for lithium-ion battery

4.2.1 Equivalent circuit modeling

The different models are derived from a basic equivalent circuit modeling which includes: an open circuit voltage (OCV) that is a function of SOC, an ohmic resistance and RC elements that reflect the dynamics of the batteries. Of the different ECMs available in the literature, the two main models depicted in Fig. 4.1 get more attention. In the Fig. 4.1, V_{oc} is the OCV, R_o is the ohmic resistance. The in series RC networks can represent battery polarization/dynamic effects and transient responses. V and I are the terminal voltage and terminal current, respectively. Positive current indicates discharging.

The OCV curve is a function of SOC as shown in Fig. 4.2 which can be measured from the Hybrid Pulse Power Characterization (HPPC) test. SOC indicates the percentage of remaining charge in the battery. The discrete time equations for calculating SOC are

$$SOC_k = SOC_{k-1} + \frac{I_{k-1}\Delta t}{Cap} \tag{4.1}$$

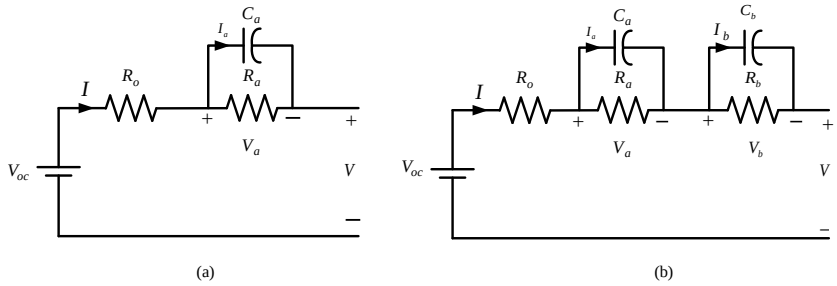

Figure 4.1: equivalent circuit modeling for battery (a) 1RC ECM, (b) 2RC ECM

In the Fig. 4.1 (a), there is only one RC pair. R_a and C_a are the resistance and capacitance, respectively. I_a and V_a are the current through C_a and its voltage, respectively. The continuous time dynamics are

$$\begin{aligned} \dot{V}_a &= -\frac{V_a}{R_a C_a} + \frac{I}{C_a} \\ V &= V_{oc} - V_a - IR_o \end{aligned} \tag{4.2}$$

In the Fig. 4.1 (b), one more RC pair is added to increase accuracy. The continuous time dynamics for the 2RC ECM are similar and take the form of

$$\begin{aligned} \dot{V}_a &= -\frac{V_a}{R_a C_a} + \frac{I}{C_a} \\ \dot{V}_b &= -\frac{V_b}{R_b C_b} + \frac{I}{C_b} \\ V &= V_{oc} - V_a - V_b - IR_o \end{aligned} \tag{4.3}$$

From above equation, the discrete time-domain equation can be derived. The simplest approach is based on Zero-Order-Hold (ZOH) of the input I where it is held constant during the integration interval. For the model with 1RC network using the

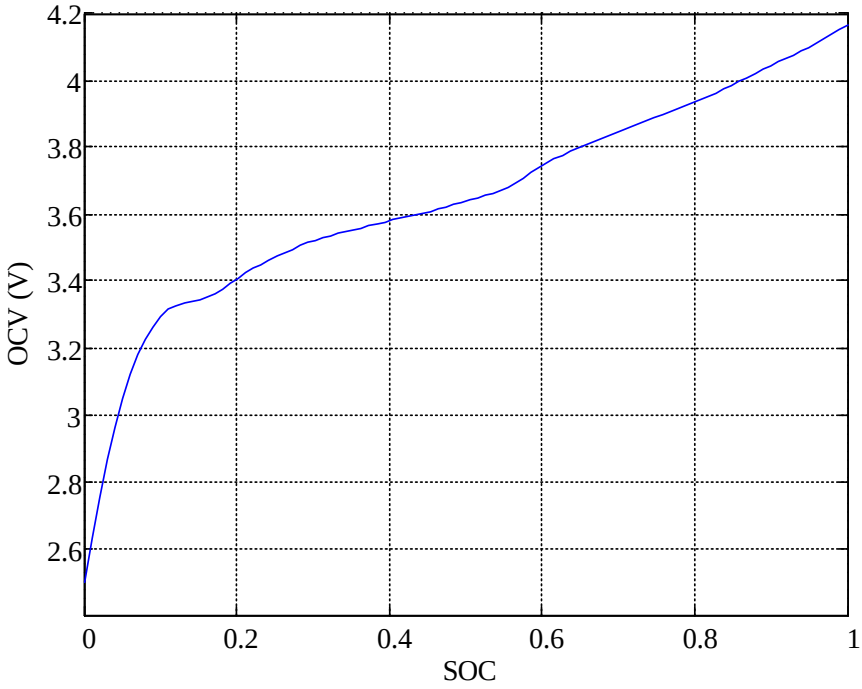

Figure 4.2: Open circuit voltage

ZOH based approach one can derive.

$$\begin{aligned} V_{a,k} &= e^{-\frac{\Delta t}{R_a C_a}} V_{a,k-1} + R_a(1 - e^{-\frac{\Delta t}{R_a C_a}}) I_{k-1} \\ V_k &= V_{oc,k} - V_{a,k} - I_k R_o \end{aligned} \tag{4.4}$$

For the model with 2RC network using the ZOH based approach is

$$\begin{aligned} V_{a,k} &= e^{-\frac{\Delta t}{R_a C_a}} V_{a,k-1} + R_a(1 - e^{-\frac{\Delta t}{R_a C_a}}) I_{k-1} \\ V_{b,k} &= e^{-\frac{\Delta t}{R_b C_b}} V_{b,k-1} + R_b(1 - e^{-\frac{\Delta t}{R_b C_b}}) I_{k-1} \\ V_k &= V_{oc,k} - V_{a,k} - V_{b,k} - I_k R_o \end{aligned} \tag{4.5}$$

To obtain a high accuracy, more RC pairs could be added to mimic the nonlinear

characteristics. Lithium-ion batteries show asymmetrical transient/dynamic behavior between charging and discharging, therefore applying asymmetric resistances to the ECM can improve the accuracy. In the next subsection, parameters identification would be introduced.

4.2.2 Parameters identification

Besides the open circuit voltage is a function of SOC, the ohmic resistance and dynamic resistance in RC pairs are variables with respect to SOC, temperature, magnitude of current, and direction of current. These parameters need to be fitted by the offline parameters identification based on the HPPC test. Fig. 4.3 shows the voltage and current profiles of an NCR18650A cell under HPPC test. The OCV-SOC curve

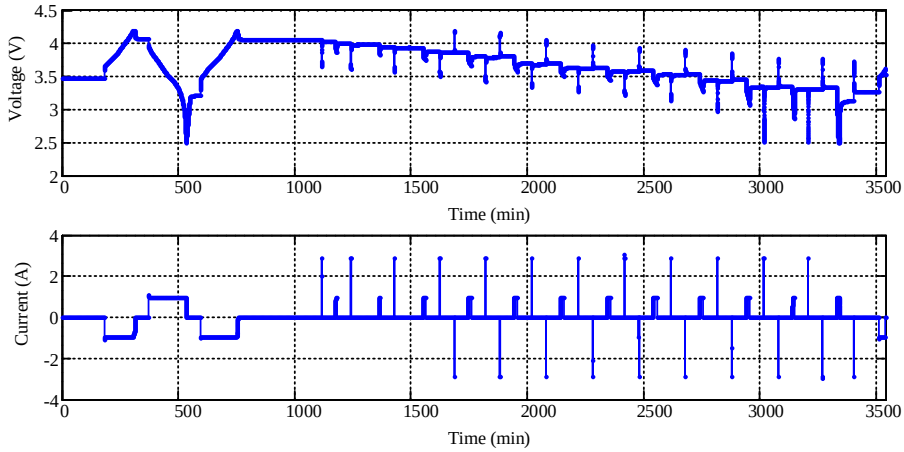

Figure 4.3: Hybrid Power Pulse Characterization voltage and current curves of NCR18650A cell

could be measured by the HPPC test. From the pulse responses in the test, the ohmic resistance and parameters in RC pairs in ECM could be fitted by numerical optimization. In this subsection, an asymmetric 3RC ECM is used to approach the

dynamic performance of the NCR18650A cell. Fitted pulse responses at 95%, 70%, 35%, and 5% SOC are shown in Fig. 4.4. The mean absolute error crosses the entire operating range can achieve 1.6245mV. The changing of ohmic resistance (R_o) and

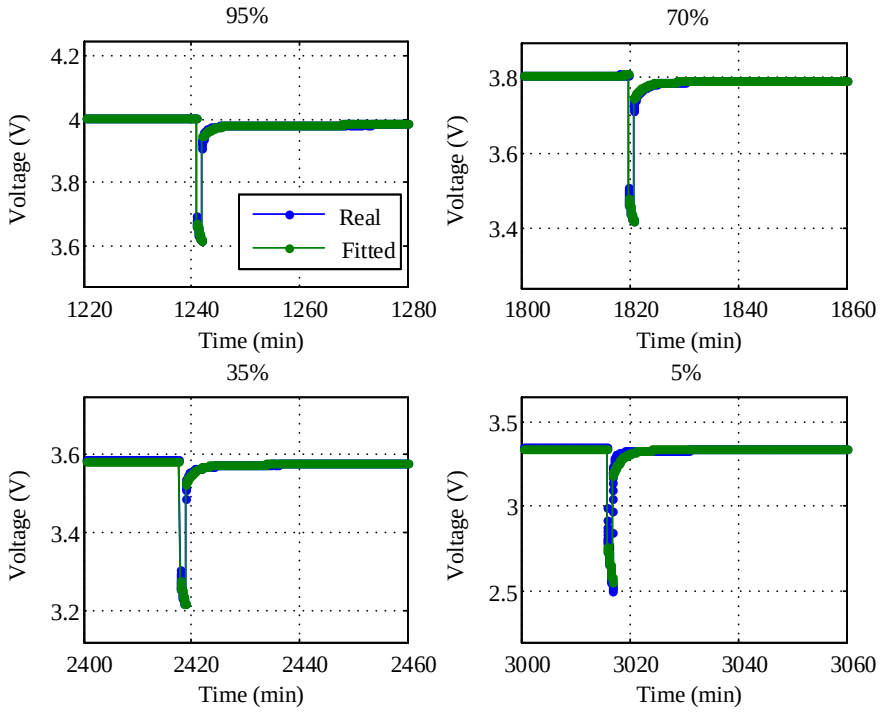

Figure 4.4: Fitted result at 95%, 70%, 35%, and 5% SOC

dynamic resistance (R_a, R_b, and R_c) with respect to SOC could be observed from Fig. 4.5.

4.2.3 States estimation based on equivalent circuit modeling

Online battery state estimation approaches using equivalent circuit modeling with algorithms based on derivatives of Kalman filter (KF) are popular. Due to the non-linear relationship between the OCV and SOC, extended Kalman filter is forced to

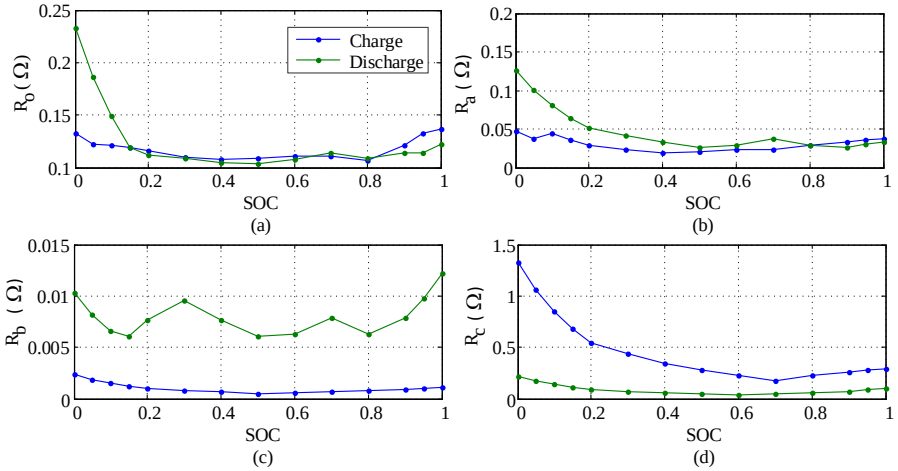

Figure 4.5: Fitted NCR18650A cell resistances (a) R_o, (b) R_a, (c) R_b, (d) R_c

estimate states/parameters in 1RC and 2RC ECM. Rather than estimate SOC directly, the OCV V_{oc} is first estimated and then passed through an OCV-SOC look-up table to obtain SOC.

Firstly, the KF and EKF estimation algorithms are recalled. The KF embeds a model into the filter and uses it to predict an intermediate state estimate. A discrete-time state-space model of the following form is assumed

$$\mathbf{x}_k = \mathbf{A}_{k-1}\mathbf{x}_{k-1} + \mathbf{B}_{k-1}\mathbf{u}_{k-1} + \mathbf{w}_{k-1} \tag{4.6}$$

$$\mathbf{y}_k = \mathbf{C}_k\mathbf{x}_k + \mathbf{D}_k\mathbf{u}_k + \mathbf{v}_k \tag{4.7}$$

where $\mathbf{x}_k \in \Re^n$ is a to be estimated system state vector at time k, and $\mathbf{u}_k \in \Re^p$ is a known input vector, $\mathbf{y}_k \in \Re^m$ a measurement vector, and $\mathbf{w}_k \in \Re^n$ and $\mathbf{v}_k \in \Re^m$ represent the process noise and measurement noise, respectively.

The KF is an optimal estimator (Kalman *et al.*, 1960) under the assumption of normally distributed, zero mean, and independent process and measurement noise,

i.e. with probability distributions

$$P(\mathbf{w}) \sim \mathcal{N}(0, \mathbf{Q}), \quad P(\mathbf{v}) \sim \mathcal{N}(0, \mathbf{R}) \tag{4.8}$$

where $\mathbf{Q}$ is the process noise covariance and $\mathbf{R}$ is the measurement noise covariance. The mechanics of the KF are summarized in Table 4.1.

Table 4.1: KF Algorithm

Step	Equation
1. A priori covariance update	$\mathbf{P}_{k\|k-1} = \mathbf{A}_{k-1}\mathbf{P}_{k-1\|k-1}\mathbf{A}_{k-1}^T + \mathbf{Q}_{k-1}$
2. A priori estimate prediction	$\hat{\mathbf{x}}_{k\|k-1} = \mathbf{A}_{k-1}\hat{\mathbf{x}}_{k-1\|k-1} + \mathbf{B}_{k-1}\mathbf{u}_{k-1}$
3. Kalman gain matrix calculation	$\mathbf{K}_k = \mathbf{P}_{k\|k-1}{\mathbf{C}_k}^T(\mathbf{C}_k\mathbf{P}_{k\|k-1}\mathbf{C}_k^T + \mathbf{R}_k)^{-1}$
4. A posteriori covariance update	$\mathbf{P}_{k\|k} = (\mathbf{I} - \mathbf{K}_k\mathbf{C}_k)\mathbf{P}_{k\|k-1}$
5. A posteriori estimate correction	$\hat{\mathbf{x}}_{k\|k} = \hat{\mathbf{x}}_{k\|k-1} + \mathbf{K}_k(\mathbf{y}_k - \mathbf{C}_k\hat{\mathbf{x}}_{k\|k-1} - \mathbf{D}_k\mathbf{u}_k)$

In the time update steps 1 and 2, a priori state and a priori covariance are predicted from time $k-1$ to time k. During the measurement update steps 3 to 5, the Kalman gain matrix $\mathbf{K}_k$ is used to obtain a posteriori covariance matrix and state estimate.

Consider a nonlinear system of the form

$$\mathbf{x}_k = f(\mathbf{x}_{k-1}, \mathbf{u}_{k-1}) + \mathbf{w}_{k-1} \tag{4.9}$$

$$\mathbf{y}_k = g(\mathbf{x}_k, \mathbf{u}_k) + \mathbf{v}_k \tag{4.10}$$

where $f(\cdot)$ and $g(\cdot)$ are nonlinear functions, and $\mathbf{w}_k$ and $\mathbf{v}_k$ are process and measurement noise vectors. For such nonlinear systems, a modified KF that linearizes around the state estimates can be used. It is referred to as the EKF (Welch and Bishop, 2006) and for nonlinear systems it becomes a sub-optimal filter.

For EKF the nonlinear functions of $f(\cdot)$ and $g(\cdot)$ are used for prediction, however covariance matrix updates and Kalman gain calculation employ linearized Jacobian matrices of $f(\cdot)$ and $g(\cdot)$ as follows

$$\mathbf{A}_k = \left.\frac{\partial f(\mathbf{x}, \mathbf{u}_k)}{\partial \mathbf{x}}\right|_{\mathbf{x}=\hat{\mathbf{x}}_{k|k}}, \mathbf{C}_k = \left.\frac{\partial g(\mathbf{x}, \mathbf{u}_k)}{\partial \mathbf{x}}\right|_{\mathbf{x}=\hat{\mathbf{x}}_{k|k-1}} \tag{4.11}$$

The mechanics of the EKF are similar to KF and are illustrated in Table 4.2

Table 4.2: EKF Algorithm

Step	Equation
1. A priori linearization	$\mathbf{A}_{k-1} = \frac{\partial f(\mathbf{x}, \mathbf{u}_{k-1})}{\partial \mathbf{x}}\|_{\mathbf{x}=\hat{\mathbf{x}}_{k-1\|k-1}}$
2. A priori covariance update	$\mathbf{P}_{k\|k-1} = \mathbf{A}_{k-1}\mathbf{P}_{k-1\|k-1}\mathbf{A}_{k-1}^T + \mathbf{Q}_{k-1}$
34. A posteriori linearization	$\mathbf{C}_k = \frac{\partial g(\mathbf{x}, \mathbf{u}_k)}{\partial \mathbf{x}}\|_{\mathbf{x}=\hat{\mathbf{x}}_{k\|k-1}}$
5. Kalman gain matrix calculation	$\mathbf{K}_k = \mathbf{P}_{k\|k-1}{\mathbf{C}_k}^T(\mathbf{C}_k\mathbf{P}_{k\|k-1}\mathbf{C}_k^T + \mathbf{R}_k)^{-1}$
67. A posteriori estimate correction	$\hat{\mathbf{x}}_{k\|k} = \hat{\mathbf{x}}_{k\|k-1} + \mathbf{K}_k(\mathbf{y}_k - g(\hat{\mathbf{x}}_{k\|k-1}, \mathbf{u}_k))$

The states estimation algorithms for 1RC and 2RC ECM are presented in the remainder of this subsection.

- EKF method - symmetric resistances in 1RC CEM

  The vector to be estimated is $\mathbf{x} = [V_a, V_{oc}, R_o, R_a, \theta]^T$ where $\theta = e^{-\frac{\Delta t}{R_a C_a}}$. According to the nonlinear relationship between the OCV and SOC, V_{oc} can be modeled as

$$\begin{aligned} V_{oc,k} &= V_{oc,k-1} + dV_{oc,k-1} \\ &= V_{oc,k-1} - \frac{dV_{oc,k-1}}{dSOC}\frac{\Delta t I_{k-1}}{Cap} \end{aligned} \tag{4.12}$$

From (4.4) and (4.12), the state-space form is

$$\begin{aligned}
\begin{bmatrix} V_{a,k} \\ V_{oc,k} \\ R_{o,k} \\ R_{a,k} \\ \theta_k \end{bmatrix} &= \begin{bmatrix} e^{-\frac{\Delta t}{R_a C_a}} V_{a,k-1} + R_a(1 - e^{-\frac{\Delta t}{R_a C_a}}) I_{k-1} \\ V_{oc,k-1} + dV_{oc,k-1} \\ R_{o,k-1} \\ R_{a,k-1} \\ \theta_{k-1} \end{bmatrix} + \mathbf{w}_{k-1} \\
V_k &= V_{oc,k} - V_{a,k} - I_k R_o + \mathbf{v}_{k-1}
\end{aligned} \tag{4.13}$$

The linearized Jacobian matrices of $f(\cdot)$ and $g(\cdot)$ to be used with EKF are

$$\begin{aligned}
\mathbf{A}_k &= \begin{bmatrix} \theta_k & 0 & 0 & (1-\theta_k)I_k & V_{a,k} - R_{a,k} I_k \\ 0 & 1 & 0 & 0 & 0 \\ 0 & 0 & 1 & 0 & 0 \\ 0 & 0 & 0 & 1 & 0 \\ 0 & 0 & 0 & 0 & 1 \end{bmatrix} \\
\mathbf{C}_k &= \begin{bmatrix} -1 & 1 & -I_k & 0 & 0 \end{bmatrix}
\end{aligned} \tag{4.14}$$

- EKF method - symmetric resistances in 2RC CEM

  The vector to be estimated is $\mathbf{x} = [V_a, V_b, V_{oc}, R_o, R_a, R_b, \theta_a, \theta_b]^T$ where $\theta_a =$

$e^{-\frac{\Delta t}{R_a C_a}}$ and $\theta_b = e^{-\frac{\Delta t}{R_b C_b}}$. From (4.5) and (4.12), the state-space form is

$$\begin{bmatrix} V_{a,k} \\ V_{b,k} \\ V_{oc,k} \\ R_{o,k} \\ R_{a,k} \\ R_{b,k} \\ \theta_{a,k} \\ \theta_{b,k} \end{bmatrix} = \begin{bmatrix} e^{-\frac{\Delta t}{R_a C_a}} V_{a,k-1} + R_a(1 - e^{-\frac{\Delta t}{R_a C_a}}) I_{k-1} \\ e^{-\frac{\Delta t}{R_b C_b}} V_{b,k-1} + R_b(1 - e^{-\frac{\Delta t}{R_b C_b}}) I_{k-1} \\ V_{oc,k-1} + dV_{oc,k-1} \\ R_{o,k-1} \\ R_{a,k-1} \\ R_{b,k-1} \\ \theta_{a,k-1} \\ \theta_{b,k-1} \end{bmatrix} + \mathbf{w}_{k-1}$$

$$V_k = V_{oc,k} - V_{a,k} - V_{b,k} - I_k R_o + \mathbf{v}_{k-1} \tag{4.15}$$

The linearized Jacobian matrices of $f(\cdot)$ and $g(\cdot)$ to be used with EKF are

$$\mathbf{A}_k = \begin{bmatrix} \theta_{a,k} & 0 & 0 & 0 & (1-\theta_{a,k})I_k & 0 & V_{a,k} - R_{a,k} I_k & 0 \\ 0 & \theta_{b,k} & 0 & 0 & 0 & (1-\theta_{b,k})I_k & 0 & V_{a,k} - R_{a,k} I_k \\ 0 & 0 & 1 & 0 & 0 & 0 & 0 & 0 \\ 0 & 0 & 0 & 1 & 0 & 0 & 0 & 0 \\ 0 & 0 & 0 & 0 & 1 & 0 & 0 & 0 \\ 0 & 0 & 0 & 0 & 0 & 1 & 0 & 0 \\ 0 & 0 & 0 & 0 & 0 & 0 & 1 & 0 \\ 0 & 0 & 0 & 0 & 0 & 0 & 0 & 1 \end{bmatrix}$$

$$\mathbf{C}_k = \begin{bmatrix} -1 & 1 & 1 & -I_k & 0 & 0 & 0 & 0 \end{bmatrix} \tag{4.16}$$

The results for SOC and ohmic resistance estimation using the methods are presented with experimental measurements on a lithium-ion cell. The initial condition assumes SOC has +5% error and R_o is 0.3Ω. Fig. 4.6 compares the estimated SOC of 1RC and 2RC ECM with the real SOC. After around 30 seconds, the estimated SOCs can catch the real SOC. The maximum absolute error of the 1RC ECM is 4.6% and the mean absolute error of it is 0.67%. The maximum absolute error of the 2RC ECM is 4.75% and the mean absolute error of it can achieve 0.51%. The ohmic resistance estimation results of 1RC and 2RC ECM are depicted and compared with an off-line fitted R_o in Fig. 4.7. The estimation algorithms provide an instant approach to evaluate the state of health of the battery.

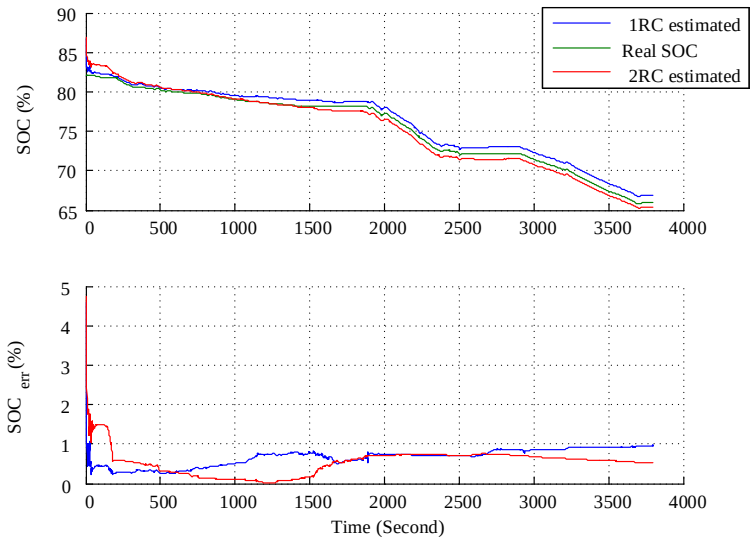

Figure 4.6: SOC estimation results of 1RC and 2RC ECM compare with real SOC

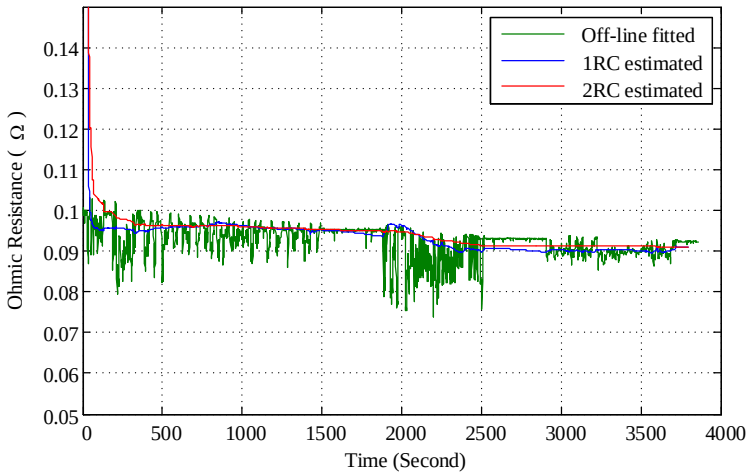

Figure 4.7: Ohmic resistance R_o estimation results of 1RC and 2RC ECM compare with off-line fitted R_o

4.3 Physics-based modeling technologies for lithium-ion battery

4.3.1 Pseudo-two dimensional model

An electrochemical-based model is a good candidate to observe internal states of a lithium-ion cell because this model reflects the chemical reaction in the battery. Doyle et al. (Doyle *et al.*, 1993, 1996; Fuller *et al.*, 1994) developed a pseudo-two dimensional (P2D) model which considers major electrochemical processes such as:

- Fick's law of diffusion in solid phase
- Ion transport in electrolyte phase
- Ohm's law at both phases
- Electrode kinetics at SEI layer

It is emphasized that this P2D model is a simplification of an actual 3D model. The two dimensions in the P2D model are the micro-scale layering thickness (x-axis), that is along the cell sandwich from one collector to another collector and a pseudo-axis r which represents the radius distance of a so-called representative spherical particle used to model the solid phase at each electrode, as shown in Fig.4.8. The typical battery cathode or anode along the x-axis has a length scale of 50-100 μm (Gully *et al.*, 2014). The others two dimensions (y and z-axis) are neglected because they are orders of magnitude larger (Ahmed *et al.*, 2014a; Newman and Tiedemann, 1975). The governing equations of P2D can present lithium ion concentration in solid (electrode) phase c_s and electrolyte phase c_e, potential of solid phase ϕ_s and potential of electrolyte phase ϕ_e.

Diffusion of lithium-ion in a spherical active material particle is modeled by Fick's second diffusion equation (Jacobsen and West, 1995):

$$\frac{\partial c_{s,i}(x,r,t)}{\partial t} = \frac{D_{s,i}}{r^2}\frac{\partial}{\partial r}\left(r^2\frac{\partial c_{s,i}(x,r,t)}{\partial r}\right), i = p, n \tag{4.17}$$

where $i = p$ represents the positive electrode and $i = n$ represents the negative electrode, r is the radius of the spherical particle, $D_{s,i}$ is the diffusion coefficient in the solid phase. Along the pseudo r-axis lithium-ions can flux through the surface of the particle, therefore the following two boundary conditions apply

$$\begin{aligned} \frac{\partial c_{s,i}(x,r,t)}{\partial r}|_{r=0} &= 0 \\ \frac{\partial c_{s,i}(x,r,t)}{\partial r}|_{r=R_{s,i}} &= -\frac{j_i}{D_{s,i}} \end{aligned} \tag{4.18}$$

where j_i is the molar flux of lithium ions and $R_{s,i}$ is the spherical particle radius.

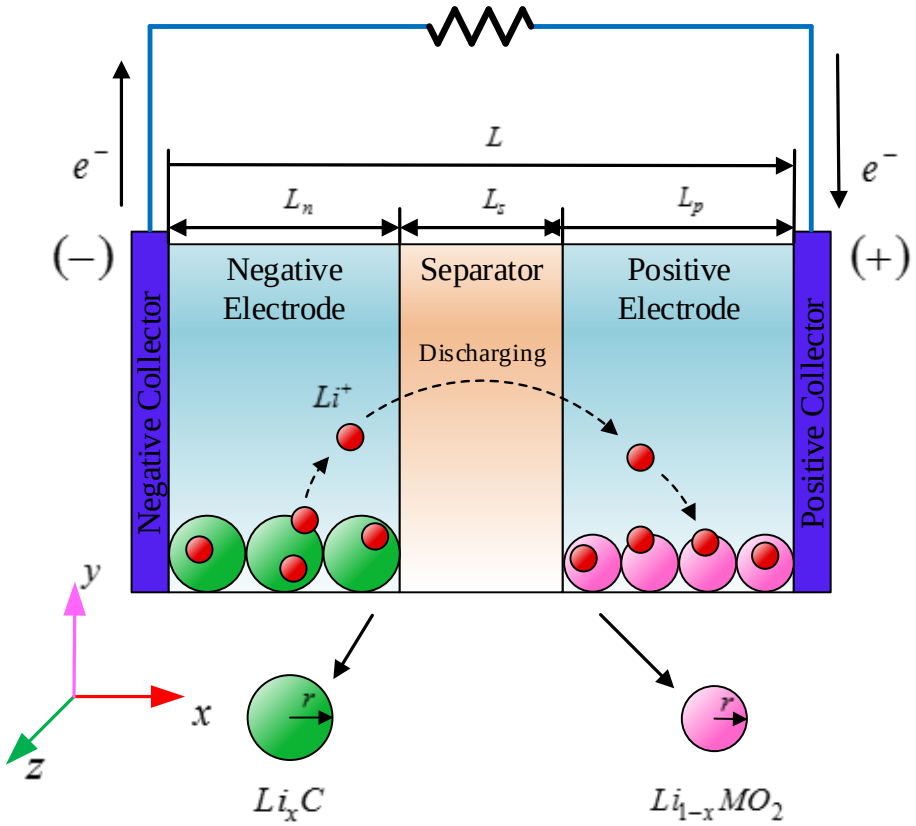

Figure 4.8: Schematic of pseudo-two dimensional model

In the spatially varying electrolyte phase, lithium-ions transport is modeled as 1-D diffusion and transfer from the solid (electrode) phase, this leads to the partial differential equation

$$\varepsilon_i \frac{\partial c_{e,i}(x,t)}{\partial t} = D_{eff,i} \frac{\partial^2 c_{e,i}(x,t)}{\partial x^2} + a_i(1-t_+) j_i(x,t) \quad , i = p,s,n \tag{4.19}$$

The subscript $i = s$ corresponds to the separator. ε_i represents the porosity of the electrolyte phase, $D_{eff,i}$ is the diffusion coefficient in the electrolyte phase, and the

specific area is $a_i = 3/R_{s,i}\varepsilon_{s,i}$. The electrodes consist of solid phase and electrolyte phase, $\varepsilon_{s,i} = 1 - \varepsilon_i$ is the volume fraction of the solid phase (Rahn and Wang, 2013).

The separator prevents electrons from flowing, the pore wall flux j_s is zero in the separator. Lithium-ions cannot flux through the boundary at $x = 0$ and $x = L_p + L_s + L_n$, therefore

$$\frac{\partial c_{e,p}(x,t)}{\partial x}|_{x=0} = \frac{\partial c_{e,n}(x,t)}{\partial x}|_{x=L_p+L_s+L_n} = 0 \tag{4.20}$$

In the solid (electrode) phase conduction of current occurs via electrons where charge conservation and a differential form of Ohm's law is applied to relate the electrical potential and the current density. It has the form

$$\sigma_{eff,i}\frac{\partial^2 \phi_{s,i}(x,t)}{\partial x^2} = a_i F j_i, i = p, n \tag{4.21}$$

The effective conductivity is $\sigma_{eff,i}$. F is Faraday's constant. At $x = 0$ and $x = L_p + L_s + L_n$, there is current flux through electron transfer from current collector to electrode, using Ohm's law this leads to the boundary condition

$$-\sigma_{eff,p}\frac{\partial \phi_{s,p}(x,t)}{\partial x}|_{x=0} = I(t) \tag{4.22}$$

where $I(t)$ is the input current of the battery cell.

At $x = L_p$ and $x = L_p + L_s$, electrons cannot conduct through the separator, this leads to boundary conditions

$$\frac{\partial \phi_{s,p}(x,t)}{\partial x}|_{x=L_p} = \frac{\partial \phi_{s,n}(x,t)}{\partial x}|_{x=L_p+L_s} = 0 \tag{4.23}$$

Considering charge conservation, Ohm's law, concentration theory and diffusive effects leads to the relation

$$k_{eff,i}\frac{\partial^2\phi_{e,i}(x,t)}{\partial x^2} + k^D_{eff,i}\frac{\partial^2 ln(c_{e,i}(x,t))}{\partial x^2} = -a_i F j_i(x,t) \quad , i = p,s,n \tag{4.24}$$

The effective ionic conductivity of the electrolyte $k_{eff,i}$ is a function of the lithium-ion concentration in the electrolyte phase, and $k^D_{eff,i} = 2k_{eff,i}(1-t_+)RT/F$. The electric field at the current-collector/electrolyte boundary and its ion flux are zero therefore

$$\frac{\partial\phi_{e,p}(x,t)}{\partial x}|_{x=0} = \frac{\partial\phi_{e,n}(x,t)}{\partial x}|_{x=L_p+L_s+L_n} = 0 \tag{4.25}$$

At the solid electrolyte interface (SEI), the electrochemical reaction for lithium ion intercalation/deintercalation follows the Butler-Volmer kinetics which relates the flux to concentrations and overpotential

$$\begin{aligned} j_i(x,t) &= 2k_i(c_{s,max,i} - c_{s,i}(x,R_{s,i},t))^{0.5} c_{s,i}(x,R_{s,i},t)^{0.5} \\ &\quad \cdot c_e(x,t)^{0.5}\sinh\left(\tfrac{\alpha F}{RT}\eta_i(x,t)\right), i = p,n \end{aligned} \tag{4.26}$$

where k_i is the reaction rate. This equation is a source of nonlinear resistance such that resistance term depends on the magnitude of the current as shown in Fig. 4.9. Fig. 4.9(a) shows the overpotential curve η_n with respect to the flux j_n, and Fig. 4.9(b) shows the resistance term curve $\frac{\eta_n}{j_n}$ with respect to the flux j_n.

The overpotential η_i is defined as

$$\eta_i(x,t) = \phi_{s,i}(x,t) - \phi_{e,i}(x,t) - U_i(x,t) \tag{4.27}$$

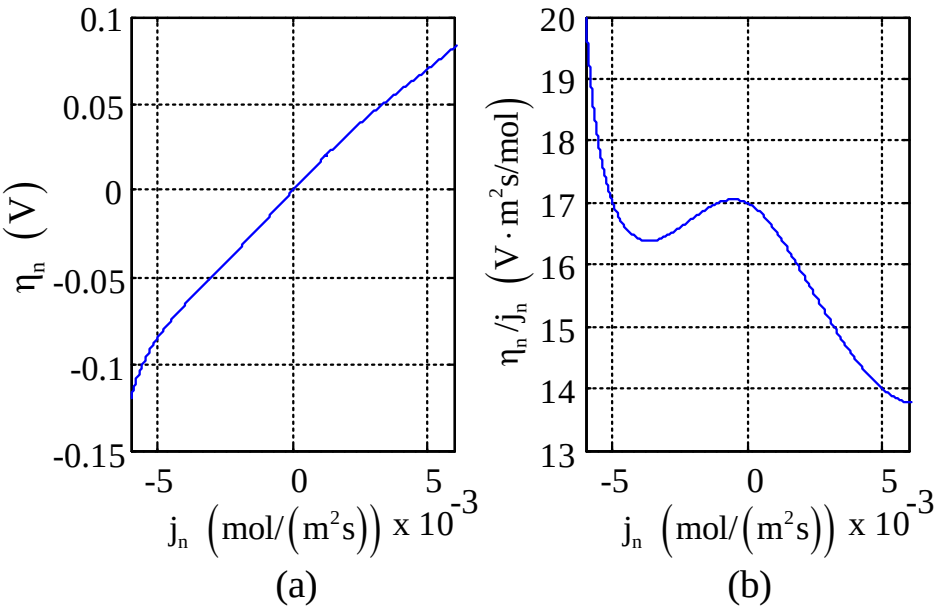

Figure 4.9: Overpotential and resistance curves in the Butler-Volmer kinetics, (a) overpotential, (b) resistance

U_i is the open circuit potential that depends on the lithium ion concentration on the spherical particle surface.

The cell terminal voltage is the voltage drop between the two terminals, therefore, the cell voltage is given by the expression

$$V_{cell}(t) = \phi_{s,p}(L,t) - \phi_{s,n}(0,t) - R_f I(t) \tag{4.28}$$

where R_f represents the contact resistance ohmic losses between the tab, collectors, and the solid phase electrode layer.

In general, the numerical solution of the P2D lithium-ion model is solved by using finite difference method such that all the variables in x-axis and r-axis need to be discretized. This method will generate a huge number of differential algebraic

equations.

4.3.2 Reduced order modeling methods

If this P2D model is used for real time estimation, it is computationally expensive. To reduce and simplify the P2D model, different approaches have been proposed. They can be refereed to as reduced order models than convert the P2D model to a simpler form by using mathematical techniques and model simplifications.

Two/three Differential Algebraic Equations (DAE) for c_s

In (Subramanian *et al.*, 2005), an approximation method for the lithium-ion concentration in the spherical electrode particle was proposed. In this model, the concentration of lithium-ion in solid phase just considers the diffusion process along the r axis and is represented by $c_s(r,t)$. From boundary conditions and the volume averaged technique, unknown coefficients of two-parameter model can be expressed by the average concentration $\bar{c}_s(t)$ and the surface concentration $c_{s,surf}(t)$. Finally, 2 DAEs are derived to obtain the average concentration and the surface concentration

$$\begin{aligned} \frac{d}{dt}\bar{c}_s(t) + 3\frac{j_i}{R_{s,i}} &= 0 \\ \frac{D_{s,i}}{R_{s,i}}\left[c_s(t) - \bar{c}_s(t)\right] &= -\frac{j_i}{5} \end{aligned} \tag{4.29}$$

For the three-parameter model, another parameter the volume-average concentration flux $\bar{q}(t)$ is added. Three DAEs for the three parameters are:

$$\begin{aligned} \frac{d}{dt}\bar{c}_s(t) + 3\frac{j_i}{R_{s,i}} &= 0 \\ \frac{d}{dt}\bar{q}(t) + 30\frac{D_{s,i}}{R_{s,i}^2}\bar{q}(t) + \frac{45}{2}\frac{j_i}{R_{s,i}} &= 0 \\ 35\frac{D_{s,i}}{R_{s,i}}\left[c_s(t) - \bar{c}_s(t)\right] - 8D_{s,i}\bar{q}(t) &= -j_i \end{aligned} \tag{4.30}$$

In the new form, the average concentration and surface concentration in the particle can be solved by 2 or 3 DAEs instead of high order finite difference method for (4.17). In Fig. 4.10, $\bar{c}_s$ and $c_{s,surf}$ from 2 and 3 DAEs are compared with the results of the finite difference method (FDM). The battery is charged and discharged by a series of pulses with increasingly large magnitudes. The figure indicates that average concentrations $\bar{c}_s$ of 2 and 3 DAEs are accurate. However, the surface concentration $c_{s,surf}$ from 2 and 3 DAEs cannot cover FDM's $c_{s,surf}$. It needs to be emphasized that $c_{s,surf}$ is zero when the input j_i is zero in 2 DAEs, therefore 2 DAEs cannot reflect the terminal voltage changing during rest.

Reformulated Model

To reduce order for other states along the x-axis, Subramanian et al. in (Boovaragavan *et al.*, 2008; Subramanian *et al.*, 2007, 2009) developed a reformulated model with volume averaging, Liapunov-Schmidt technique, and perturbation techniques. The pore wall flux j_i, the reciprocal of effective ionic conductivity of electrolyte phase $1/k_{eff,i}$, solid phase average concentration $c_{s,i}^{ave}$, and electrolyte phase concentration

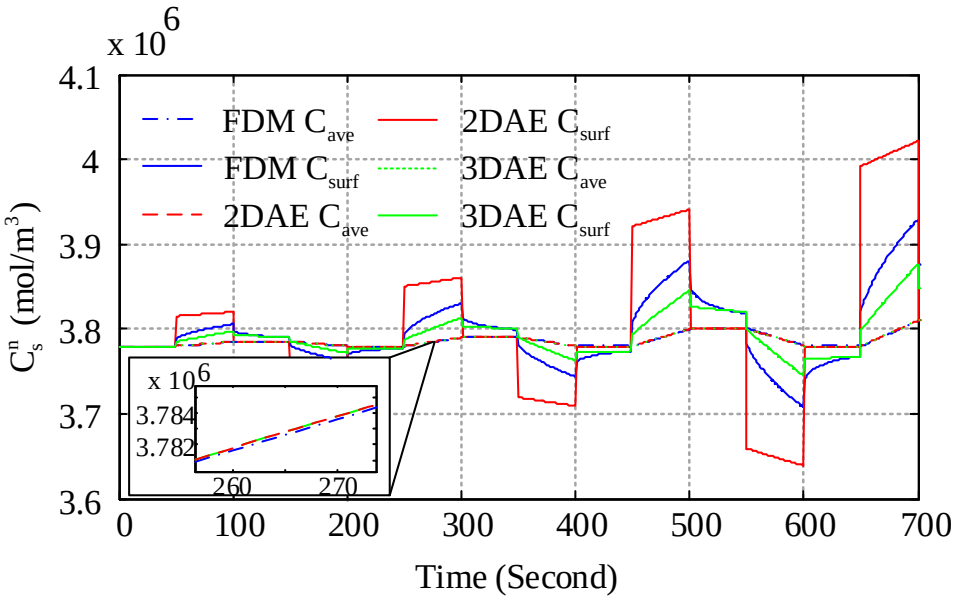

Figure 4.10: Comparison between FDM, 2DAEs, and 3DAEs

$c_{e,i}$ are assumed to take the form

$$y(x,t) = \sum_{i=0}^{N} a_i(t)\xi_i(x) \tag{4.31}$$

where $y(x,t)$ is approximated, $a_i(t)$ represents a time-varying coefficient and $\xi_i(x)$ represent space dependent functions which could be a combination of linear, exponential and oscillatory terms. From j_i and $1/k_{eff,i}$, the solid phase and electrolyte phase potential are derived with an analytical solution of the algebraic equation and presented in polynomial representation. This reformulated model is sufficient for rates up to 1C with 49 DAEs while the full order P2D by finite difference method requires 4800 DAEs. A drawback is the type and order need to be selected based on mathematical intuition, experience and research. Moreover, this method is not valid for short time charge/discharge pulses.

Galerkin's Method

Dao et al. (Dao *et al.*, 2012) used Galerkin's method to approximate partial differential equation for c_e and ϕ_e. In Galerkin's method, the variable in the partial differential equation (PDE) $\frac{d^n y(x,t)}{dx^n} = f(x,t)$ is defined as the sum of the basis function in the form

$$\hat{y}(x,t) = \phi_0 + \sum_{k=1}^{N} c_k(t)\phi_k(x) \tag{4.32}$$

$\phi_k(x)$ are basis functions, and $c_k(t)$ are time-dependent unknown coefficients. In the paper, the sinusoidal function is chosen as a basis function. Substituting $\hat{y}(x,t)$ into the full PDE can get a residual which is defined as

$$R(x,t) = \frac{d^n}{dx^n}\left(\phi_0 + \sum_{k=1}^{n} c_k(t)\phi_k(x)\right) - f(x,t) \approx 0 \tag{4.33}$$

The basis function and residual satisfy the relationship

$$\langle \phi, R \rangle = \int_a^b \phi_k R(x,t)dx = 0 \tag{4.34}$$

This equation can generate a set of N linear ordinary differential equations (ODEs). Time-dependent unknown coefficients $c_k(t)$ can be solved from these ODEs. A drawback of this method is that these unknown coefficients need to be recalculated if parameters and properties change.

Proper Orthogonal Decomposition

Cai and White (Cai and White, 2009) proposed a reduced order model which is approached by proper orthogonal decomposition (POD). In this method, a partial

differential equation needs to be discretized and solved in the discrete model. With a constant input, the solution matrix $\mathbf{Y}_{m\times n}$ can be generated, where m presents spatial node points and n presents time steps. Through POD, a kernel $\mathbf{K}$ can be constructed from $\mathbf{Y}$ by using the singular value decomposition (SVD) method.

$$\mathbf{K} = \frac{1}{n}\mathbf{Y}\mathbf{Y}^T \tag{4.35}$$

By SVD, the proper orthogonal modes Φ_i are calculated and sorted by high-to-low singular values.

$$SVD(\mathbf{K}) = \mathbf{\Phi\Sigma\Phi}^T \tag{4.36}$$

A subspace is composed of first N proper orthogonal modes (POMs). The variable in the rigorous model is presented by the linear combination of the first N POM.

$$C(t) = \mathbf{\Phi}a(t) \tag{4.37}$$

In above equations, $a(t)$ is a reduced variable which is derived by substituting $C(t) = \mathbf{\Phi}a(t)$ into the rigorous model. The ROM is constructed by (4.37). This method increases accuracy at high currents. However, there still are a large set of algebraic equations for the rigorous model.

Control Oriented 1D Model

Smith et al. (Smith *et al.*, 2007, 2008) proposed a control oriented 1D electrochemical model which approaches P2D model by using the residue grouping method. This method derives an impedance model transfer functions of pore wall flux $j(z,t)$, solid-electrolyte potential difference $\phi_{s-e}(z,t)$, overpotential $\eta(z,t)$ and solid phase surface

lithium-ion concentration $c_s(z,t)$. The electrolyte phase concentration c_e was solved by quasi-linearization.

If the full order model transfer functions are $Y(s)/I(s)$, the corresponding reduce order model transfer functions are approximated as

$$\frac{\hat{Y}(s)}{I(s)} = \mathbf{Z}(x) + \sum_{k=1}^{n} \frac{\mathbf{r}_k s}{s - \lambda_k} \tag{4.38}$$

where $\mathbf{Z}(x)$ is a $n \times 1$ steady state vector obtained from the full order model as $\mathbf{Z} = lim_{s\to 0} Y(s)/I(s)$, λ_k is numerically generated eigenvalues, and $\mathbf{r}_k$ is $n \times 1$ residue vectors. Nonlinear optimization is needed to be used to fit parameters λ_k and $\mathbf{r}_k$ based on the frequency response cost function

$$\begin{aligned} J = \sum_{k=1}^{n_\omega} \sum_{i=1}^{n_x} & |Re(\hat{Y}(x_i, j\omega_k) - Y(x_i, j\omega_k))|^2 \\ & + |Im(\hat{Y}(x_i, j\omega_k) - Y(x_i, j\omega_k))|^2 \end{aligned} \tag{4.39}$$

In (4.39), x_i represents the spatial domain $x \in [0, L]$, and $j\omega_k$ presents the frequency domain. This method can match a specific frequency range, leading to better performance at high frequency compared to other approximation methods. However, the nonlinear optimization is not practical, because it is sensitive to the initial condition and cannot ensure the optimal result is globally optimal. If the cell ages, this reduced order model needs to be reconstructed.

Discrete-time Realization Algorithm

James et al. (Leea *et al.*, 2012a,b) extended the model of Smith et al. to derive analytic transfer functions for ϕ_s, ϕ_e, and c_e. However, those transfer functions are

transcendental functions. In order to generate reduced order discrete time state space model, the discrete-time realization algorithm(DRA) is used. First, transfer functions are sampled at high rate and converted to the continuous-time impulse responses through inverse discrete Fourier transform. Second, through cumulative summation of the impulse responses, the continuous-time step responses can be obtained and used to generate discrete-time pulse responses. The discrete-time state space model is derived from Ho-Kalman algorithm that can return discrete-time state-space matrices from discrete-time pulse responses. This reduced order model has high accuracy and short computing time. However, if parameters and properties of cell change, the process to generate discrete-time pulse responses need to be repeated to generate a new reduced order model from a changed transfer function.

The above methods have several limitations in practice, they are based on numerical solution and need to know a priori knowledge of a cell. If the cell ages or external condition changes, some parameters and properties, such as the diffusion coefficient D_s, the reaction rate k_{eff} and even the radius R_s, will change. These reduced order models need to be reconstructed or the full order PDE needs to be solved again. In a battery management system, the reduced order model should have capability to observe internal properties of a cell on-line.

Padé **Approximation**

In this approach a linearized Butler-Volmer equation via quasi-linearization and approximation of spherical diffusion Padé approximations are employed (Forman *et al.*, 2011). The diffusion dynamics are slower than the electrical dynamics, so the equilibrium potentials U_n, U_p, and conductivity of electrolyte k^D_{eff} and k_{eff} are assumed to

be fixed in time. The remaining nonlinear Butler-Volmer equation is quasi-linearized at every integration time step and the algebraic loop is linearized into block matrix form.

For the lithium-ion diffusion process on one spherical particle, the finite difference method needs to calculate N points. Forman et al. just calculated 2 states: $c_s(s)$ and c_s^{ave}. The transfer function between input pore wall flux $J(s)$ and output Li ion concentration $c_s(s)$ are derived. Based on this transfer function, the average lithium-ion concentration is modeled as a pure integrator,

$$\frac{c_s^{ave}}{J} = -\frac{3Dm}{R_s s} \tag{4.40}$$

The transfer function for surface concentration is complex and can be represented as

$$\frac{c_s(s)}{J(s)} = G(s) \tag{4.41}$$

This transfer function $G(s)$ is approximated by a N-order Padé approximation as

$$P(s) = \frac{\sum_{m=0}^{N-1} a_m s^m}{s(1 + \sum_{n=1}^{N-1} b_n s^n)} \tag{4.42}$$

The known transfer function $G(s)$ has a pole at the origin, $G(s)$ and $P(s)$ need to be multiplied by s to cancel this pole when deriving coefficients in $P(s)$. The approximation is interested in low frequency, therefore those coefficients are calculated

by 0 to n-order derivative at $s = 0$ as follows

$$\begin{aligned} sG(s)|_{s=0} &= sP(s)|_{s=0} \\ \frac{d}{ds}\left(sG(s)\right)|_{s=0} &= \frac{d}{ds}\left(sP(s)\right)|_{s=0} \\ \frac{d^2}{ds^2}\left(sG(s)\right)|_{s=0} &= \frac{d^2}{ds^2}\left(sP(s)\right)|_{s=0} \\ &\vdots \end{aligned} \tag{4.43}$$

From above equations, coefficients in (4.42) can be solved. The Padé approximation provides a method to generate a fixed reduced order model that the construct does not change with internal parameters variation. However, this model works well at low frequency, but does not have good performance at high frequency unless the order increases. From the result of this paper, 10th-order Padé approximation can handle 0.4Hz.

SPM and ESPM

To shorten the computational run time, a single particle model is proposed (Guo *et al.*, 2011). In this model, a single spherical particle is modeled instead of several spherical particles in each electrode as shown in Fig.4.11.

The diffusion of lithium ion in the single electrode active material is similar with (4.17), but neglects the position on the primary x-axis. The partial differential equation can be solved by finite difference method or approximated by two/three-parameter model as discussed in (Subramanian *et al.*, 2005). The distribution of lithium ion concentration in the electrolyte phase is assumed to be uniform. The variations of the current density through two electrodes are assumed to follow a uniform distribution. Moreover, the potential in the electrolyte phase is ignored, and

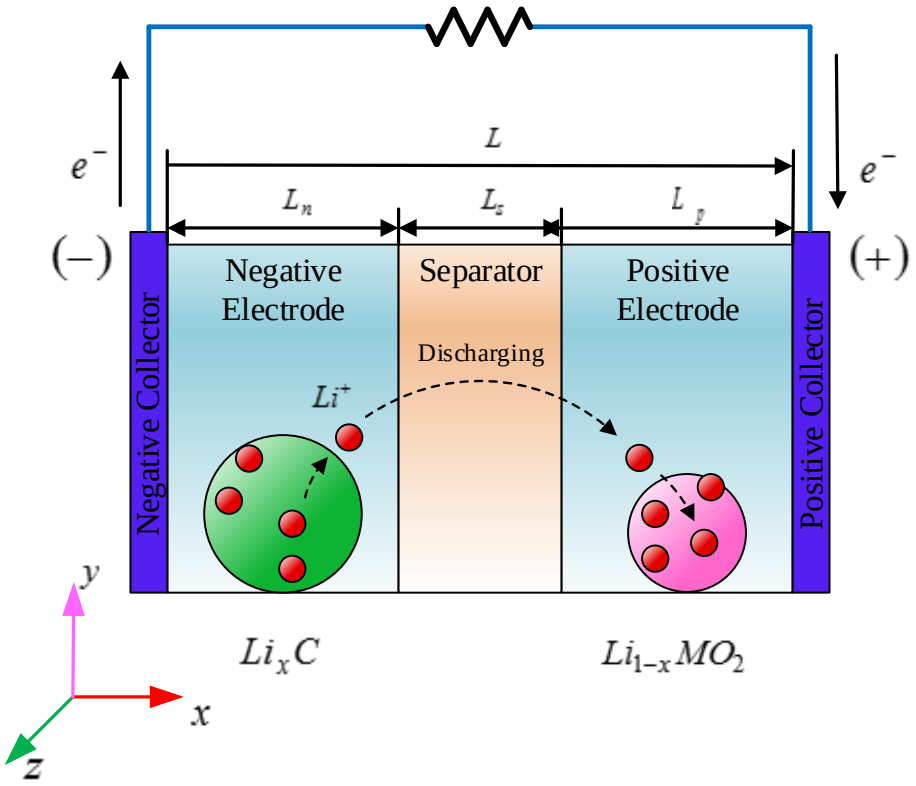

Figure 4.11: Schematic of single particle model

the potential on ohmic loss between two collectors is simplified as $R_f I$. Based on the above assumptions, the terminal voltage can be expressed as

$$\begin{aligned} V_{cell} &= U_p(c_{s,p}|_{r=R_{s,p}}) - U_n(c_{s,n}|_{r=R_{s,n}}) \\ &\quad + \frac{RT}{0.5F} asinh \frac{j_p}{j_{0,p}} - \frac{RT}{0.5F} asinh \frac{j_n}{j_{0,n}} \\ &\quad + R_f I \end{aligned} \tag{4.44}$$

where

$$j_{0,i} = 2k_i(c_{s,max,i} - c_{s,i}|_{r=R_{s,i}})^{0.5} c_{s,i}|^{0.5}_{r=R_{s,i}} c_e^{0.5}$$

The third term and the fourth term are the overpotential terms of both electrodes which are derived from the Butler-Volmer kinetics in (4.26).

In (Ahmed *et al.*, 2014a,b; Domenico *et al.*, 2008, 2010), the difference of the electrolyte potential is modeled using the following equation,

$$\phi_{e,p} - \phi_{e,n} = -\frac{I}{2A}\left(\frac{\delta_p}{k^{eff}} + \frac{2\delta_s}{k^{eff}} + \frac{\delta_n}{k^{eff}}\right) \tag{4.45}$$

In order to increase accuracy of SPM, some papers focus on improving c_e, ϕ_e and ϕ_s. Rahimian et al. (Rahimian *et al.*, 2013) applied the polynomial approximation into SPM to model variation of c_e and ϕ_e. Baba et al. (Baba *et al.*, 2014) proposed an enhanced single particle model (ESPM) that uses parabolic profiles to approximate c_e, ϕ_e and ϕ_s across the primary x-axis. Unlike the P2D model, these three states along x axis do not need to be known at each discrete point. In ESPM, they can be simplified by values at the boundary and average values in three regions. Therefore, coefficients in parabolic profiles are solved from boundary conditions and the volume average technique. Fig. 4.12 compares the performance of SPM (Guo *et al.*, 2011), ESPM (Baba *et al.*, 2014), and P2D models which are solved by FEA in COMSOL. Note that the parameters in the three models are from (Boovaragavan *et al.*, 2008). The input current of these two models change from 0.25C to 2C. This figure indicates that SPM and ESPM can match well the P2D model when the current is less than 1C. For high C-rate application, the accuracy of SPM is not reliable. However, SPM and ESPM simplified model, fitting parameters of them may improve the accuracy

for high C-rate. This chapter will discuss how SPM is employed to model lithium-ion battery in BMS development.

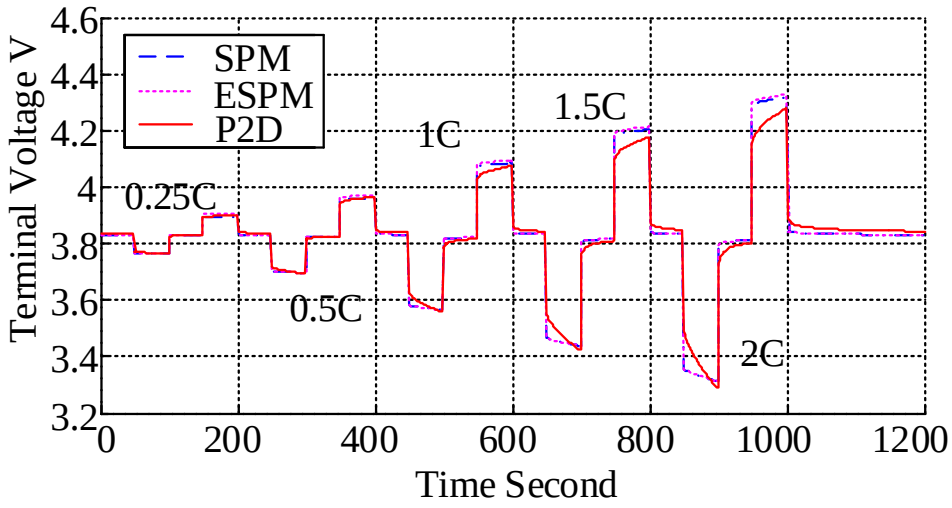

Figure 4.12: Comparison between SPM, ESP, and P2D models at different C-rate

4.3.3 Comparison with equivalent circuit model

Equivalent circuit models are routinely used in BMS design due to their simple structure and relative ease to fit parameters and estimate battery states (Hu *et al.*, 2012; Mohan *et al.*, 2015; Prasad and Rahn, 2012). A typical ECM consists of the ohmic resistor, open circuit voltage, and several resistor-capacitor parallel pairs in series. RC pairs characterize response of terminal voltage with respect to input current and time. More RC pairs can provide higher accuracy. To improve the fidelity of the ECM, component values in the ECM could be designed as variables dependent on SOC and temperature. Furthermore, components are asymmetric to approximate response of battery charge/discharge. To obtain high accuracy at different SOC and temperatures, experiment data at different conditions are needed. Therefore, a large

number of parameters need to be fitted.

The ECM accuracy deteriorates at high currents, low SOC, lower temperatures, and at operating points away from the characterization tests (Chaturvedi *et al.*, 2010; Seaman *et al.*, 2014). At low SOC the battery is extremely nonlinear. Table 4.3 compares the fitting results of SPM with ECM for a 2.9 Ah Panasonic NCR18650A cell. The ECM includes 3RC pairs, nonlinear resistance terms and asymmetric parameters. The fitting method for ECM is quadratic programming based. The ECM has higher mean absolute error (MAE) than SPM, especially when the battery is running under US06 drive cycle which has aggressive regenerative braking and acceleration and the SOC change is 6%. In the US06 drive cycle, the maximum current is 6.077A, more than 2C-rate for the NCR18650A cell. Fig 4.13 shows fitting results and absolute voltage errors of SPM and ECM for US06.

Table 4.3: Fitting results of SPM and ECM for a 2.9Ah NCR18650A cell

	SOC range	Maximum current	SPM MAE	ECM MAE
UDDS	82.07% $\sim$ 77.97%	2.564A	3.811mV	9.7874mV
US06	77.38% $\sim$ 71.37%	6.077A	11.473mV	18.8847mV
HWY	69.87% $\sim$ 63.50%	2.13A	6.216mV	17.9381mV

4.3.4 Lithium-ion battery SEI growth model

From the literature, many aging mechanisms occur that lead to battery degradation. From (Lin *et al.*, 2013; Ning *et al.*, 2006; Ramadass *et al.*, 2004; Safari *et al.*, 2009), main aging mechanisms are SEI formation at first few cycles and SEI growth during cycling at the anode. SEI formation and growth either increases resistance or transplants active lithium into SEI growth and leads to corrosion of lithium in the active

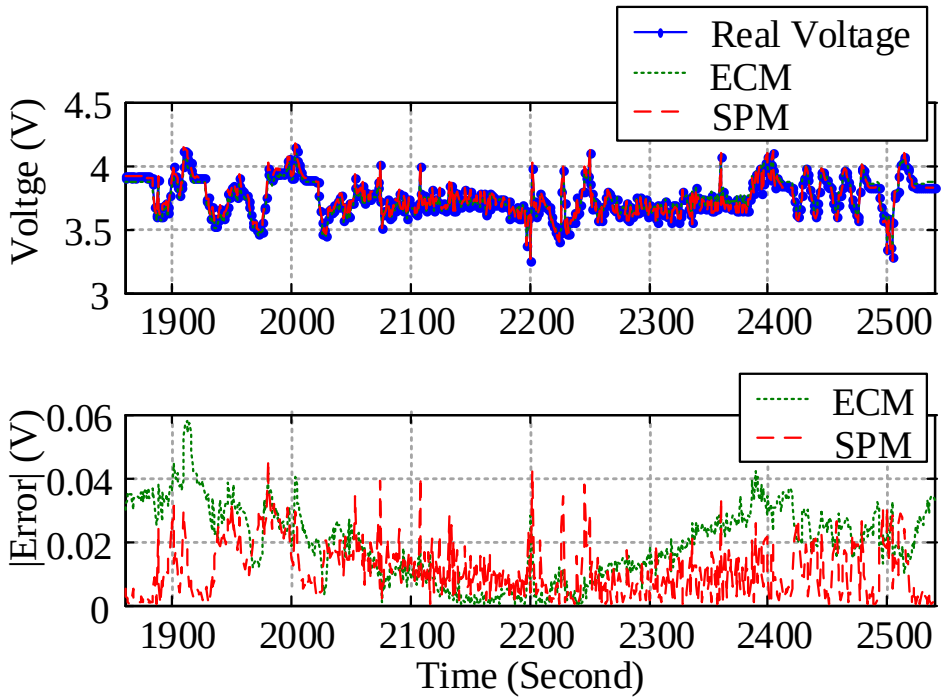

Figure 4.13: Comparison fitting results between SPM and ECM under US06 drive cycle

carbon.

During charging, the intercalation occurs between lithium ions and electrons at the anode.

$$C + xLi^+ + xe^- \longrightarrow Li_xC \tag{4.46}$$

Unstable solvent also reacts with lithium ions and electrons, and forms a layer on the surface of the solid spherical particle as shown in Fig. 4.14.

$$Solvent + xLi^+ + xe^- \longrightarrow P \tag{4.47}$$

P presents the new SEI layer. Therefore, the pore wall flux of lithium ions is the sum

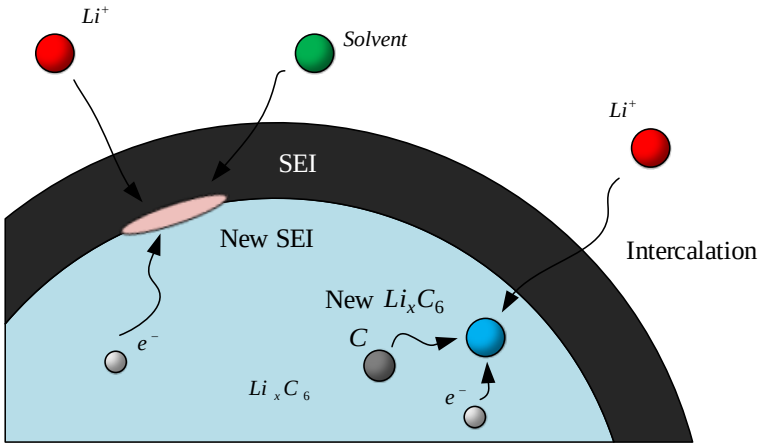

Figure 4.14: SEI format on the anode electrode

of intercalation and side reaction flux (Ramadass *et al.*, 2004)

$$j_n = j_{int} + j_{side} \tag{4.48}$$

The intercalation flux for the SPM is given by the Butler-Volmer kinetics

$$\begin{aligned} j_{int} &= 2k_n(c_{s,max,n} - c_{s,n}|_{r=R_{s,n}})^{0.5} c_{s,n}|^{0.5}_{r=R_{s,n}} \\ & \quad c_e^{0.5} \sinh\left(\tfrac{\alpha F}{RT}\eta_n\right) \end{aligned} \tag{4.49}$$

The kinetic expression for the side reaction is also derived from the Butler-Volmer equation (Ramadass *et al.*, 2004; Safari *et al.*, 2009)

$$j_{side} = -k_{f,s} exp\left(-\frac{\beta F}{RT}\left(\phi_{s,n} - R_{SEI} F j_n\right)\right) \tag{4.50}$$

where $k_{f,s}$ is the rate constant of the side reaction. The SEI growth is related to the side reaction flux through

$$\frac{d\delta}{dt} = -\frac{j_{side}}{2}\frac{M_{SEI}}{\rho_{SEI}} \tag{4.51}$$

The molecular weight of SEI is M_{SEI}, and the SEI density is ρ_{SEI}. The SEI film resistance is $R_{SEI}(t) = \delta(t)/\kappa_{SEI}$, κ_{SEI} is SEI ionic conductivity. With the SEI layer thicker, impedance rises and relates to power fade. Capacity also reduces during SEI growth, due to lithium ions gradually being lost to form the SEI layer in this irreversible process. Moreover, the open circuit voltage curve would shift due to the loss of lithium ions (Di Domenico *et al.*, 2015; Ning *et al.*, 2006).

4.4 Single Particle Model for BMS Development

As a battery model in BMS, SPM should provide accurate SOC, internal impedance, and capacity through on-line estimation. This section summarizes how SOC and capacity that can be reflected in the SPM. The structure and discretization method are introduced in detail. In order to build an accurate SPM and identify parameters of this model, a new parametrization method for SPM is proposed. The SPM is combined with the SEI layer growth model and compared with experimental results. Other contributions are that SOC and SOH estimation methods are proposed based on EKF.

4.4.1 Cell level quantities

Open circuit voltage is related to open circuit potentials of the two electrodes

$$V_{OCV} = U_p(c_{s,p}|_{r=R_{s,p}}) - U_n(c_{s,n}|_{r=R_{s,n}}) \tag{4.52}$$

To develop the relationship between c_s and SOC, the lithium-ion concentration c_s^m could be presented by a ratio as state of charge in each electrode $SOC_i^m = c_{s,i}^m/c_{s,i,max}$.

The two curves of open circuit potentials are shown in Fig. 4.15. The x-axis is SOC_i^{surf}. The OCV curve of the negative electrode is published in (Boovaragavan *et al.*, 2008), the curve of the positive electrode could be derived from Hybrid Pulse Power Characterization test. Note that the positive electrode OCV is not directly given by HPPC test. A net OCV is given by HPPC and is utilized to subtract the negative OCV to get the positive OCV.

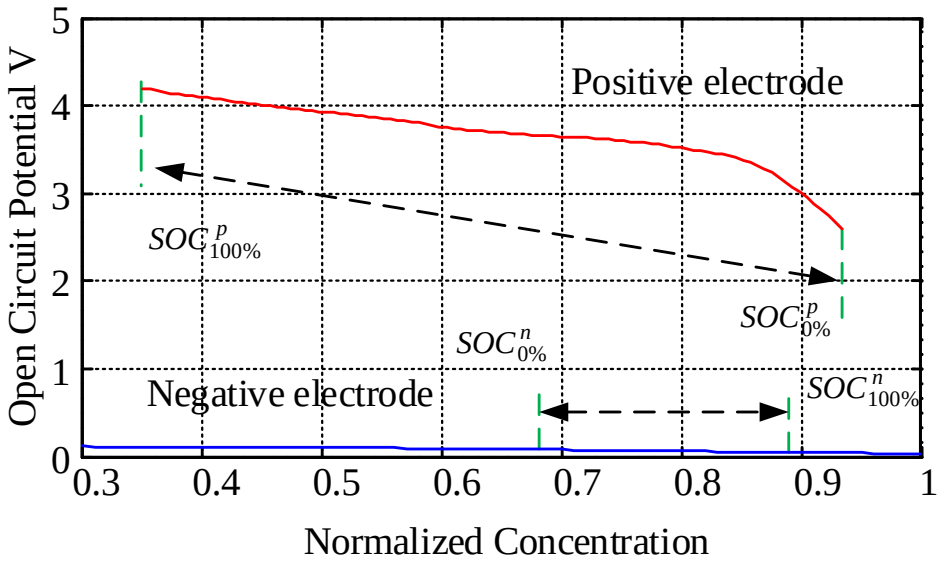

Figure 4.15: Electrode open circuit potential curves

The capacity of the cell is related to the total number of active lithium-ions of each electrode. In practice, to avoid rapid cell degradation and power depletion, the cell cannot use all lithium-ions in the electrodes, therefore the useful capacity of each electrode is a window between SOC_{100}^i and SOC_0^i. During discharge, lithium ions move from negative electrode to positive electrode, thus the concentration of lithium ions decrease from $SOC_{100\%}^n$ to $SOC_{0\%}^n$ in the negative electrode and increases from

$SOC^p_{100\%}$ to $SOC^p_{0\%}$ in the positive electrode. During charging, lithium ions move in the opposite direction. Total number of active lithium-ions are defined as ampere-hour capacity of two electrodes that can be expressed as

$$\begin{aligned} Q_n &= AFL_n\varepsilon_s^n c_{s,max}^n |SOC^n_{100\%} - SOC^n_{0\%}|/3600Ah \\ Q_p &= AFL_p\varepsilon_s^p c_{s,max}^p |SOC^p_{100\%} - SOC^p_{0\%}|/3600Ah \end{aligned} \tag{4.53}$$

A is the electrode plate area, L_n, L_s and L_p are length of the three cell dimension layers, ε_s is the solid phase volume fraction, and $c_{s,max}$ is the total capacity of electrode in moles of lithium per unit volume. Overall, the cell capacity is the minimum of the two electrode capacities. For a fresh battery, these two electrode capacities are assumed as equal.

The molar flux of lithium ions j_i is

$$j_i = \frac{I}{a_i F A L_i} \tag{4.54}$$

The state of charge of each electrode is related to the average concentration of lithium-ion of each electrode. To calculate lithium-ions concentration in both electrodes, a spherical particle can be discretized to several shells and calculated by FDM. The average concentration in a spherical particle is

$$\bar{c}_s[k] = \frac{1}{V}\left[dV_1 c_s^0[k] + dV_2 c_s^1[k] + \ldots + dV_M c_s^{M-1}[k]\right] \tag{4.55}$$

where the m^{th} shell's volume $dV_m = \frac{4}{3}\pi(m\Delta r)^3 - \frac{4}{3}\pi((m-1)\Delta r)^3$ and the spherical volume $V = \frac{4}{3}\pi(M\Delta r)^3$. The state of charge of each electrode are $\overline{SOC^i} = \bar{c_s^i}/c^i_{s,max}$.

The state of charge is

$$SOC = \frac{SOC^p_{0\%} - \overline{SOC^p}}{SOC^p_{0\%} - SOC^p_{100\%}} = \frac{\overline{SOC^n} - SOC^n_{0\%}}{SOC^n_{100\%} - SOC^n_{0\%}} \tag{4.56}$$

4.4.2 Finite difference method for the diffusion equation

As mentioned in Section 4.3, the diffusion equation (4.17) can be solved by FDM for high accuracy. In (Ahmed *et al.*, 2014a; Domenico *et al.*, 2008, 2010), the spherical particle is separated by even shells. Lee et al. (Lee *et al.*, 2011) separates the spherical particle by uneven shells in order to reduce the number of states. In order to observe how c_s changes from the surface to center of the spherical particle, even shells are utilized to separate the spherical particle in this thesis. If the spherical particle is separated by M shells, as shown in Fig. 4.16, lithium-ion concentration on each shell c_s^m, where $m = 1 \dots M-1$ could be calculated by FDM. The number of shells in a spherical particle will be discussed later.

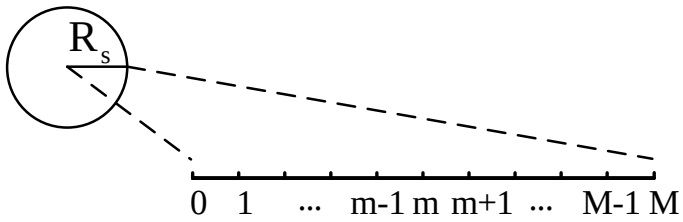

Figure 4.16: A spherical particle is divided into M shells

For the m^{th} shell, the central difference for the diffusion equation is given by

$$\frac{c_s^m[k+1]-c_s^m[k]}{\Delta t} = \frac{D_s}{(\Delta r)^2}\left(\frac{m-1}{m}c_s^{m-1}[k] - 2c_s^m[k] + \frac{m+1}{m}c_s^{m+1}[k]\right) \tag{4.57}$$

Boundary conditions (4.18) can provide the following relationship by forward and backward difference methods.

$$\begin{aligned} c_s^0[k] &= c_s^1[k] \\ c_s^M[k] &= c_s^{M-1}[k] - \frac{\Delta r j}{D_s} \end{aligned} \tag{4.58}$$

Thus, for the 1^{st} and $M-1^{th}$ shells, the difference equations are given by

$$\begin{aligned} \frac{c_s^m[k+1]-c_s^m[k]}{\Delta t} &= \frac{D_s}{(\Delta r)^2}\left(-2c_s^1[k]+2c_s^2[k]\right) \\ \frac{c_s^m[k+1]-c_s^m[k]}{\Delta t} &= \frac{D_s}{(\Delta r)^2}\left(c_s^{M-2}[k]\frac{M-2}{M-1}+c_s^{M-1}[k]\frac{-M+2}{M-1}\right) \\ &\quad +\frac{-j}{\Delta r}\frac{M}{M-1} \end{aligned} \tag{4.59}$$

Diffusion equation for one spherical particle can be expressed as

$$\begin{bmatrix} c_s^1[k+1] \\ \vdots \\ c_s^{M-1}[k+1] \end{bmatrix} = \mathbf{A}\begin{bmatrix} c_s^1[k] \\ \vdots \\ c_s^{M-1}[k] \end{bmatrix} + \mathbf{B}j \tag{4.60}$$

where

$$\mathbf{A} = \frac{D_s \Delta t}{(\Delta r)^2} \begin{bmatrix} -2 & 2 & & & \\ & \ddots & & & \\ & \frac{m-1}{m} & -2 & \frac{m+1}{m} & \\ & & & \ddots & \\ & & & \frac{M-2}{M-1} & \frac{-M+2}{M-1} \end{bmatrix} + I$$

$$\mathbf{B} = -\frac{\Delta t}{\Delta r} \begin{bmatrix} 0 \\ \vdots \\ 0 \\ \frac{M}{M-1} \end{bmatrix}$$

To derive the open circuit potential and SOC of each terminal, outputs of a spherical particle are lithium-ion concentration on the spherical surface $c_{s,surf}$ and average lithium-ion concentration $\bar{c}_s$. From the boundary condition of the spherical surface, the lithium-ion concentration on the spherical surface are

$$c_s^{surf}[k] = c_s^M[k] = c_s^{M-1}[k] - \frac{\Delta r j}{D_s} \tag{4.61}$$

The average concentration is calculated by (4.55). Output equations are

$$\begin{bmatrix} c_s^{surf}[k] \\ \bar{c}_s[k] \end{bmatrix} = \mathbf{C} \begin{bmatrix} c_s^1[k] \\ \vdots \\ c_s^{M-1}[k] \end{bmatrix} + \mathbf{D} j \tag{4.62}$$

where

$$\mathbf{C} = \begin{bmatrix} 0 & \cdots & 0 & 1 \\ \frac{dV_1+dV_2}{V} & \frac{dV_3}{V} & \cdots & \frac{dV_M}{V} \end{bmatrix}$$

$$\mathbf{D} = \begin{bmatrix} \frac{-\Delta r}{D_s} \\ 0 \end{bmatrix}$$

Overall, equations in SPM and SEI layer growth model are summarized in Fig. 4.17.

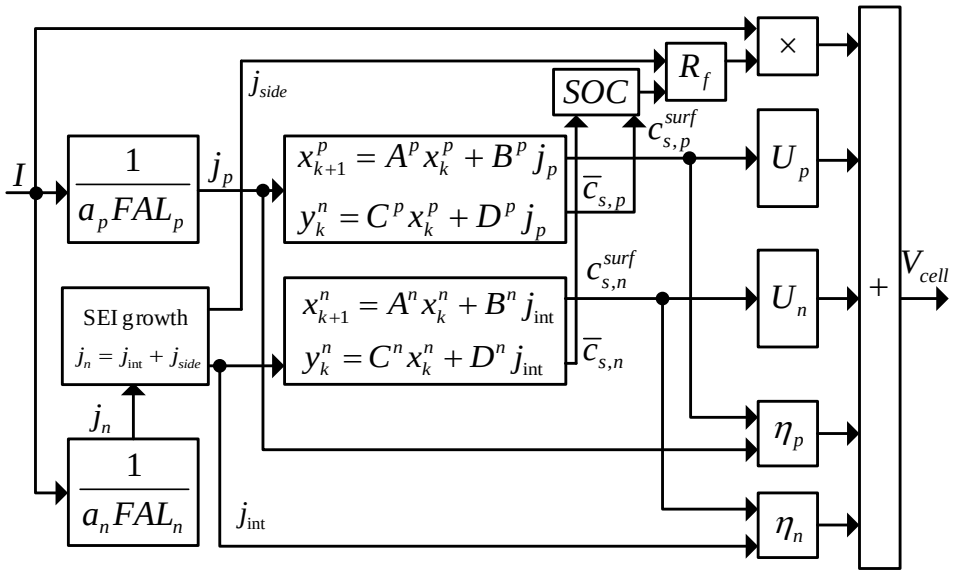

Figure 4.17: Summarized equations in SPM

4.4.3 Experimental procedure

Panasonic NCR18650A cell is tested, aged, and modeled based on SPM. The experimental procedure is summarized in Fig. 4.18. Panasonic NCR18650A is discharged by repeating UDDS, US06, and HWY from a fully charged state to the lower voltage limit of 2.5V. After the drive cycles, the cell is charged by a constant current constant

voltage (CCCV) method, that constant current is 1.5A, constant voltage is 4.2V, and cutoff current is 0.1A. To measure cell's nominal capacity, the cell is discharged by a 3A (1C-rate is 2.9A (Panasonic, 2012)) constant current (CC) and stop when the terminal voltage reaches the cutoff voltage 2.5V. To age the cell, this procedure repeats 50 times until the cycle number reaches 100. Fig. 4.19 shows the experimental testbed. NCR18650A cell's input current is controlled by a bidirectional DC-DC converter from a 12V VRLA battery. The function of the bidirectional DC-DC converter is to generate the driving cycle input current profiles. In this circuit, the 12V VRLA battery is used as a bidirectional power supply device. The computer controls the DC-DC converter and records the input current and terminal voltage.

Fig. 4.20 shows the PCB board of the bidirectional DC-DC converter. There are three half-bridge DC-DC converters on the PCB board. The 1^{st} bridge generates the driving cycle profiles from the VRLA battery. When the tested lithium-ion battery is discharging, the VRLA battery is charging. To protect the VRLA from overcharge, the 2^{nd} bridge is connected to the resistors in Fig. 4.19. The 3^{rd} bridge is not used in this experiment.

4.4.4 Parametrization

In the SPM, there are two open circuit potential curves and approximately 20 parameters that need to be fitted. The difference of two open circuit potentials of two electrodes can be seen as the open circuit voltage in the equivalent circuit model.

$$U_{OCV} = U_p(c_{s,p}|_{r=R_{s,p}}) - U_n(c_{s,n}|_{r=R_{s,n}}) \tag{4.63}$$

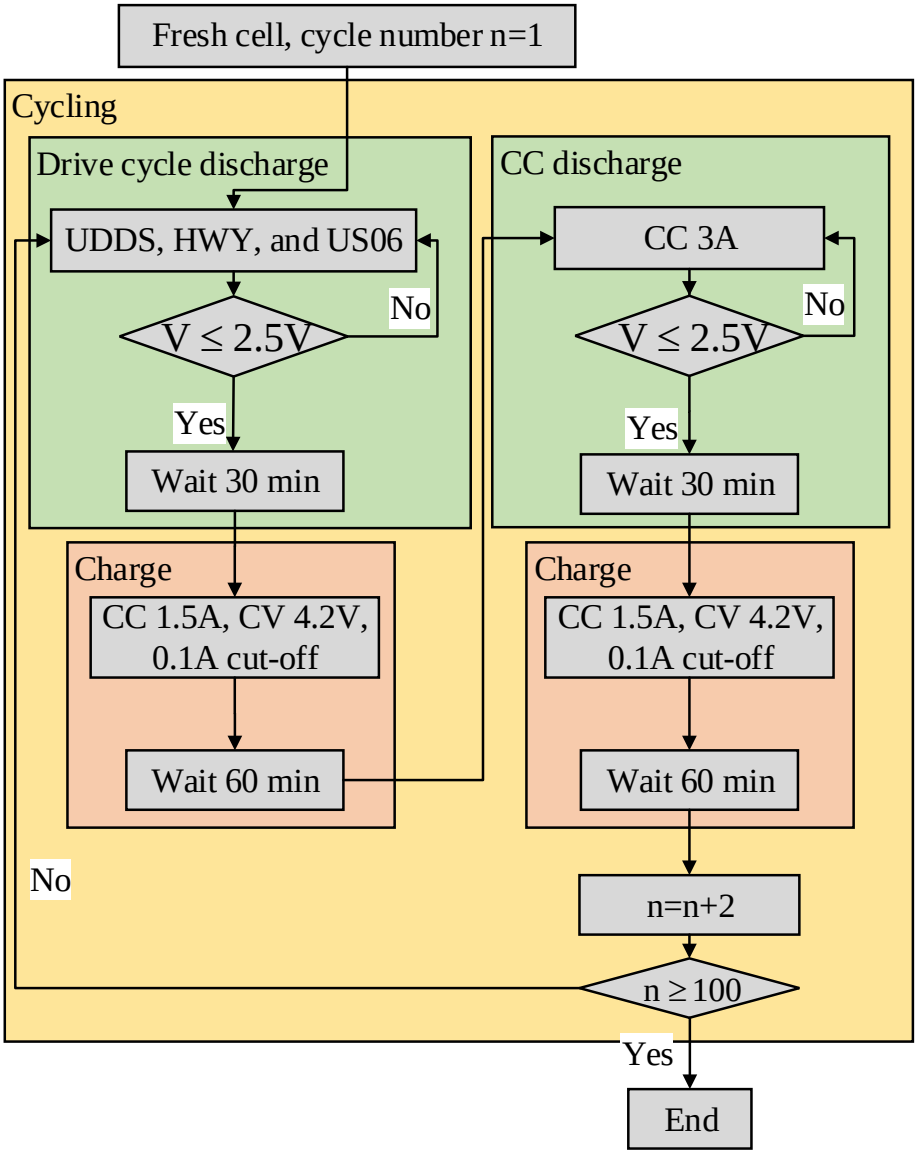

Figure 4.18: Experimental procedure

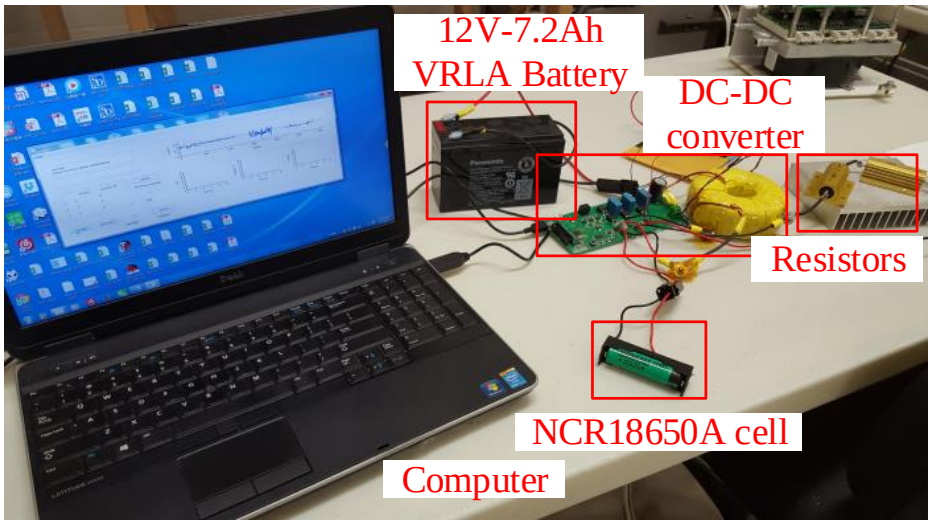

Figure 4.19: Experimental testbed

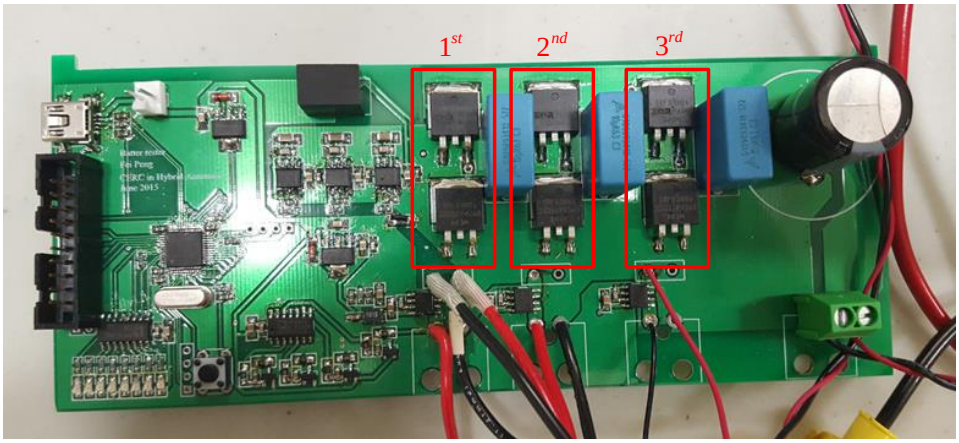

Figure 4.20: PCB of the bidirectional DC-DC converter

The open circuit potential curve on the graphite anode were curve-fitted in (Subramanian *et al.*, 2009). The positive electrode curve can be derived from $U_n(c_{s,n}|_{r=R_{s,n}})$ and U_{OCV}. Two open circuit potential curves used in this thesis are shown in Fig. 4.15.

Some parameters can be derived or assumed. Length of three layers L_n, L_s and L_p and the electrode plate area can be approximated based on cell geometry. The cell capacity can constrain some parameters. For a fresh battery, these two electrode capacities are assumed as equal. Therefore, parameters in (4.53) can be calculated or assumed.

The remaining parameters are diffusion coefficients in the two electrodes $D_{s,i}$, radius of two single particles $R_{s,i}$, reaction rates of two electrodes k_i, and ohmic resistance R_f. The potential in the negative electrode is low and flat, so parameters in the negative electrodes are assumed as constants in this thesis. Parameters in the positive electrode and ohmic resistance can be fitted by numerical optimization. The fitted SPM is compared with UDDS, US06, and HWY experiment result for Panasonic NCR18650A in Fig. 4.21. MAE of fitting is 6.216mV. Parameters are presented in Table. 4.4. Note that R_f is assumed as a function of SOC. Test range of the cell in Fig. 4.21 is from $90\% \sim 60\%$ SOC, R_f is also presented in this table.

4.4.5 Number of shells selection

To model the lithium-ion cell by SPM, the number of shells in each particle needs to be decided. Even though more shells can provide more accurate and smoother lithium-ion concentration curves, high order finite difference equations are computationally expensive and result in complex state estimation. SPMs with different shell numbers (from 5 to 30 shells) in a spherical particle are parametrized and compared. Fig. 4.22

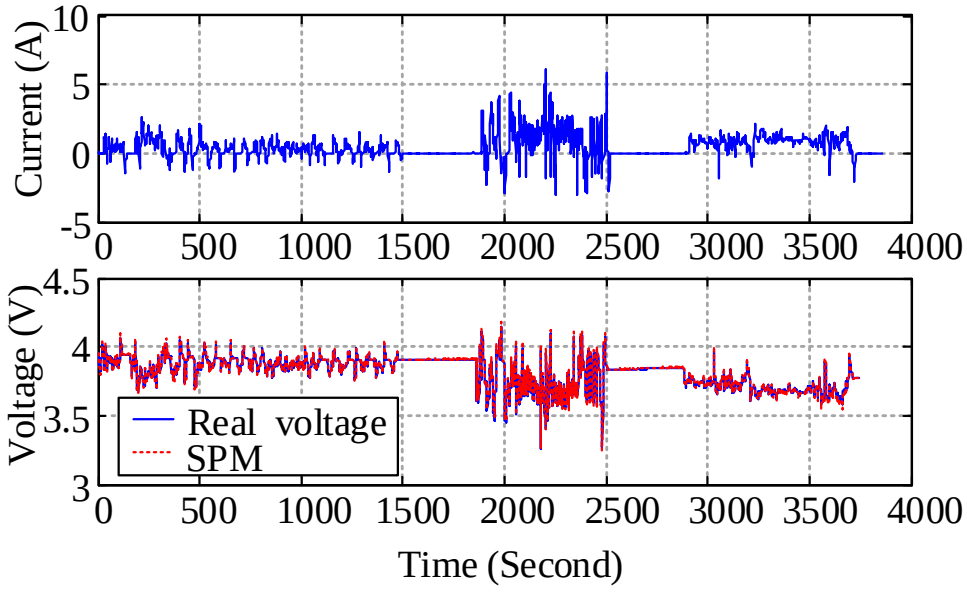

Figure 4.21: Comparison of SPM and UDDS, US06, and HWY drive cycle for Panasonic NCR18650A

Table 4.4: Parameters for SPM

Parameter	Positive electrode	Negative electrode	Source
$c_{s,max,i}$ (mol/m^3)	1.4728×10^5	1.9026×10^5	calculated
SOC_i^0	0.35	0.6376	assumed
SOC_i^{100}	0.934	0.9972	assumed
$D_{s,i}$ (m^2/s)	1.1×10^{-14}	1×10^{-13}	fitted & assumed
$R_{s,i}$ (m)	1.18×10^{-5}	2.3×10^{-5}	fitted & assumed
$k_{n,i}$ (m/s)	6.49×10^{-11}	2.51×10^{-11}	fitted & assumed
$\epsilon_{s,i}$	0.49	0.56	(Boovaragavan *et al.*, 2008)
$L_i(m)$	80×10^{-6}	88×10^{-6}	(Boovaragavan *et al.*, 2008)
$A(m^2)$	0.0342	0.0342	(Muenzel *et al.*, 2015)

SOC	90% ~ 80%	80% ~ 70%	70% ~ 60%	Source
$R_f(\Omega)$	0.057	0.0587	0.0504	fitted

(a) and (c) shows the lithium-ion concentration on each shell in the positive spherical particle with 5 and 20 shells under an 1000 seconds drive cycle. The lithium-ion concentration c_s^p on each shell at the 1000 second mark are shown in Fig. 4.22 (b) and (d). It needs to be emphasized that the color scale of these four figures are same. Fig. 4.22 indicates that the result of (4.60) is influenced by the number of shells.

Mean absolute errors of all cases are presented in Fig. 4.23. Overall, a spherical particle with less shells has higher error than a particle with more shells, especially the particle with less than 10 shells has MAE over 10mV. However, it does not mean that more shells in a particle can provide higher accuracy. If a spherical particle has one more shell, SPM will increase 2 DAEs. Fig. 4.23 indicates that if the shell number is more than 25 (more than 50 DAEs), difficulties arise when trying to find the global minimum point by the parametrization method, due to the high order system. To keep high accuracy and have low DAE numbers, a spherical particle with 20 shells is used in this thesis.

4.4.6 SEI layer growth model

The SEI layer growth model is integrated with the SPM and summarized in Fig. 4.17 (Lin *et al.*, 2013; Ramadass *et al.*, 2004; Safari *et al.*, 2009). This model is compared with experimental results. From constant current discharge in Fig. 4.18, the cycle life characteristics are shown in Fig. 4.24. The capacity of the cell reduces from 2.9Ah to 2.67Ah after 100 cycles. NCR18650A data sheet(Panasonic, 2012) shows that NCR18650A cell's capacity reduces to 2.7Ah after 100 CCCV charge and CC discharge cycles. Parameters of the aging model are adjusted by trial and error and shown in Table. 4.5.

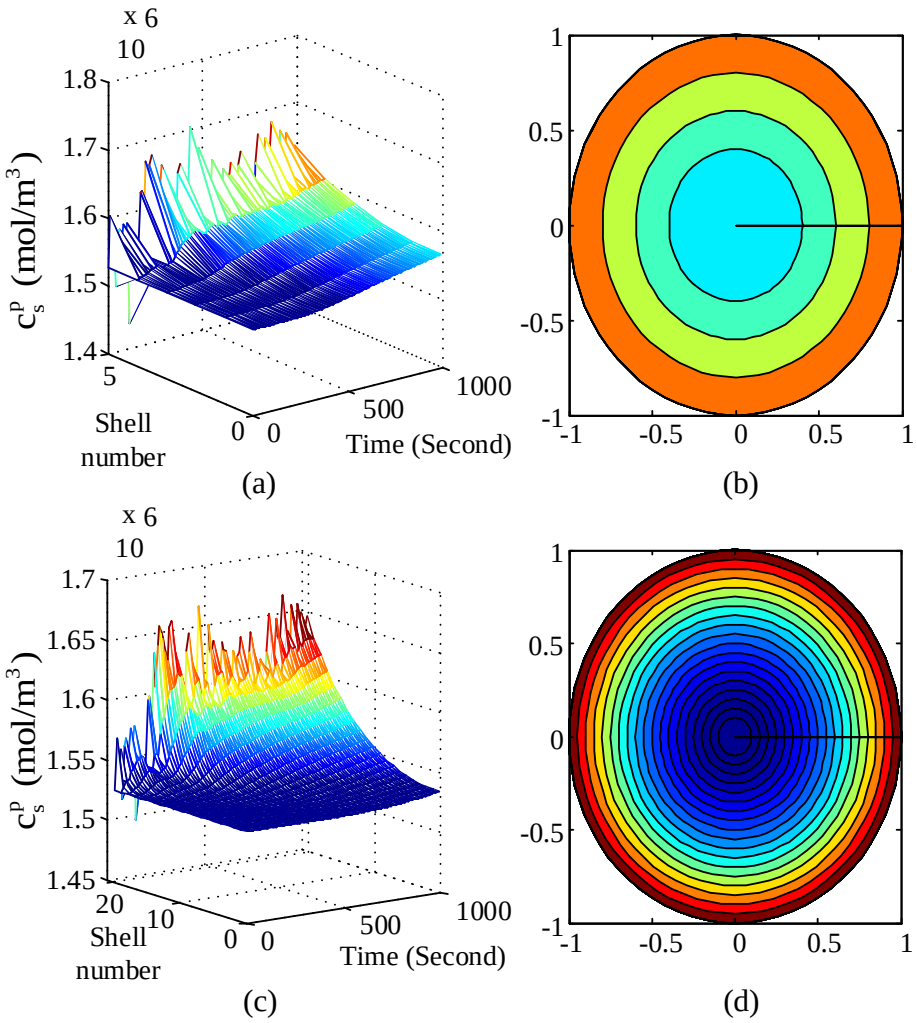

Figure 4.22: Lithium-ion concentration on each shell in a spherical particle with different shell number (a) 5 shells c_s^p under an 1000 seconds drive cycle, (b) c_s^p of 5 shells at the 1000 second mark, (c) 20 shells c_s^p under an 1000 seconds drive cycle, (d) c_s^p of 20 shells at the 1000 second mark

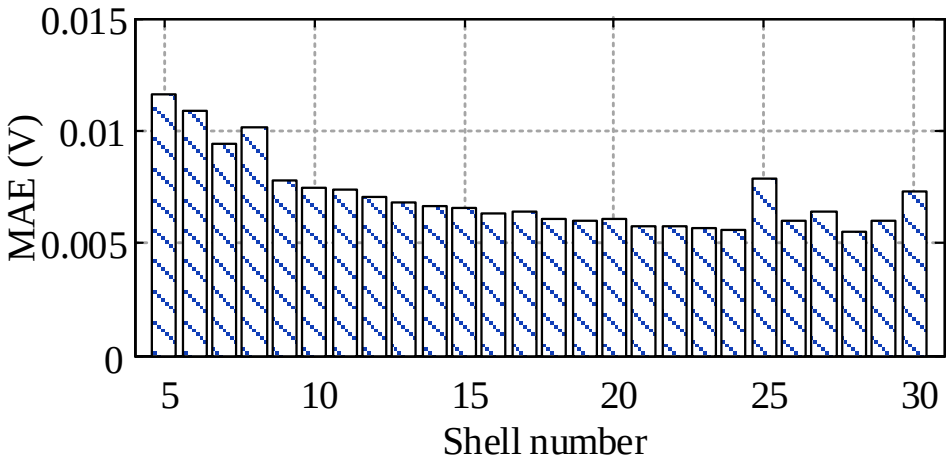

Figure 4.23: Mean absolute error of SPM with different shells number

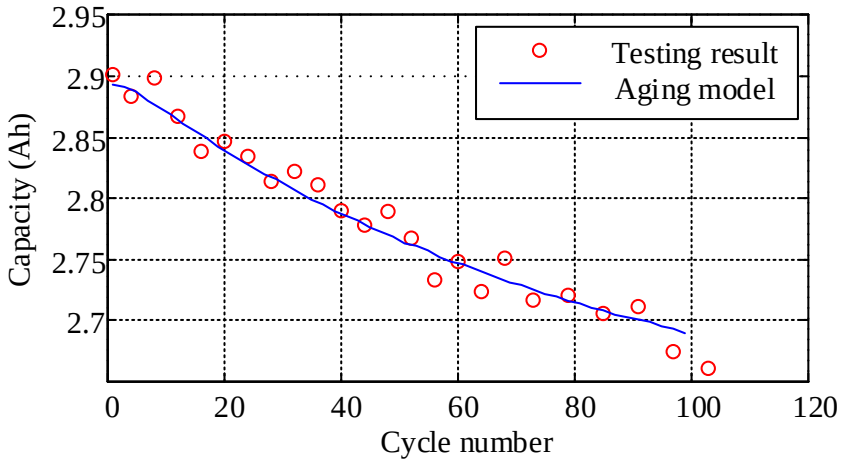

Figure 4.24: Cycle life characteristics

Table 4.5: Parameters for SEI layer growth model

$k_{f,s}(m/s)$	$M_{SEI}(kg/mol)$	$\rho_{SEI}(kg/m^3)$	$\kappa_{SEI}(S/m)$
2×10^{-8}	0.0112	8500	19.8×10^{-3}

4.4.7 SOC and SOH estimation based on HSPM

An energy storage system in an electric vehicle needs to estimate state of charge and state of health. In this chapter, the nonlinear model SPM is estimated by extended Kalman filter. Extended Kalmen filter can be summarized as (Emadi, 2014)

Table 4.6: EKF algorithm

Time update:
$\hat{x}_{k+1}^- = A\hat{x}_k + Bu_k$ $P_{k+1}^- = AP_kA^T + WQ_kW^T$
Measurement update:
$K_{k+1} = P_{k+1}^- H_{k+1}^T (H_{k+1} P_{k+1}^- H_{k+1}^T + VR_{k+1}V^T)^{-1}$ $\hat{x}_{k+1} = \hat{x}_{k+1}^- + K_{k+1}(y - h(x_{k+1}^-, uk+1))$ $P_{k+1} = (I - K_{k+1}H_{k+1})P_{k+1}^-$

SOC estimation

State of charge of a lithium-ion battery could be estimated based on lithium-ion concentrations of $M-1$ shells in spherical particles. To simplify the estimation system, the input current density j in (4.60) is transferred to the input current I by (4.54). The state vector consists of

$$\mathbf{x} = [SOC^1, \ldots, SOC^{M-1}]^T \tag{4.64}$$

which normalize the lithium-ion concentration on each shell $[c_s^1, \ldots, c_s^{M-1}]$ by $c_{s,max}$. Therefore, matrices **A**, **B**, **C**, and **D** in (4.60) and (4.62) are modified to

$$\begin{aligned} \mathbf{A_d} &= \mathbf{A}, \quad \mathbf{B_d} = \frac{\mathbf{B}}{a^i F L_i A \cdot c_{s,max}} \\ \mathbf{C_d} &= \mathbf{C}, \quad \mathbf{D_d} = \frac{\mathbf{D}}{a^i F L_i A \cdot c_{s,max}} \end{aligned} \tag{4.65}$$

The measurement equation is a nonlinear equation (4.44) which includes the open circuit potentials of both electrodes $U_p(SOC_p^{surf})$ and $U_n(SOC_n^{surf})$, therefore, the state vector needs state of charge of the lithium-ion concentration on the surface of each electrode SOC_i^{surf} through (4.62). However, a state vector of a system includes two electrodes, lithium-ion concentrations of each shell leads to a system with weak observability. This dynamic system is of the form

$$\begin{aligned} \begin{bmatrix} \mathbf{x}_{k+1}^p \\ \mathbf{x}_{k+1}^n \end{bmatrix} &= \begin{bmatrix} \mathbf{A_d}^p & 0 \\ 0 & \mathbf{A_d}^n \end{bmatrix} \begin{bmatrix} \mathbf{x}_k^p \\ \mathbf{x}_k^n \end{bmatrix} + \begin{bmatrix} \mathbf{B_d}^p \\ \mathbf{B_d}^n \end{bmatrix} I_k \\ V_{cell,k} &= h([\mathbf{x}_k^p, \mathbf{x}_k^n]^T, I_k) \end{aligned} \tag{4.66}$$

where the Jacobian matrix of partial derivatives of h with respect to $[\mathbf{x}_k^p, \mathbf{x}_k^n]^T$ is

$$\mathbf{H} = [\underbrace{0, \ldots, 0}_{M-2}, \frac{\partial h}{\partial SOC_p^{M-1}}, \underbrace{0, \ldots, 0}_{M-2}, \frac{\partial h}{\partial SOC_n^{M-1}}] \tag{4.67}$$

There is no equation that relates the positive electrode and the negative electrode together. The rank of the observability matrix of the system is less than $2(M-1)$, so this system has weak observability. According to (Domenico *et al.*, 2010), the state vector in this system just includes the positive electrode $\mathbf{x} = [SOC_p^1, \ldots, SOC_p^{M-1}]^T$

to reduce orders of the model and develop a model with a full rank observability matrix.

To calculate the terminal voltage from the measurement equation (4.62), SOC_n^{surf} of term $U_n(SOC_n^{surf})$ in the measurement equation needs to be derived by the state vector $\mathbf{x}$. Through (4.56) and known $\overline{SOC}_p$, the average state of charge of the negative electrode is

$$\begin{aligned} \overline{SOC}_n &= \frac{SOC^p_{100\%} - \overline{SOC}_p}{SOC^p_{100\%} - SOC^p_{0\%}} \cdot \left(SOC^n_{100\%} - SOC^n_{0\%}\right) \\ &\quad + SOC^n_{0\%} \end{aligned} \tag{4.68}$$

A challenge of solving the diffusion equation by FDM is that (4.62) cannot provide an unique solution for SOC^{surf} from a known $\overline{SOC}$. In this chapter, to develop a relationship from a known $\overline{SOC}$ to SOC^{surf}, (4.62) for the negative electrode is replaced by an approximation (4.29). The new model is called the hybrid SPM (HSPM) that diffusion equations are solved by FDM in the positive electrode and solved by 2 DAEs approximation in the negative electrode. Reasons for the replacement are that $\bar{c}_s$ in 2 DAEs approximation has high accuracy of $\bar{c}_s$ calculation and the open circuit potential of the negative electrode is flat as can be observed from Fig 4.15.

Overall, the dynamic system is of the form

$$\begin{aligned} \mathbf{x}_{k+1} &= \mathbf{A_d}\mathbf{x}_k + \mathbf{B_d} I_k \\ V_{cell,k} &= h(x_k, I_k) \end{aligned} \tag{4.69}$$

The Jacobian matrix of partial derivatives of h with respect to $\mathbf{x}$ is

$$\mathbf{H} = [\underbrace{0, \ldots, 0}_{M-2}, \frac{\partial h}{\partial SOC_p^{M-1}}] \tag{4.70}$$

the last term is

$$\begin{aligned} \frac{\partial h}{\partial SOC_p^{M-1}} &= \frac{\partial U_p}{\partial SOC_p^{M-1}} - \frac{\partial U_n}{\partial SOC_p^{M-1}} \\ &= \frac{\partial U_p}{\partial SOC_p^{surf}} \frac{\partial SOC_p^{M-1}}{\partial SOC_p^{surf}} - \frac{\partial U_n}{\partial SOC_n^{surf}} \frac{\partial SOC_n^{surf}}{\partial SOC_p^{M-1}} \end{aligned} \tag{4.71}$$

where

$$\begin{aligned} \frac{\partial SOC_n^{surf}}{\partial SOC_p^{M-1}} &= \frac{\partial SOC_n^{surf}}{\partial \overline{SOC}_n} \frac{\partial \overline{SOC}_n}{\partial \overline{SOC}_p} \frac{\partial \overline{SOC}_p}{\partial SOC_p^{M-1}} \\ &= -\frac{\left(SOC_{100\%}^n - SOC_{0\%}^n\right)}{SOC_{100\%}^p - SOC_{0\%}^p} \cdot \frac{dV_M}{V} \end{aligned} \tag{4.72}$$

To obtain an accurate model, HSPM parameters are refitted. New fitted parameters and MAE are shown in Table 4.7.

Table 4.7: Parameters for the HSPM

$D_{s,p}$ (m^2/s)	$R_{s,p}$ (kg/mol)	$k_{n,p}$ (kg/m^3)	$R_f(\Omega)$ 90% ∼ 80%	$R_f(\Omega)$ 80% ∼ 70%	$R_f(\Omega)$ 70% ∼ 60%	MAE (mV)
1.02×10^{-14}	1.21×10^{-5}	6.05×10^{-11}	0.052	0.0504	0.0394	6.098

A simpler SOC estimation method is employed using 2 DAEs in both electrodes. It simplifies the entire battery model and estimation system. However, the error on the terminal voltage from 2 DAEs approximation will lead to a bias in SOC estimation. Fig. 4.25 compares SOC estimation of HSPM and 2 DAEs SPM with real SOC. The test drive cycles are UDDS, US06, and HWY; as shown in Fig. 4.21. The input current contains white noise with variance from 0 to 0.9A. The initial condition of SOC has +5% error.

The comparison results show that the absolute SOC error of HSPM is lower than

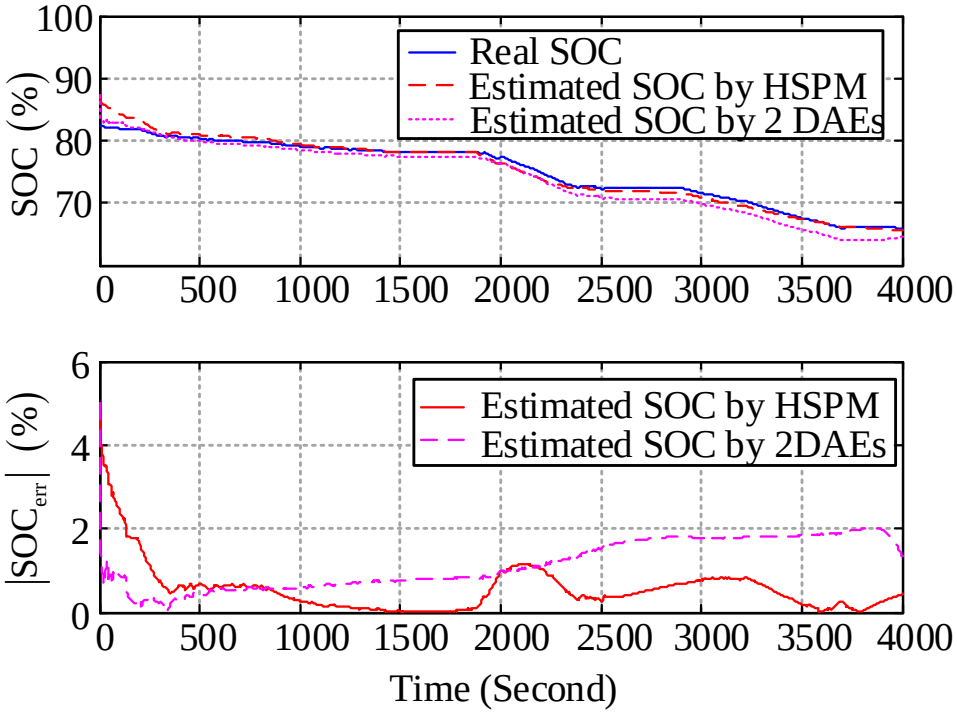

Figure 4.25: SOC estimation of HSPM and 2 DAEs SPM compare with real SOC

the error of 2 DAEs SPM. The SOC MAE of HSPM is 0.43% and the MAE of 2 DAEs SPM is 1.11%. The maximum absolute error of HSPM is 1.15% and the maximum absolute error of 2 DAEs SPM is 2.02%. An apparent drawback of HSPM is that the high order system makes the process noise covariance Q is difficult to determine and tune. Therefore, HSPM cannot follow the real SOC as quickly as 2 DAEs SPM which has only one element in the Q matrix.

Fig. 4.26 shows internal states $SOC_p^m, m = 1, \cdots, M-1$ and SOC on the spherical particle surface SOC_p^M of the cell through EKF. $SOC_p^m, m = 1, \cdots, M$ are drawn in gray lines. Red line and blue line are estimated average SOC and real SOC. The initial condition assumes SOC has +5% error. SOCs of each shell start from 87.2%. After around 300 seconds, SOCs of each shell can catch the real SOC.

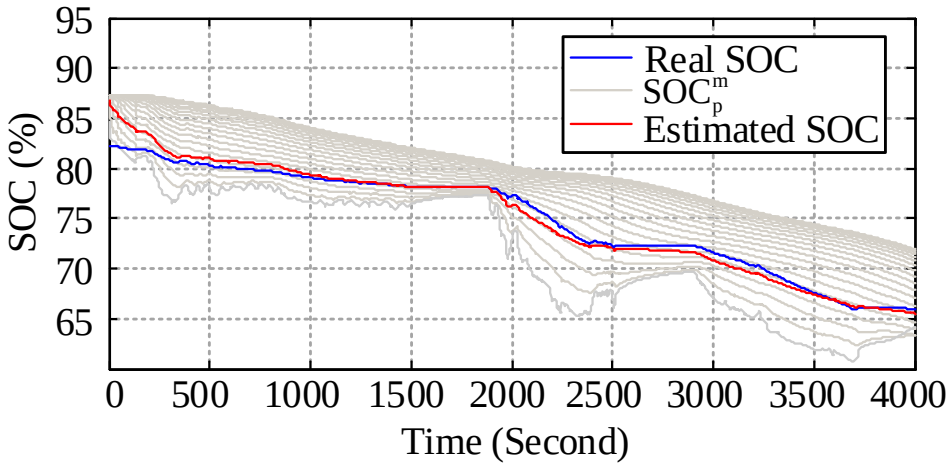

Figure 4.26: Internal states SOC_p^m in EKF, $m = 1, \cdots, M$

SOC-SOH joint estimation

In BMS, internal impedance and capacity of battery cells are important factors of SOH. In an aged battery, due to the SEI layer growth and the loss of lithium ions, the internal impedance will increase and the operation range in the negative electrode open circuit potential curve will shift to the left which leads to the OCV-SOC curve changes (Ning *et al.*, 2006). The OCV-SOC curve and the internal impedance would be used to estimate or derive the cell's capacity (Di Domenico *et al.*, 2015; Malysz *et al.*, 2016). The OCV-SOC could be observed from the electrochemical-based model, and the internal impedance needs to be estimated. The internal impedance is added into the state vector. The internal impedance changes slower than SOC variation, thus, the process equation for it are

$$R_{f,k+1} = R_{f,k} \tag{4.73}$$

In the measurement equation (4.44), the last three terms could be replaced by the term $R_f I$. R_f includes the linear resistance and nonlinear resistance. Therefore, the **H** matrix becomes

$$\mathbf{H} = [\underbrace{0, \ldots, 0}_{M-2}, \frac{\partial h}{\partial SOC_p^{M-1}}, I_k] \tag{4.74}$$

Impedance estimation for the 1^{st} cycle and 50^{th} are shown in Fig. 4.27. The initial condition is 0.3Ω. Estimated impedance can quickly follow the off-line fitted impedance. For the first cycle, the MAE of the R_f achieves 0.0064Ω. For the 50^{th} cycle, the MAE of the R_f is 0.0062Ω.

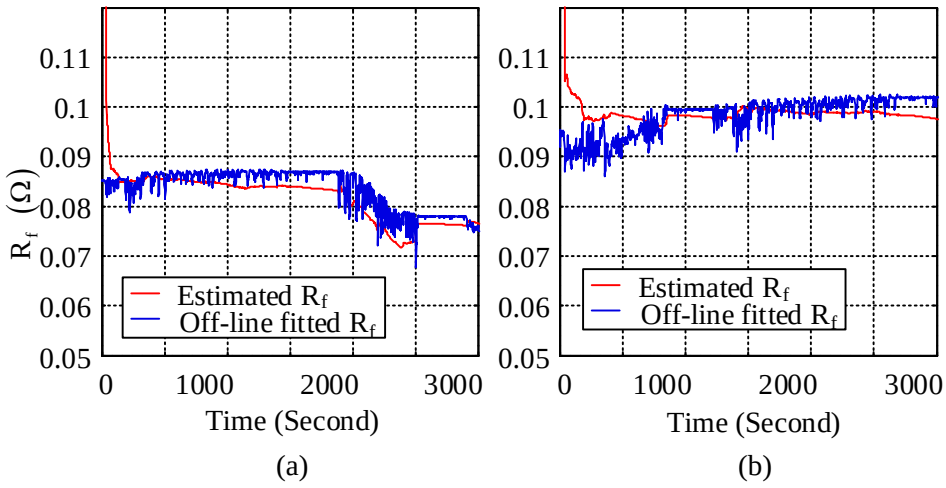

Figure 4.27: Estimated internal impedance (a) the 1st cycle, (b) the 50th cycle

The order of the estimation system is higher, therefore the process noise covariance Q and measurement noise covariance R need to be adjusted. Finally, the MAE of the SOC estimation in the SOC-SOH joint estimation system is 0.5% which is lower than the SOC-only estimation system. Fig. 4.28 indicates that the estimated SOC in the joint estimation system can follow the real SOC. However, the response time of it is slower than the SOC-only estimation system.

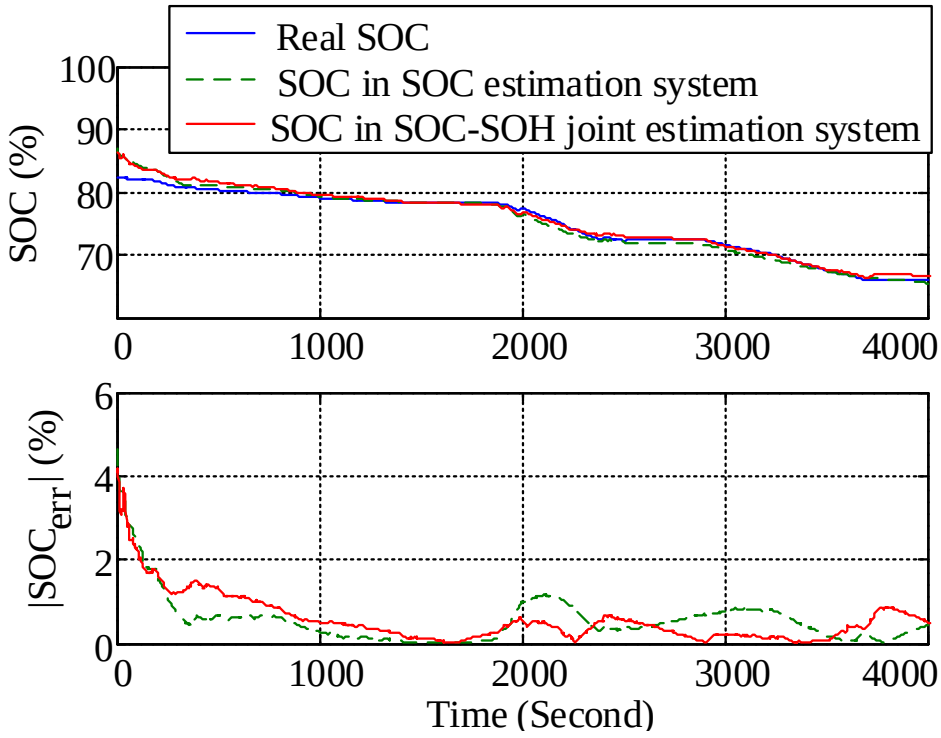

Figure 4.28: Comparison of SOC estimation in two estimation systems

4.5 Equivalent circuit modeling for ultracapacitor

Ultracapacitor is a type of the electrochemical capacitors with a high energy density which is similarly known as electrochemical double layer capacitor. The large surface area and extremely small charge separation lead to the ultracapacitor has higher capacitance than conventional capacitors.

Even though the energy density of the ultracapacitor is still lower than the lithium-ion battery, the ultracapacitor has significantly higher power density. And the low internal impedance provides high efficiency of the ultracapacitor. Moreover, the cycle life of ultracapacitor can achieve to 500,000 cycles (Maxwell, 2013). The ultracapacitors can be used to combine with the lithium-ion batteries to absorb and release high

power for regenerative braking and acceleration.

4.5.1 Equivalent circuit model

Due to the stable internal states and long cycle life, the ultracapacitor can use the equivalent circuit modeling techniques. In (Manla *et al.*, 2011; Shi and Crow, 2008; Tao and Li, 2014), several models had been introduced. They can be categorized into four basic classes: the simplest model, the RC parallel branch model, the RC transmission line model, and the RC series-parallel branch model. Those models are reviewed in this section.

- The simplest model

  The simplest model just has a RC branch as show in Fig. 4.29. The resistor R represent the equivalent series resistor (ESR) and the capacitor C is the capacity of the ultracapacitor. The transfer function of this model is

  $$Z(s) = R + \frac{1}{sC} \tag{4.75}$$

  A primary disadvantage of this model with the simple structure is that it cannot capture the voltage behavior after the charging or discharging stops. Therefore, more terms are needed in the ultracapacitor model.

- RC parallel branch model

  This model consists of several RC branches as shown in Fig. 4.30. More RC branches can enhance the accuracy of the model. Usually, two or three branches can maintain a high accuracy with uncomplicated modeling process. For ease of

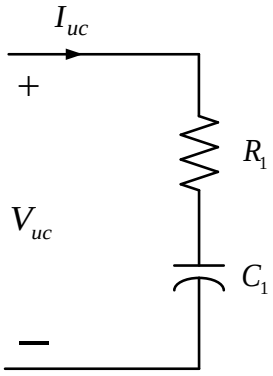

Figure 4.29: The simplest model

analysis, this figure just shows a RC parallel branch model with 2 RC branches. The transfer function of this model takes the form of

$$Z(s) = \frac{R_1 R_2 + \frac{R_1}{sC_2} + \frac{R_2}{sC_1} - \frac{1}{C_1 C_2}}{R_1 + \frac{1}{sC_1} + R_2 + \frac{1}{sC_2}} \tag{4.76}$$

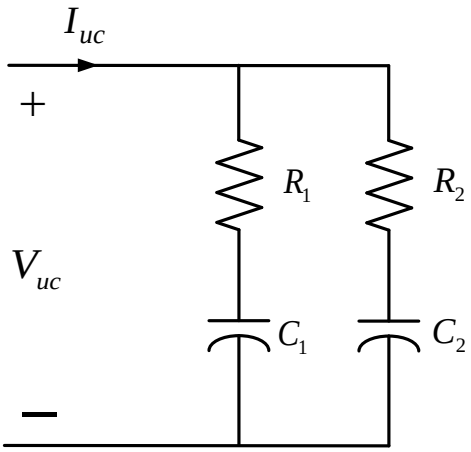

Figure 4.30: RC parallel branch model

- RC transmission line model

The RC transmission line model was developed from porous electrode theory to approach the electrolyte resistance and double-layer capacitance. The ultracapacitor's physical structure and electromechanical characteristics are directly reflected by the RC transmission line model. A two order RC transmission line model is shown in Fig. 4.31. However, this model is difficult to simulate and

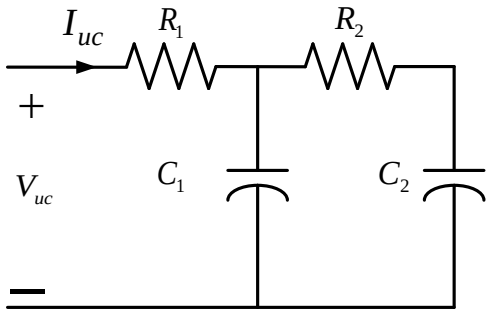

Figure 4.31: RC transmission line model

analyze due to the complicated analytical expression. The transfer function of the two order RC transmission line model takes the form of

$$Z(s) = R_1 + \frac{\frac{R_2}{sC_1} + \frac{1}{s^2C_1C_2}}{\frac{1}{sC1} + R_2 + \frac{1}{sC_2}} \tag{4.77}$$

Even though the two order model is straightforward, a high order RC transmission model would be intricate and need to be transferred to other models for a transparent solution.

- RC series-parallel branch model

  Fig. 4.32 shows a two order RC series-parallel branch model. In this model, R_1 represents the equivalent series resistance. The ultracapacitor's pore impedance

is represented by R_2, C_2, and C_1 which could be replace by another RC pair. The RC series-parallel branch model is widely used to simulate and observe the ultracapacitor. The transfer function is

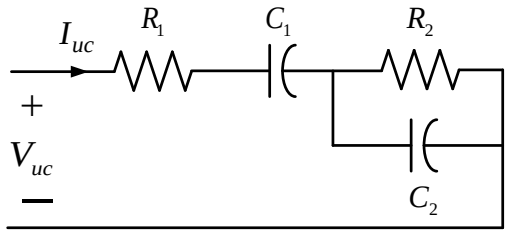

Figure 4.32: RC series-parallel branch model

$$Z(s) = R_1 + \frac{1}{sC_1} + \frac{\frac{R_2}{sC_2}}{R_2 + \frac{1}{sC_2}} \tag{4.78}$$

4.5.2 Parameterization

Similar to the parameterization for battery, parameters in the ultracapacitor's equivalent circuit models could be fitted by numerical optimization. In this subsection, an one order equivalent circuit modeling which includes one equivalent series resistance and one RC pair, as shown as in Fig. 4.33, is fitted and compared with the test data.

The discrete time-domain equations for the ultracapacitor models are

$$\begin{aligned} V_{k+1}^{uca} &= e^{-\frac{\Delta T}{R_{uca}C_{uca}}} V_k^{uca} + R_{uca}(1 - e^{-\frac{\Delta T}{R_{uca}C_{uca}}}) I_k^{uc} \\ V_k^{uc} &= V_k^{uca} + R_{uco} I_k^{uc} \end{aligned} \tag{4.79}$$

Parameters R_{uco}, R_{uca}, and C_{uca} in the model can be fitted by numerical optimization in Matlab. In this chapter, an ultracapacitor module which connects two

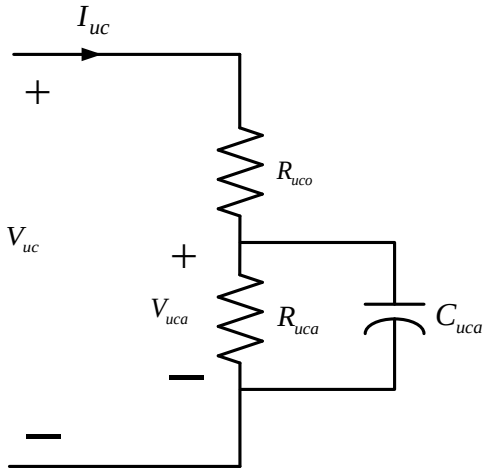

Figure 4.33: Equivalent circuit models of ultracapacitor

Maxwell BCAP0350 cells in series is tested by current pulses with different magnitude. Fitting results for this module are shown in Table 4.8. The mean square error (MSE) is 1.71×10^{-5}V. Tested current, voltage, fitted voltage curve, and absolute voltage error of this model are shown in Fig 4.34.

Table 4.8: Fitting result of BCAP0350

R_{uco} (Ω)	R_{uca} (Ω)	C_{uca} (F)	MSE (V)
0.0451	50.241	193.131	1.71e-5

4.5.3 SOC of an ultracapacitor

From (2.10), the state of charge of an ultracapacitor could be directly calculated by using the terminal voltage. The state of charge of an ultracapacitor is

$$SOC = \frac{E}{\frac{1}{2}C(V_{max}^2 - V_{min}^2)} = \frac{\frac{1}{2}C(V^2 - V_{min}^2)}{\frac{1}{2}C(V_{max}^2 - V_{min}^2)} \tag{4.80}$$

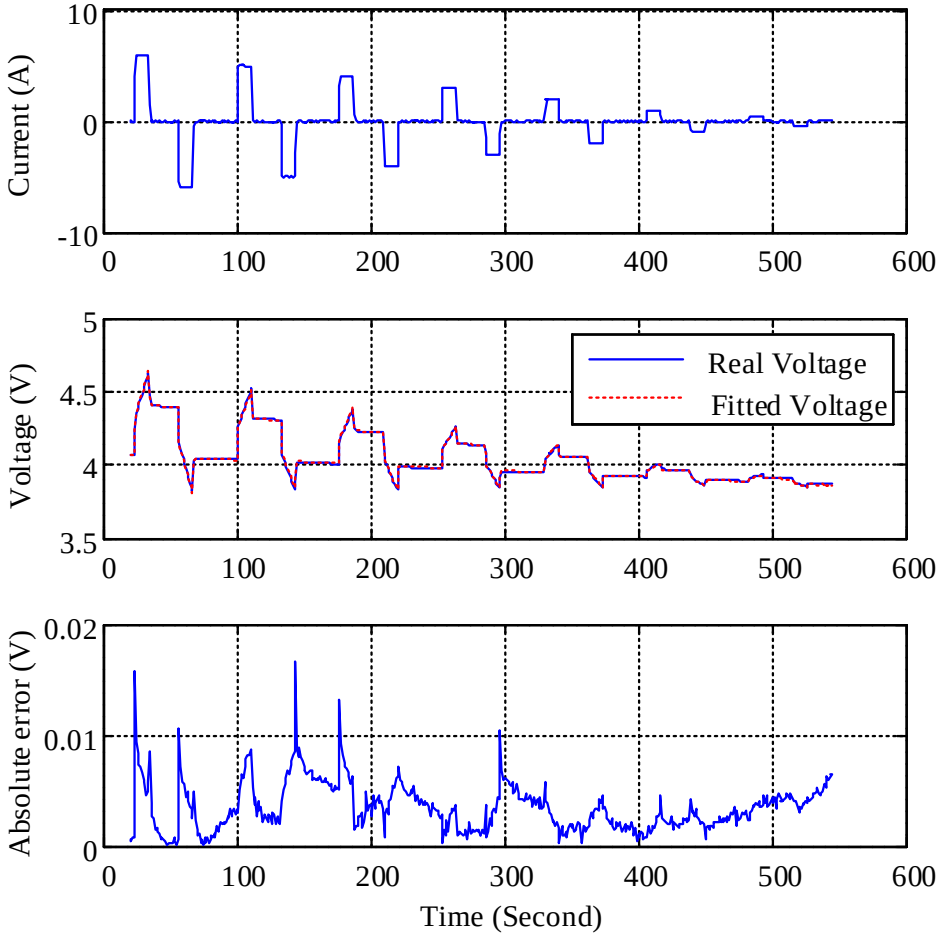

Figure 4.34: Fitted voltage curve of BCAP0350

4.6 Conclusion

In this chapter, the equivalent circuit modeling and physics-based modeling techniques for the lithium-ion battery and the equivalent circuit modeling techniques for the ultracapacitor are introduced. They are applied to the analysis in the remainder of the research. Equivalent circuit modeling for the lithium-ion battery and ultracapacitor are widely used in the practical energy storage systems. Moreover, pseudo-two dimensional model, several reduced-order techniques, and SEI layer growth model

have been reviewed in this chapter. With a focus on BMS development, the SPM method is explored based on following aspects:

- Definitions of cell level quantities in electrochemical-based model
- Numerical solution for diffusion equation
- Parametrization method
- Effects of the number of shells in a spherical particle
- SEI layer growth model
- Introduction of a new so-called HSPM amenable for BMS development
- SOC and SOH estimation based on HSPM

An SPM of a Panasonic NCR18650A cell is developed and compared to experimental data using UDDS, US06, and HWY driving cycles. Results show that SPM can provide an accurate model with 3.811mV for UDDS driving cycle, 6.216mV for HWY driving cycle, and 11.473mV MAE for US06, even though US06 driving cycle includes high current pulses. For SOC and SOH estimation in SPM, an observable HSPM which combines FDM and 2 DAEs for solving diffusion equations is used with EKF. HSPM has simplified many physics processes from the full-order model, however, the order of the system is higher such that the process matrix Q in EKF can be more difficult to tune. Future work will attempt to use adaptive filters to track states of battery in short time. Alternative reduced order models will be investigated from a parametrization and states estimation point of view.

Chapter 5

Hybrid Energy Storage System Analysis based on Physics-Based Lithium-ion Battery Modeling

5.1 Introduction

In this chapter, the lithium-ion batteries in a direct coupled hybrid energy storage system are compared with the single lithium-ion battery in terms of the external performance, internal states, and aging effects by the single particle model with SEI layer growth model and experimental results. Firstly, this thesis proposes a novel hybrid energy storage system that combines a lithium-ion battery and an ultracapacitor at the cell level through a small size bi-directional DC-DC converter. The combination at the cell level supports more flexible control capability depending on different internal states and external states of each cell. Different positions in a battery pack may have different temperatures, therefore, states of batteries may be not the same.

Although applying this topology in a large size energy storage system increases the complexity and cost, this topology could be used to observe the performance of a lithium-ion battery in an active hybrid energy storage system.

Inspired by the principle of the lithium-ion capacitor which replaces the cathode of a lithium-ion battery by the activate carbon, a direct coupled hybrid energy storage module which connects the batteries and ultracapacitors in parallel is proposed. The direct coupled ultracapacitors improve the power capability of the lithium-ion batteries and keep a higher specific energy than the lithium-ion capacitor. The ultracapacitors perform as a low pass filter that receives and releases the high frequency components of power. Moreover, as the main aging mechanism, the high frequency regenerative pulses are received by the ultracapacitors, therefore, the lifespan of the lithium-ion battery is also prolonged. The SEI layer growth and capacity fade of a lithium-ion battery are validated by the physics-based modeling and experimental results. As a component in an energy storage system, SOC and SOH of the batteries in a direct coupled hybrid module are important states need to be estimated. Without the additional current sensor, this thesis develops the SOC-SOH joint EKF estimator based on the physics-based modeling for the lithium-ion battery in a direct coupled hybrid module.

5.2 Active hybrid module

5.2.1 Active hybrid module configuration

Conventionally, hybrid energy storage system in an electrified vehicle is the combination of battery pack and ultracapacitor pack. To obtain more flexible control

capability, a novel hybrid energy storage system that combines battery and ultracapacitor at the cell level is proposed. In a battery string, each battery cell is connected with an ultracapacitor in parallel through a bi-directional DC-DC converter. This hybrid module controls power flow not only depending on power demand but also the state of charge, internal resistance, capacity and external temperature of each battery cell. The configuration is shown in Fig. 5.1. The voltage range of a typical lithium-ion

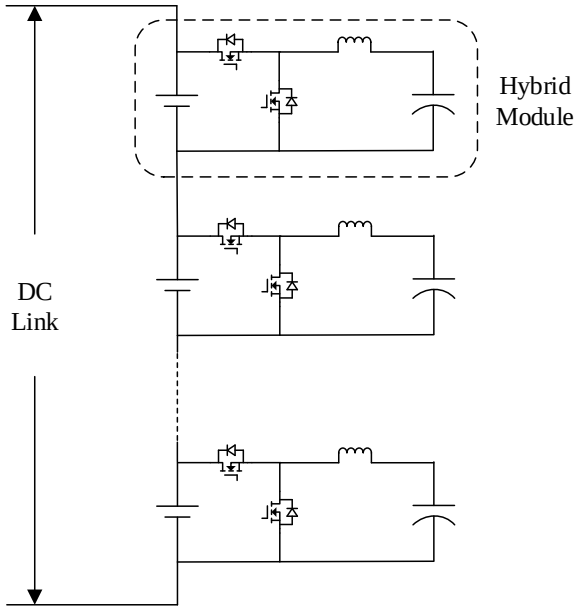

Figure 5.1: Active hybrid module string

cell is from 2.5V to 4.2V. The maximum voltage of ultracapacitor is 2.85V. To avoid battery is overdischarged and ultracapacitor is overcharged, the battery side voltage is higher than ultracapacitor side voltage. Therefore, a half-bridge DC-DC converter can be used in this topology.

5.2.2 Rule-Based Control strategy

In this research, power split of the hybrid cell is controlled by a rule-based control strategy.

1. In generative braking ($P_{req} < 0$), ultracapacitor absorbs regenerative braking power as much as possible.

2. In discharging ($P_{req} > 0$),

   - If $P_{req} > P_{limit}$, battery supplies P_{limit} and ultracapacitor supplies remaining power ($P_{req} - P_{limit}$).
   - If $P_{req} < P_{limit}$ and $U_{UC} < U_{ref}$, battery sends power to load and charges ultracapacitor.

3. Prevent battery and ultracapacitor overcharge and overdischarge.

P_{req} is the power demand, P_{limit} is a limit power sent by battery, U_{UC} represents the ultracapacitor voltage, and U_{ref} is a reference voltage on ultracapacitor. Ultracapacitor cannot keep at high voltage or low voltage because ultracapacitor needs to prepare for coming regenerative braking or acceleration. The reference voltage varies depending on current speed. When the vehicle is driving at a low speed, ultracapacitor should absorb energy for acceleration. When the vehicle is driving at a high speed, ultracapacitor should release energy for receiving regenerative braking energy.

5.2.3 Electric Vehicle Driving Cycles

To evaluate the performance of the hybrid cell, this configuration is tested under three driving cycles: UDDS, HWY, and US06. The velocity profiles of these driving cycles are provided by United States Environmental Protection Agency (EPA, 1996). Demanded power of these velocity profiles can be calculated from the vehicle kinematics (Emadi, 2014).

Four forces that are worked on a vehicle are:

$$F_d = F_{rr} + F_{rf} + F_a + F_{tf} \tag{5.1}$$

$$F_{rr} = k_r mg\cos\theta \tag{5.2}$$

$$F_{rf} = mg\sin\theta \tag{5.3}$$

$$F_a = \frac{1}{2}\rho C_d A_f v^2 \tag{5.4}$$

$$F_{tf} = m\frac{dv}{dt} \tag{5.5}$$

where F_{rr}, F_{rf}, F_a and F_{tf} are the rolling resistance, the resistive force, the aerodynamic resistance or drag force and the transient force required to accelerate the vehicle, respectively. k_r is the rolling resistance coefficient, m is the vehicle mass, θ is the road gradient, g is the gravitational constant, ρ is the density of air, C_d is the drag force coefficient, A_f is the vehicle frontal area, and v is the vehicle linear velocity.

The road wheel torque is

$$T_w = J_w\frac{d\omega_w}{dt} + d_f r_w F_d \tag{5.6}$$

where J_w is the wheel inertia, ω_w is the angular velocity, r_w is radius, and d_f is a factor proportioning torque distribution on the rear axle. The traction machine torque is

$$T_m = J_m \frac{d\omega_m}{dt} + \frac{1}{n_t \eta_t} T_w \tag{5.7}$$

where n_t is the total transmission gear ration, η_t is transmission efficiency, and J_m is the machine rotor inertia. Follow Eq. (5.1), (5.6), and (5.7), mechanical power is

$$P_m = T_m \omega_m \tag{5.8}$$

where $\omega_m = n_t \frac{v}{r_w}$ is traction machine angular velocities.

Characteristics of the electric vehicle are shown in Table 5.1.

Table 5.1: Electric Vehicle Characteristics

Parameter	Value	Units
Total gear and differential ratio n	8.83	pu
Total gear and differential efficiency n	1	pu
Wheel inertia J_w	0.164	kgm^2
Motor inertia J_m	5.7×10^{-4}	kgm^2
Wheel radius r_w	0.274	m
Distribution factor d_f	1	factor
Rolling resistance k_r	0.0267	
Air density ρ	1.23	kg/m^3
Mass m	1570	kg
Frontal area A_f	1.75	kg/m^3
Drag force coefficient C_d	0.31	

5.2.4 Sizing of Hybrid ESS

From above vehicle kinematics, the peak power of three driving cycles can be calculated. The maximum peak power is 97kW in US06. When designing an energy

storage system, the system needs to satisfy the requirement of the peak power and voltage on DC-link. Panasonic NCR18650A cell has the 3.1Ah capacity with 1 C-rate capability and 3.7V rated voltage. Therefore, 96 cells are connected in series to reach the requirement of DC-link in a string. 45 strings are connected in parallel to ensure the discharge current provided by each battery cell is less than 6A. As a high specific power storage system, the ultracapacitor can supply high C-rate discharge current. Moreover, ultracapacitor can absorb regenerative braking energy which is an important reason leads to SEI growth. In this topology, Maxwell 350F ultracapacitor is selected.

5.2.5 Simulation results and discussion

Using the active hybrid module in a large size energy storage system, the cost, size, weight, and complexity of control would be the challenges. However, the physics-based modeling in this topology could be used to evaluate the performance and SEI layer growth of battery under driving cycles. Fig. 5.2, 5.3, and 5.4 show power and current split of the hybrid module under UDDS, HWY and US06. UDDS has many acceleration and regenerative braking, therefore, high power flows in/out the ultracapacitor, and the magnitude of current in/out the battery can be greatly reduced. On the highway, the vehicle maintains a high speed and the energy storage system needs to supply power in a long time and receive high regenerative braking power in a short time. US06 represents high acceleration aggressive driving habits with the high current spikes. Ultracapacitor can quickly absorb and release the high power pulses and reduce the impacts of them on battery.

SEI layer growth of battery cell in the hybrid cell and battery-only cell under

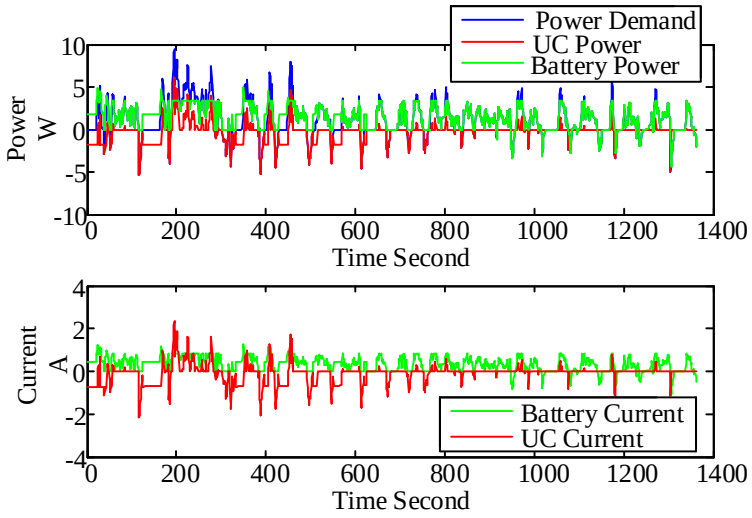

Figure 5.2: Power and current split of a single hybrid cell under UDDS drive cycle

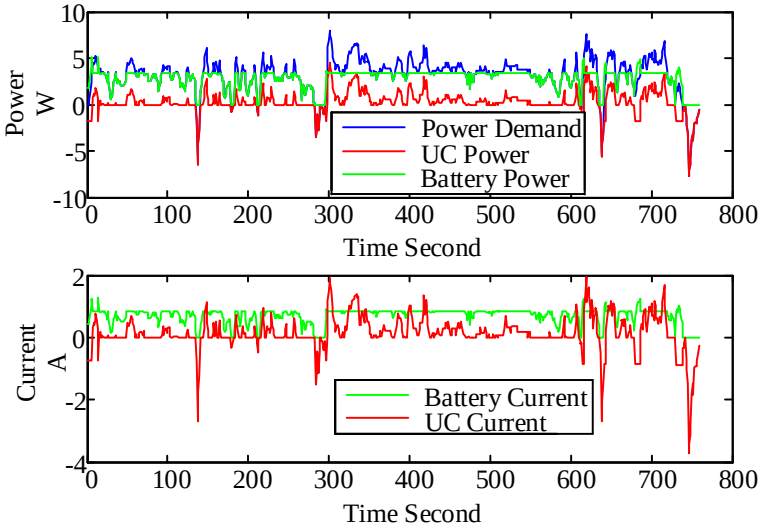

Figure 5.3: Power and current split of a single hybrid cell under HWY drive cycle

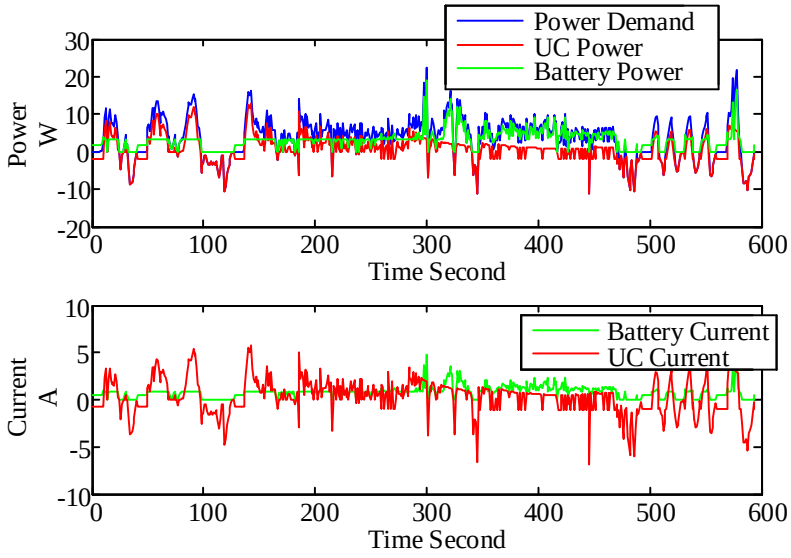

Figure 5.4: Power and current split of a single hybrid cell under US06 drive cycle

each driving cycle are compared in Fig. 5.5. The duration of each driving cycle is different, so each of them is repeated several times until the depth of discharge of the battery cell is 70%. This figure is normalized to the growth of the battery-only cell. Solid lines represent SEI growth of battery in hybrid cell, and dashed lines represent SEI growth of the battery-only cell. For the battery-only cell, the greatest amount of regenerative braking in UDDS results in SEI layer increases faster than others. The hybrid cell greatly receives regenerative braking power and SEI layer growth is slower than the battery-only cell.

Fig. 5.6 shows SEI growth of hybrid cell and the battery-only cell under each driving cycle over 2 hours. Comparing with three driving cycles for the battery-only cell, battery under US06 has the thickest SEI layer. Even though high frequency regenerative braking increases SEI layer, a battery maintains at a high SOC level under UDDS. Aggressive stop and acceleration under US06 lead to SEI layer are

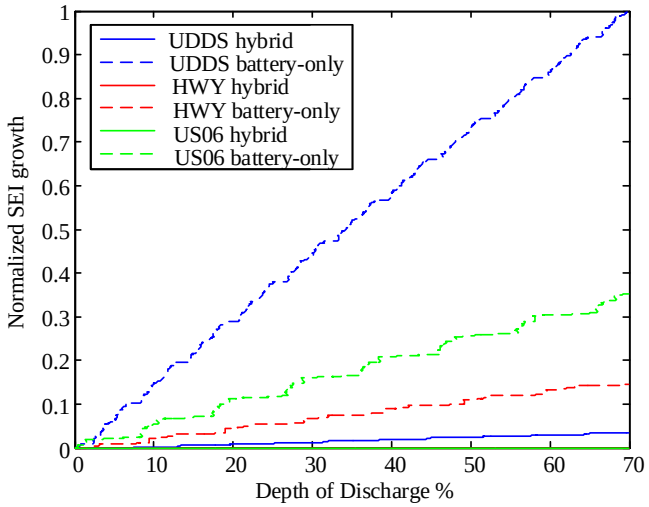

Figure 5.5: SEI growth of hybrid cell and battery-only for a 70% depth of discharge of UDDS, HWY, and US06. HWY hybrid line is overlapped by US06 hybrid line.

thicker than UDDS over the same length of time.

5.3 Direct coupled hybrid module

5.3.1 Direct coupled hybrid module

A direct coupled hybrid module which directly connects ultracapacitors cells with lithium-ion battery cells in parallel at the module level is proposed. The performance of the direct coupled hybrid module and extended modules are analyzed.

Modeling

To observe the internal states and aging effects of the lithium-ion battery in the direct coupled hybrid module, the SPM with the aging model is applied to the lithium-ion

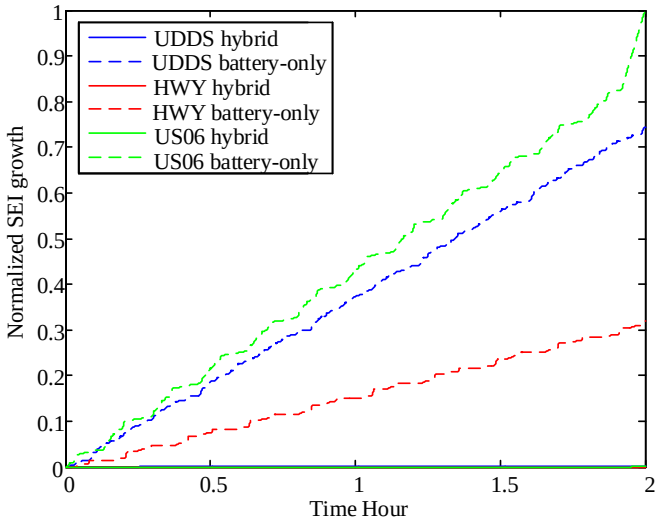

Figure 5.6: SEI growth of hybrid cell and battery-only for 2 hours under UDDS, HWY and US06. HWY hybrid line is overlapped by UDDS hybrid and US06 hybrid lines on the x-axis.

battery modeling. Due to the high stability and long lifespan, changes of ultracapacitor's parameters and aging effects are neglected. The ECM is used for ultracapacitors. The currents flow into the battery branch and the ultracapacitor branch need to be calculated as input signals for the battery and ultracapacitor models. Equations in SPM are too complicated for analytic solutions, these two currents are found by using bisection and interpolation algorithms to confirm voltage on two branches are same. The schematic of the direct coupled hybrid model is shown in Fig. 5.7. Parameters of the model are from Table 4.4 and Table 4.8 which were fitted for the lithium-ion battery SPM and ultracapacitor ECM separately.

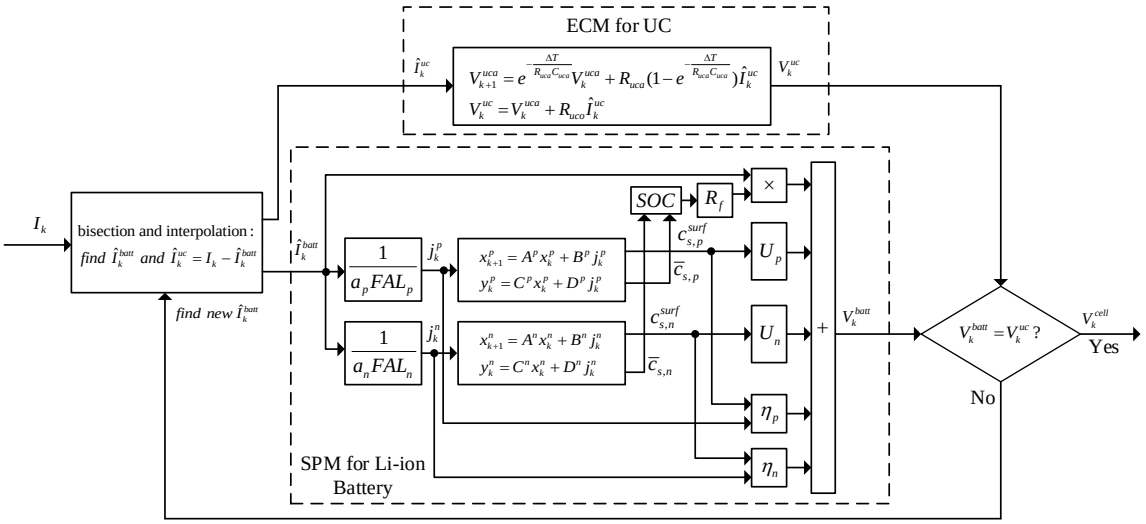

Figure 5.7: Schematic of the direct coupled hybrid module

Design for direct coupled hybrid module

To increase the specific power of the lithium-ion battery, prolong battery's life cycle and decrease energy loss, the direct coupled hybrid module is needed to be optimized and designed from following aspects: value and position of a current limiting resistor, the number of battery cells and ultracapacitor cells in series and in parallel.

- Cutoff frequency

  To absorb and release high frequency regenerative braking and acceleration power, ultracapacitor works in this topology without active power split circuit as a low-pass filter. The cutoff frequency is influenced by the value and position of a current limiting resistor R_{limit}, the number of the ultracapacitor branches $N_{UC}^{parallel}$, the number of battery branches $N_{Batt}^{parallel}$, the number of ultracapacitor cells in series N_{UC}^{series}, and the number of battery cells in series N_{Batt}^{series}. Three topologies can be considered as shown in Fig. 5.8. By plotting the attenuation

of the current flows into the battery branch $Gain(dB) = 20log_{10}\frac{I_{Batt}}{I_{Hybrid}}$ against different values of the input current frequency, the frequency response curve of the hybrid modules with different configurations are shown in Fig. 5.9.

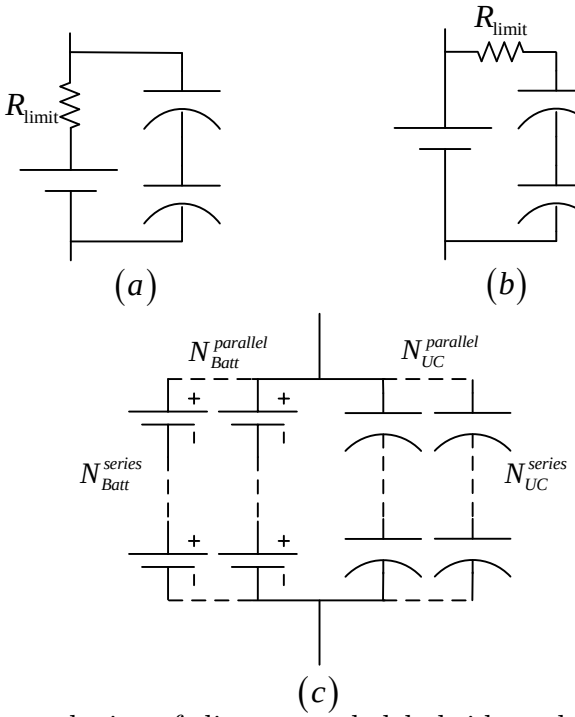

Figure 5.8: Three topologies of direct coupled hybrid module. (a) R_{limit} is in the battery branch, (b) R_{limit} is in the ultracapacitor branch, (c) general topology

In most of the cases, different kinds of energy sources are connected in parallel is dangerous, because of a little voltage difference may lead to a large inrush current between energy sources. To protect energy sources, a current limiting resistor may be needed between the battery cells and ultracapacitor cells. The position of the current limiting resistor R_{limit} can vary the cutoff frequency. The resistor can be placed in the battery branch or ultracapacitor branch as shown in Fig. 5.8 (a) and (b). The frequency responses for these two topologies are shown

in Fig. 5.9(a). A hybrid module is assumed that a battery cell connects with two ultracapacitor cells in parallel and the current limiting resistance is 0.1Ω. Magnitudes of these two options are nearly close to $0dB$ for low frequencies and the most of the currents flow into the battery branch. For high frequencies input current, the magnitude of current flows into the battery is greatly attenuated in the hybrid module which has R_{limit} on the battery branch. The attenuation rate is $-22.5dB(7.5\%)$ at $0.1Hz$. The other topology with a R_{limit} on the ultracapacitor branch just has a poor attenuation rate $-6.74dB(46\%)$ at $0.1Hz$. The reason is that the R_{limit} increases the impedance of the ultracapacitor branch. To reduce magnitudes of currents flow into the battery branch at high frequencies, the resistor should be placed on the battery branch to limit high inrush current and increase the impedance of this branch.

The frequency responses could be adjusted by a varying R_{limit}. The frequency responses of a changing R_{limit} from 0 to 0.1Ω are shown in Fig. 5.9(b). The arrow in the figure directs the direction of R_{limit} increasing. A higher resistance can increase the impedance on the battery branch and resist more currents which flow into the battery.

To reduce the impedance on the ultracapacitor branch, capacitance on the ultracapacitor side could be increased by increasing the number of ultracapacitor branches. Frequency responses of $N_{UC}^{parallel} = 1, 2, 3$ are shown in Fig. 5.9(c). A hybrid module is assumed that the number of battery cell in series is 1, the number of ultracapacitor cell in series is 2, and $R_{limit} = 0\Omega$. It indicates that the system has a lower gain with more numbers of ultracapacitor branches.

Fig. 5.9(d) presents the impacts of the number of battery cells in parallel

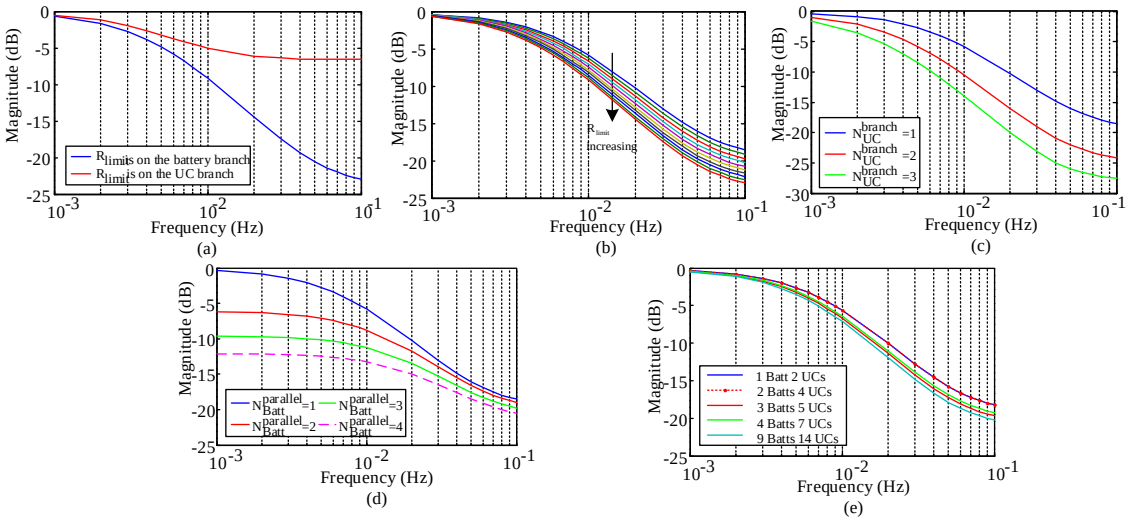

Figure 5.9: Frequency responses of different hybrid module combinations, (a) Frequency responses of two topologies with two R_{limit} positions, (b) Frequency responses of the hybrid module with R_{limiit} from 0 to 0.1Ω, (c) Frequency responses of the hybrid module with $N_{UC}^{parallel} = 1, 2, 3$, (d) Frequency responses of the hybrid module with $N_{Batt}^{parallel} = 1, 2, 3, 4$, (e) Frequency responses of the hybrid module with different N_{Batt}^{series} and N_{UC}^{series}

$N_{Batt}^{parallel}$. Connecting more battery cells in parallels leads to the impedance of battery side reduces and the attenuation rate reduces, especially for low frequency.

Effects of the number of battery cells and number of ultracapacitor cells in each branch are also researched. $N_{Batt}^{series} = 1, 2, 3, 4$ are considered. Battery cells and ultracapacitor cells are directly connected, so the voltage on each branch should be matched. The voltage range of a lithium-ion cell is from 2.5V to 4.2V, and the maximum voltage of ultracapacitor cell is 2.7V. To match battery side voltage and sufficiently use energy in ultracapacitor, one battery cell needs two ultracapacitor cells(1B2U), two battery cells need four ultracapacitor cells(2B4U), three battery cells need five ultracapacitor cells(3B5U), and four

battery cells need seven ultracapacitor cells(4B7U). Performance of the direct coupled hybrid module is related to the ratio $\gamma = \frac{N_{Batt}^{series}}{N_{UC}^{series}}$. To reduce the capacitance on the ultracapacitor branch, the number of ultracapacitor in series should be as less as possible and γ should be as high as possible. Fig. 5.9(e) shows five configurations frequency responses. Configurations 1B2U and 2B4U have same $\gamma = 0.5$, hence frequency responses of them are overlapping. The ratio γ of configuration 3B5U is 0.6 and the ratio γ of 4B7U is 0.57, therefore, 3B5U has higher attenuation rate than 4B7U. Both of them have higher attenuation rate than 1B2U and 2B4U. Based on the voltage limit, a configuration has 9 or multiple of 9 batteries in series and 14 or multiple of 14 ultracapacitors in series has the highest ratio $\gamma = 0.64$. The 65% energy stored in an ultracapacitor could be utilized.

- Current limiting and energy loss

  A large current limiting resistance can increase the attenuation rate and reduce the inrush current in the direct coupled hybrid module. However, the resistor also leads to energy loss in the hybrid module. Configuration 1B2U with varying R_{limit} from 0Ω to 0.1Ω on battery branch is tested under UDDS, US06, and HWY driving cycles. To research how much of the inrush current may generate in the hybrid module, the initial voltage of the lithium-ion cell is 4V and the initial voltage of the ultracapacitor cells are 2.1V. Therefore, the voltage difference between battery branch and ultracapacitor branch are $0.2V$. Energy loss in the hybrid module under different driving cycles and the inrush current are shown in Fig. 5.10. This figure indicates that the high current limiting resistance can reduce the inrush current but cause high energy loss. For the applications in

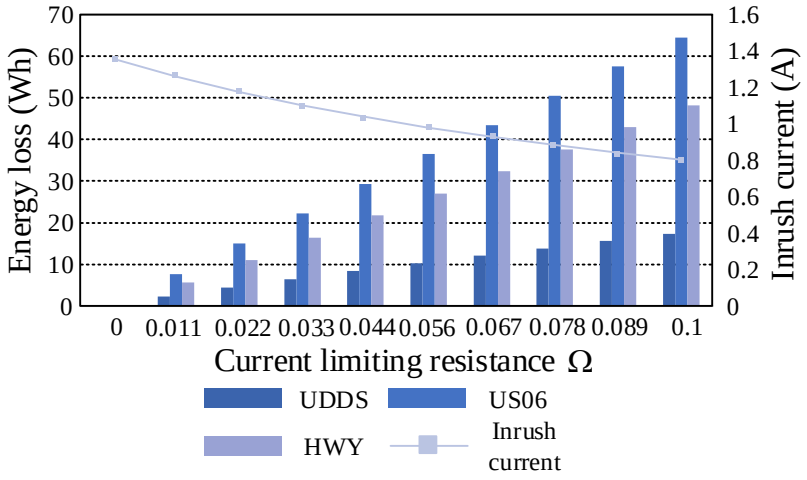

Figure 5.10: Inrush current and energy loss with different current limiting resistance

this thesis, NCR18650 has high internal resistance to limit the inrush current, therefore, there is no R_{limit} between the battery and ultracapacitor branches.

- Specific power

  The combination between battery cells and ultracapacitor cells can change the specific power of the energy storage system. Performance of the battery-only cell and direct coupled hybrid modules with different $N_{UC}^{parallel}$, $N_{Battery}^{parallel}$, N_{UC}^{series}, and $N_{Battery}^{series}$ are simulated under 2s, 5s, and 10s discharge pulses at the rate voltage 3.7V. The magnitude of the pulses needs to ensure the currents flow into battery and ultracapacitor do not exceed the maximum current $I_{Batt}^{max} = 6A$ and $I_{UC}^{max} = 170A$. Fig. 5.11 shows the current, voltage, and power curves of an 1B2U hybrid module and one battery-only cell under 10s discharge pulse. As shown in Fig. 5.11 (b), the magnitude of the 10s current pulse flows into the battery is 6A. In the 1B2U module, when the current flows into the battery reaches to 6A, the magnitude of the current flows into the hybrid module reaches to 12.7A. The last point in a pulse is utilized to define power capability. The configuration

1B2U can release higher power than the battery-only cell as shown in Fig. 5.11 (e) and (f).

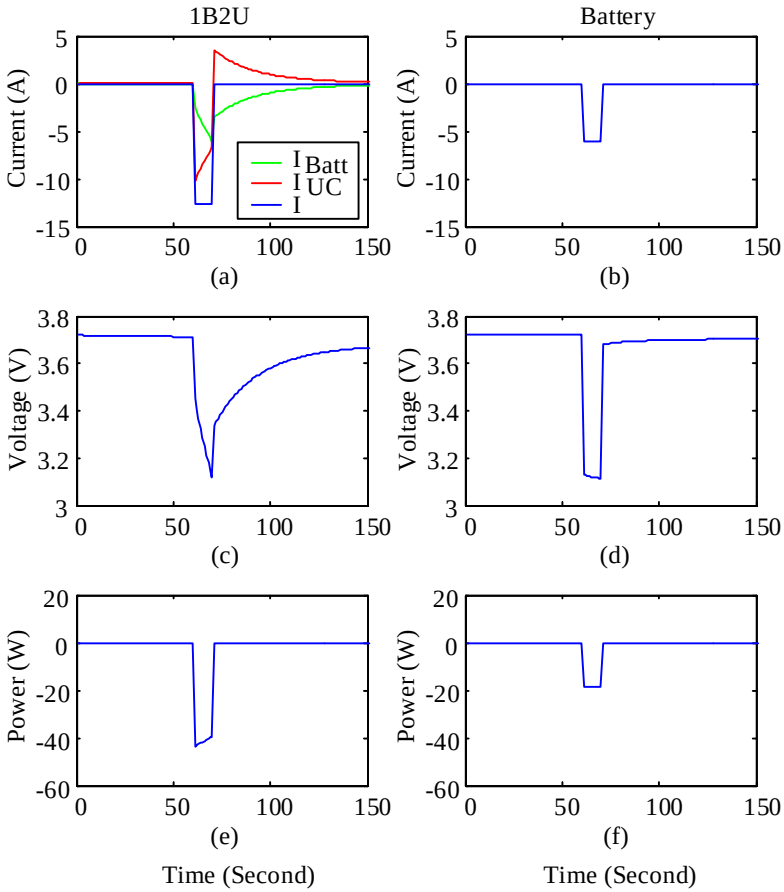

Figure 5.11: Current, voltage, and power curve of 1B2U module and battery-only cell under 10s constant current

Even though the hybrid module can release and receive higher power than battery cell, the weight of a module also increases. The specific power of different configurations is analyzed. The weight of BCAP350 is 60g (Maxwell, 2013), and weight of NCR18650A is 47.5g (Panasonic, 2012). Fig. 5.12 shows the specific power of the hybrid modules with different the ratio γ which relates to N_{Batt}^{series} and N_{Batt}^{series}. Blue, orange, and gray bars present the specific power of the

10s, 5s, and 2s pulses. Yellow line presents the ratio γ. For one combination, 2s pulse has the highest specific power, and 10s pulse has the lowest specific power. Overall, a hybrid module which has 9 or multiple of 9 N_{Batt}^{series} and 14 or multiple of 14 N_{UC}^{series} has the highest specific power for 10s, 5s, and 2s pulses. The trend of the specific power is the same with the variation of the ratio γ.

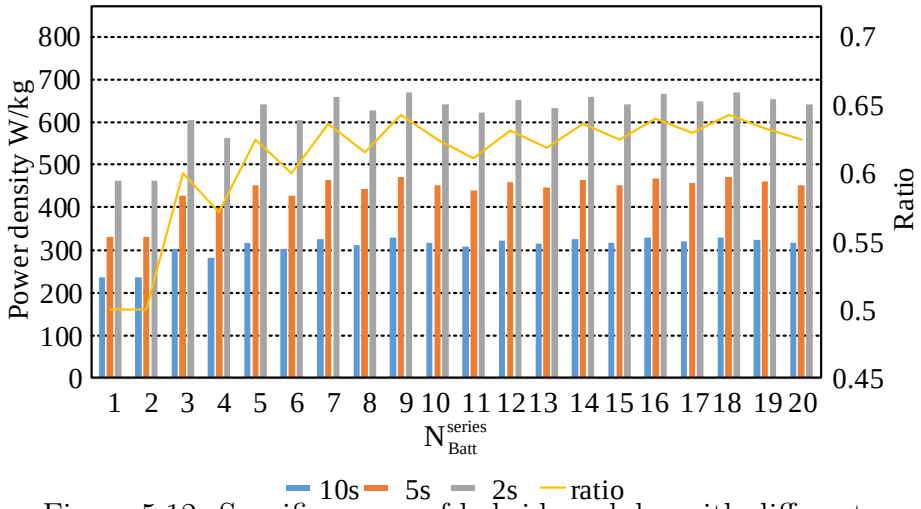

Figure 5.12: Specific power of hybrid modules with different γ

While a hybrid module has $N_{Batt}^{series} = 9$ and $N_{UC}^{series} = 14$, Fig. 5.13 shows specific power of battery and hybrid modules with different $N_{Batt}^{parallel}$ and $N_{UC}^{parallel}$. For the 2s pulse and 5s pulse, the specific power of the hybrid module is higher than the battery. For the 10s pulse, the specific power of the hybrid module is lower than the battery. A hybrid module with more $N_{UC}^{parallel}$ and less $N_{Batt}^{parallel}$ has higher specific power for the 2s and 5s pulses.

5.3.2 Simulation and experiment results

A direct coupled hybrid module 1B2U is tested under US06, UDDS, and HWY driving cycles. The experimental testbed is shown in Fig. 5.14. The input current of the

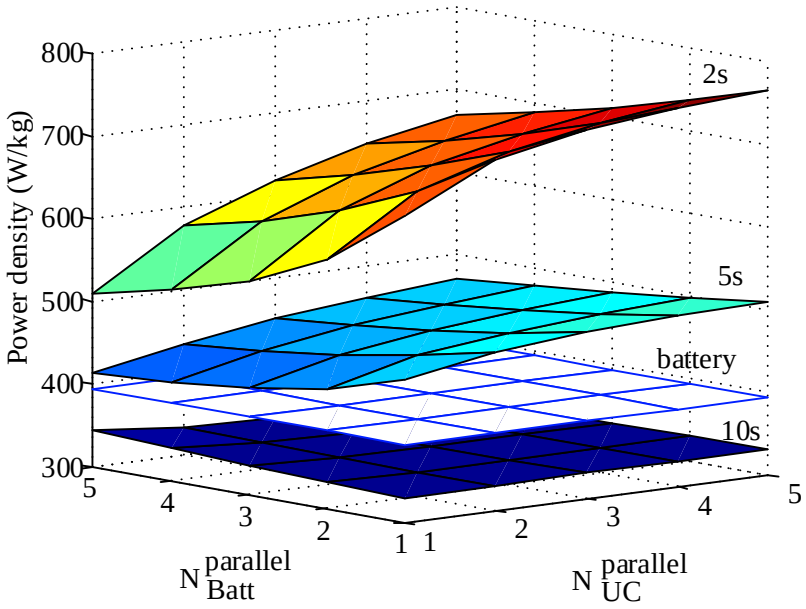

Figure 5.13: Specific power of hybrid modules with different $N_{Batt}^{parallel}$ and $N_{UC}^{parallel}$

hybrid module is controlled by a DC-DC converter from a 12V VRLA battery. The computer controls the DC-DC converter and records the input current and terminal voltage.

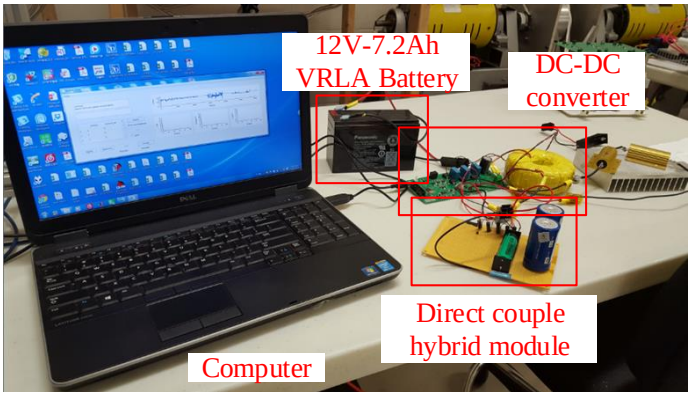

Figure 5.14: Experimental testbed

Fig. 5.15 compares voltage curves between the model and experiment results of the 1B2U module. Voltage MAE of this model is 4.5mV. Fig. 5.16 shows the real

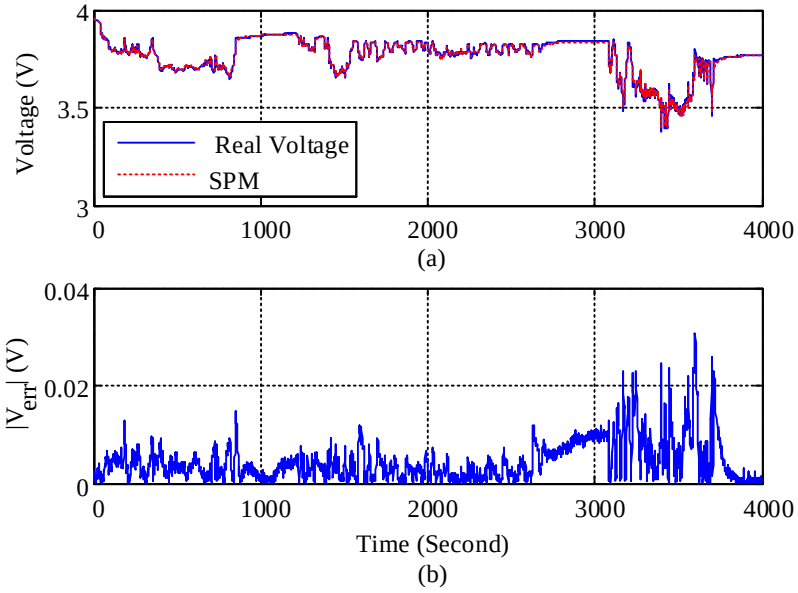

Figure 5.15: Comparison between voltage of the model and real data, (a) voltage curves, (b) absolute error

currents flow into the hybrid module I_{Hybrid}^{Real}, lithium-ion battery I_{Batt}^{Real}, the estimated currents flow into the lithium-ion battery I_{Batt}^{Model} and ultracapacitor I_{UC}^{Model}. MAE of the current flows into battery is $51.4mA$. This figure indicates that high frequency components of the input current are released/received by the ultracapacitors. There is little regenerative braking current flow into the lithium-ion battery.

The accurate physics-based modeling could be used to analyze the performance of the hybrid module. In order to observe internal states variations of the battery in a hybrid module and compare to the battery-only cell, an 1B2U hybrid module and a battery cell are simulated under repeated HWY, UDDS, and US06 drive cycles from fully charged to the cutoff voltage 3V. Voltage, SOC, and R_{SEI} curves are compared in Fig. 5.17. Fig. 5.17(a) shows that the hybrid module makes the terminal voltage on the battery smoother than the battery-only cell, hence, the hybrid module can avoid

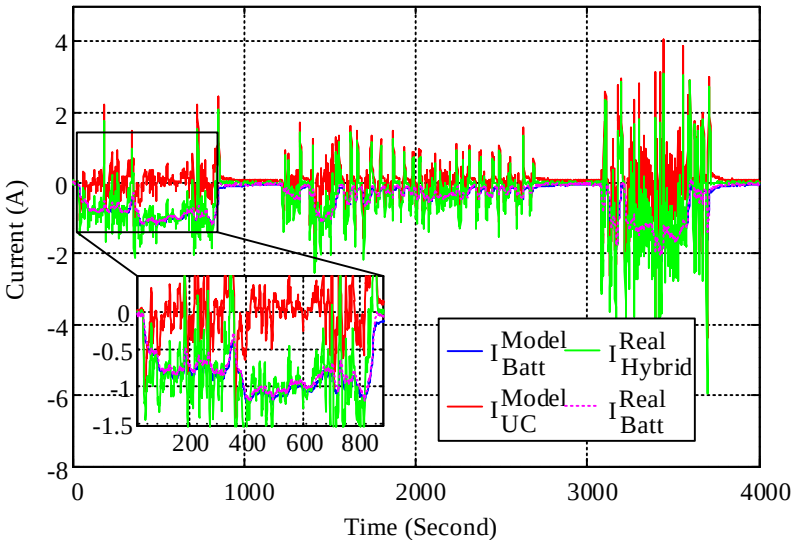

Figure 5.16: Comparison between current of the model and real data

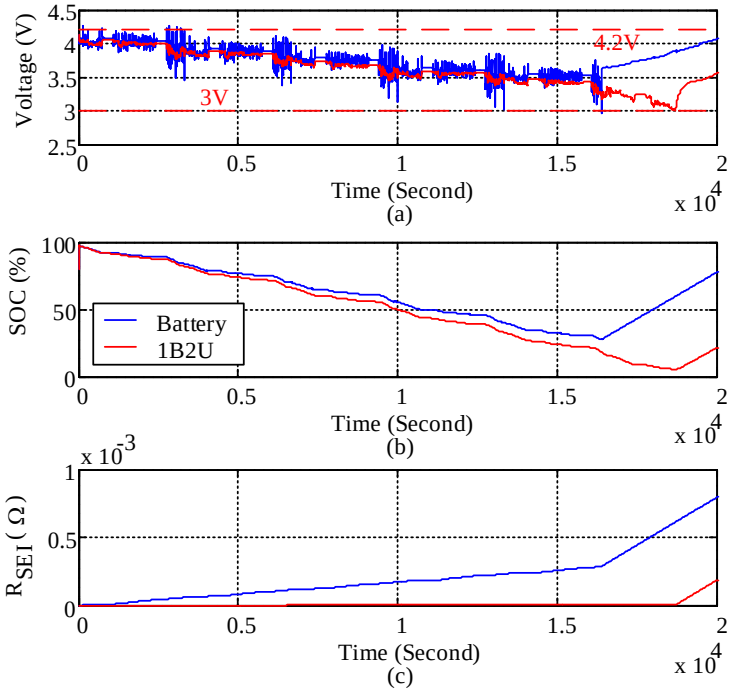

Figure 5.17: Comparison between 1B2U hybrid module and battery-only cell under driving cycles

overcharge and overdischarge from the high amplitude and high frequency pulses. The hybrid module has a wider operating SOC range because the smooth terminal voltage accepts it runs a longer distance until the terminal voltage of it achieves the cutoff voltage 3V. Moreover, SEI layer of the hybrid module grows slower than the battery-only cell from the SEI layer growth model as shown in Fig. 5.17(c).

To compare internal state variation of an aged hybrid module with battery and validate the SEI growth model based on the physics-based modeling, the 1B2U hybrid module and a battery cell are tested and aged. The experimental procedure is introduced in Fig 5.18. The battery cell and 1B2U hybrid module are discharged by a repeated 4 times HWY, UDDS, and US06 blend driving cycle. After the driving cycle, they are charged by a constant current constant voltage (CCCV) charging that the constant current is 1.5A, constant voltage is 4.2V, and cutoff current is 0.1A. The battery in the 1B2U hybrid module and the battery-only cell are discharged by a 3A constant current to measure battery cell's nominal capacity. The cutoff voltage is 2.5V. This procedure repeats 50 times until the cycle number reaches 100.

Fig. 5.19 shows the tested internal resistances of two cells which are respectively in the battery-only cell and 1B2U hybrid module at the 1st cycle and the 100th cycle. The tested internal resistances are fitted by numerical optimization under HPPC profile. The 100th cycle internal resistances are also compared with the physics-based models of the battery and hybrid module. It needs to note that the 100th cycle internal resistances of the physics-based models grow based on the tested internal resistances at the 1st cycle. Therefore, the shape of the 100th cycle internal resistances in the models are the same as the 1st cycle tested internal resistances. From the test results and simulation results, the battery-only cell has a higher internal resistance

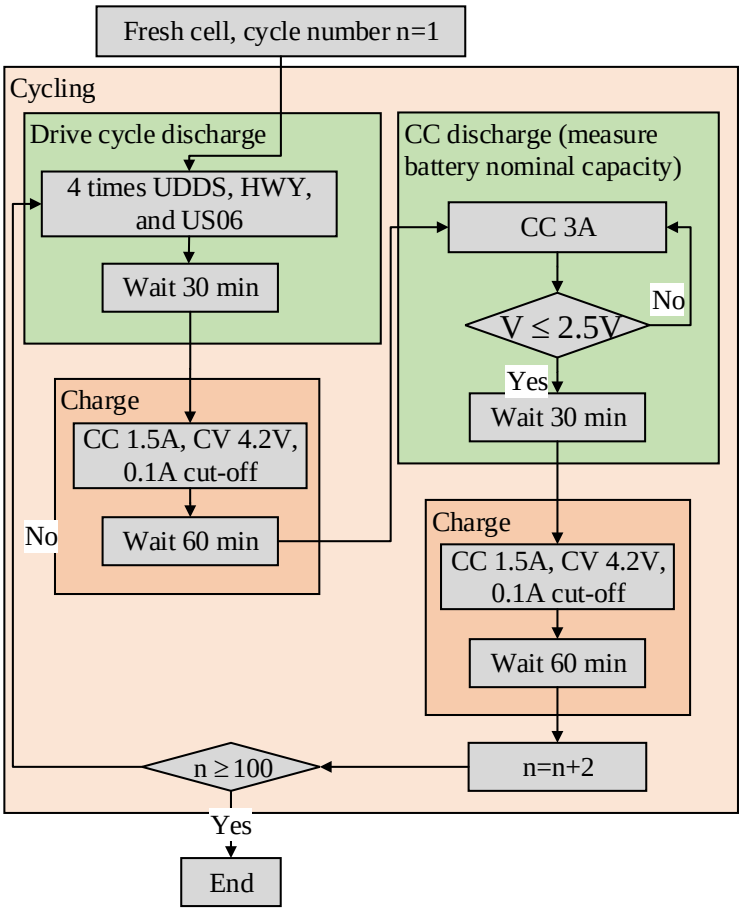

Figure 5.18: Experimental procedure

than the 1B2U module.

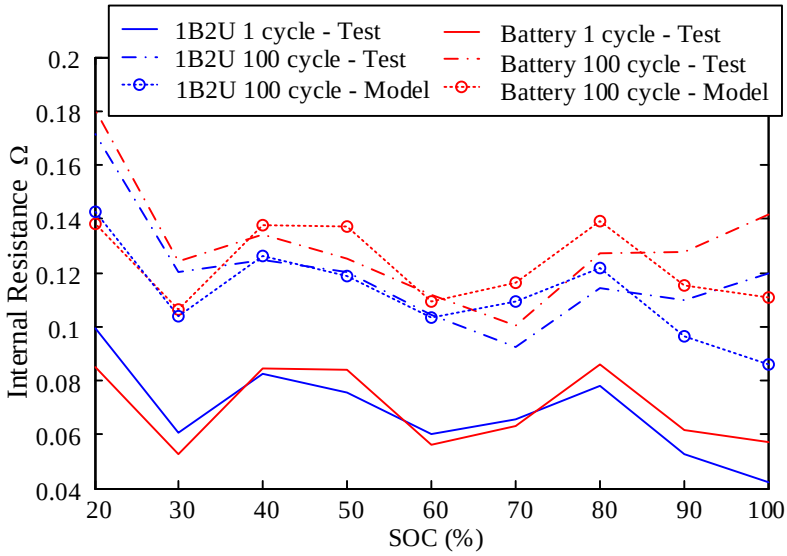

Figure 5.19: Internal resistance of fresh battery cell and 100 cycles aged battery cell

Fig. 5.20 compares the capacity fade between the battery-only cell and 1B2U module based on the test results and aging model. The aging model can follow the trend of capacity fade. The hybrid module can marginally postpone the aging process after the 100 cycles. In this figure, the aging models are projected to the 200th cycle. Results show that the capacity of the battery in the hybrid module at the 200th cycle equals to the capacity of the battery-only cell at the 145th cycle. The hybrid module prolongs 55 cycles after 200 cycles.

5.3.3 States Estimation for lithium-ion battery in hybrid module based on SPM

Estimation algorithm based on extended Kalmen filter (EKF) is developed to estimate SOC and SOH of the lithium-ion battery in a hybrid module. The SOC-SOH joint

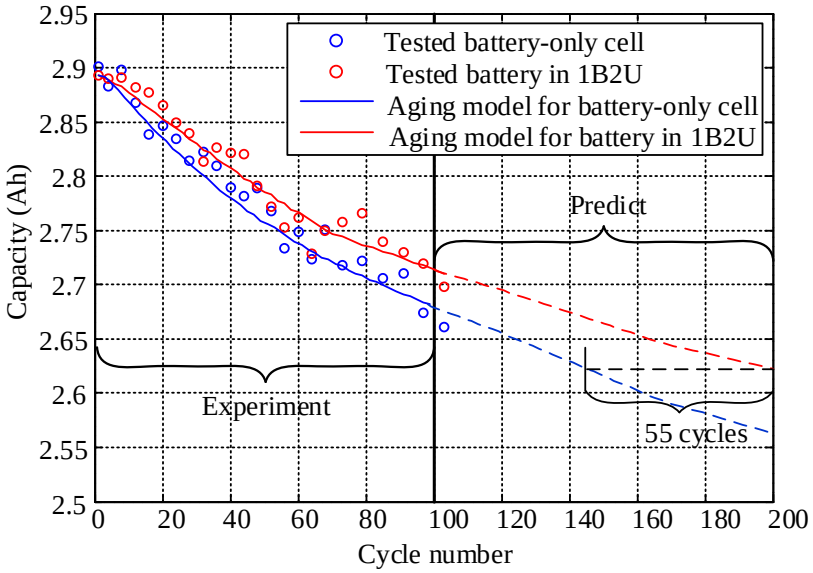

Figure 5.20: Cycle life characteristcs

estimation algorithm in (Gu *et al.*, 2016b) is applied to estimate states of batteries in the hybrid module. In this algorithm, the state vector consists of normalized lithium ion concentration of each shell of the positive electrode and the internal resistance R_f with respect to the magnitude of current and SOC.

$$\mathbf{x} = [SOC_p^1, \ldots, SOC_p^{M-1}, R_f]^T \tag{5.9}$$

From the first $M-1$ states, the SOC of the cell could be derived by (4.56).

However, the current that flows into the lithium-ion battery is unmeasurable. Currents I_k^{batt} and I_k^{uc} need to be determined by the bisection and interpolation algorithms as the hybrid module modeling in Fig. 5.7. This current I_k^{batt} and terminal voltage V_k become the input signal into the EKF algorithm. The flowchart of this

estimation algorithm is shown in Fig. 5.21. The ultracapacitors have a longer cycle life and more stable properties than the lithium-ion battery, therefore assuming parameters in ultracapacitors are known in the estimation algorithm.

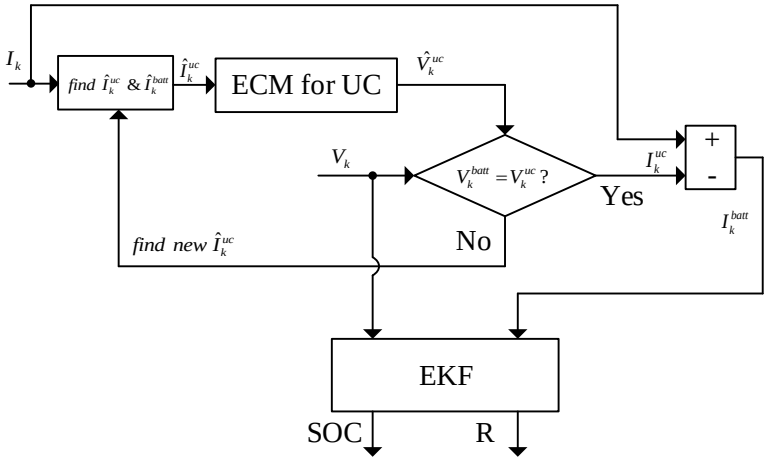

Figure 5.21: Flowchart of the SOC-SOH joint estimation for the lithium-ion battery in a direct couple hybrid module

The SOC-SOH joint estimator is validated by the 1B2U hybrid module experimental results. It is assumed that $M = 20$ shells in a solid phase spherical, therefore, state vector $\mathbf{x}$ includes 19 states for SOC estimation and 1 state for the internal resistance estimation. To validate the estimator, the initial SOC error is +5% and the initial internal resistance is 0.3Ω (around +100% error). Fig. 5.22 indicates that this EKF estimator can follow SOC and the internal resistance. The maximum SOC error is 1.18% after the estimator is convergence and the MAE of SOC is 0.24%. The maximum estimated resistance error is 0.0362Ω after the estimator is convergence and the MAE of the internal resistance is 0.0134Ω.

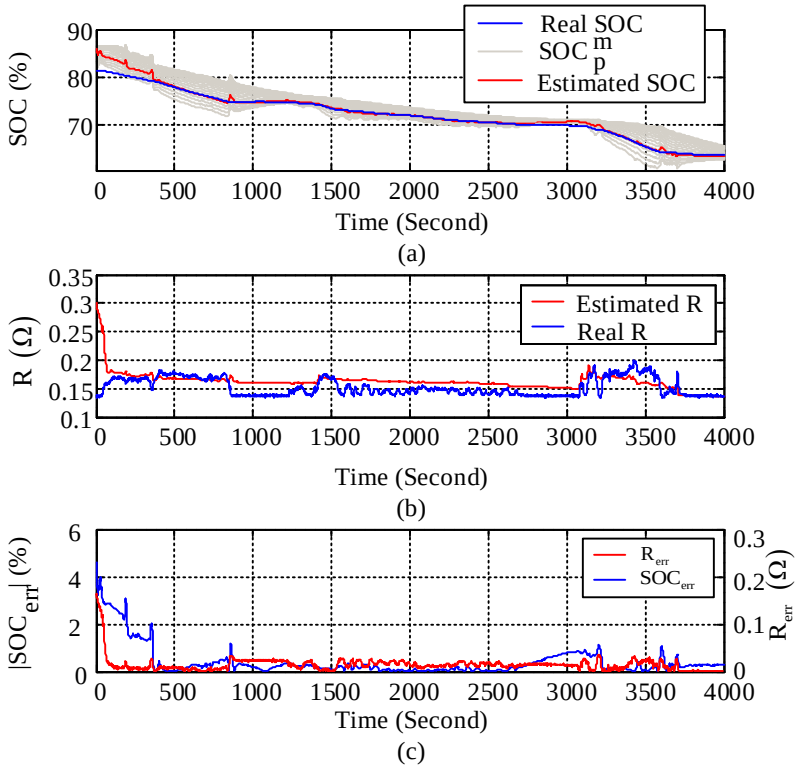

Figure 5.22: SOC and internal resistance estimation results (a) Estimated SOC, (b) Estimated internal resistance R_f, (c)SOC and R_f absolute error

5.4 Conclusions

To research the aging mechanisms in a lithium-ion battery cell, physics-based single particle model with SEI growth model was used. This model was applied to analyze the active hybrid energy storage system which focuses on hybridization at the cell level. This topology was simulated under UDDS, HWY and US06 driving cycles. From simulation results, the hybrid module slowed SEI growth under different conditions. However, the active hybrid module at the cell level is not suitable for a large energy storage system owing to the complicated topology.

A direct coupled hybrid energy storage module was proposed that employed ultracapacitors to improve the performance of the lithium-ion battery. Without power electronics between battery cells and ultracapacitor cells, the performance of the module could be enhanced by the number of battery cells and the number of ultracapacitor cells in series and in parallel. A single particle model with the bisection and interpolation algorithms was utilized to simulate the performance of the direct coupled hybrid module and validated by experimental results. A case study based on an 18650 lithium-ion battery cell and an ultracapacitor cell is presented. The direct coupled hybrid modules enable higher specific power than a single lithium-ion battery for short term pulses. The combination with ultracapacitor cells can smooth the terminal voltage, therefore, the hybrid module expands the SOC operating range of the battery in a fixed voltage operating range. Simulation and experimental results showed that the hybrid module can postpone aging effects of battery cells. Moreover, in order to estimate SOC and SOH of a battery cell in the hybrid module without additional current sensors, an SOC-SOH joint estimation algorithm embedded an optimization algorithm was proposed to calculate the current flows into a battery and

estimate the SOC and SOH of the battery.

Chapter 6

On the Design of a Direct Cell Coupled Hybrid Energy Storage System for Plug-in Hybrid Electric Vehicles and Mild Hybrid Electric Vehicles

6.1 Introduction

An energy storage system for an electrified vehicle needs to satisfy a multitude of performance requirements including power, energy, and cold start. Typically an energy storage system consists of hundreds, or even thousands, of battery cells. Aside from the performance of the energy storage system, cost, volume, weight, and aging

degradation are also important factors in the design. An optimum energy storage system should match performance targets over the design life and minimize cost, space, weight, and oversizing of the energy storage system (Bilgin *et al.*, 2015; Ostadi and Kazerani, 2014).

The focus of this chapter is the design, sizing, and comparative analysis of hypothetical hybrid energy storage system pack designs employing electrochemical battery cells direct coupled with ultracapacitor cells. A case study is performed using PHEV-40, power-assist HEV, and 48V HEV target requirements (USABC, 2002, 2014c,d) and a hybrid module design element concept that is composed of combinations of discrete battery and UC cells. Commercially available cells such as, an 18650 NCA lithium-ion battery cell and a non-aqueous, symmetric UC cell are used as unit-level design elements in the example case study. These design elements are put in as many as needed parallel and series combinations to satisfy design requirements.

The HESS pack design is motivated by exploring complementary benefits of using high-power capable UC cells with high energy dense battery cells. A thorough design requires experimental performance and power characterization of the HESS pack candidate to ascertain performance/cost targets and to facilitate pack sizing design. Since there are many ways to directly couple battery and UC cells, via many possible sizing ratios, and each combination has a different power/energy capability response, it is impractical to perform experimental characterization of every HESS pack design candidate. For a battery only design this is not an issue since it is sufficient to characterize a single cell and scale the resulting power/energy capability responses to extrapolate pack performance. However, the response of a direct coupled HESS pack depends not only on the individual battery/UC cell responses, but also on their

relative string ratios and combined impedances.

A simulation design approach is proposed that employs an equivalent circuit model of the battery cell, based on a full cell characterization over its operating range, and a model of the UC. Candidate HESS modules with selected battery/UC ratios are simulated to generate expected power/energy capability curves used in subsequent pack sizing design. A so-called maximum-energy-pulse (MEP) test procedure (Pei *et al.*, 2014) is employed for this purpose. Although there are other characterization procedures available such as dynamic stress test (Govindaraj *et al.*, 2010; Han *et al.*, 2014), hybrid pulse power characterization (Vellucci *et al.*, 2013), and others (He *et al.*, 2011; Pattipati *et al.*, 2011), the MEP test performs the test by operating at the extreme current and voltage limits. An additional cold cranking simulation test (USABC, 2014a) is also performed to verify the HESS pack design passes cold start requirements. The use of this HESS module simulation approach can find a smaller number optimal HESS design candidates that can be experimentally tested at latter stages of the pack design process. A step-by-step HESS pack design sizing approach is proposed and described in this chapter. The pack sizing design is based on a graphical approach proposed by USABC (USABC, 2014a). Multiple HESS pack designs are compared to a battery only design at different temperatures and using metrics such as minimum/maximum power, useable pack energy, cost, weight, and volume.

6.2 Cell and pack modeling

The equivalent circuit model depicted in Fig. 6.1 is used to model the battery cell (Emadi, 2014). Parameters for this model were obtained by fitting parameters from characterization tests on a single 18650 battery cell across various temperatures and state of charge operating points. The fitted ohmic (R_o) and dynamic (R_a,R_b,R_c) resistances of this cell are shown in Fig. 6.2. It is observed that resistance increase as a function of temperature and at lower SOC regions. Moreover, the open circuit voltage (V_{oc}) is a monotonic function of SOC that decreases as SOC decreases. These factors will limit the power capability of the cell at lower temperatures and at lower SOC operating points.

The UC is modeled as the simple equivalent circuit shown in Fig. 6.3. Parameters for this model can be obtained from the Maxwell datasheet (Maxwell, 2013). It is noted here that unlike battery cells, the UC resistance is fairly insensitive to large temperature variations. A Maxwell BCAP0310 is chosen because it has relatively higher power density and larger energy than other Maxwell UC cells; it is also similar in weight and cell cost to the 18650 cell. A comparison between the battery and UC cells used in the case study is shown Table 6.1. It is noted here that table values for the 18650 cell are based a separate commercially available Panasonic NCR18650A cell (Panasonic, 2012). The values and costs shown in Table 6.1 are for illustrative purposes only; the case study presented in this chapter focuses more on the relative differences/costs between the UC and battery in the context of comparisons between battery-only and HESS pack designs using combinations of unit design elements.

A hybrid energy storage system that combines batteries and ultracapacitors can be categorized into either passive or active HESS designs. A passive HESS design directly

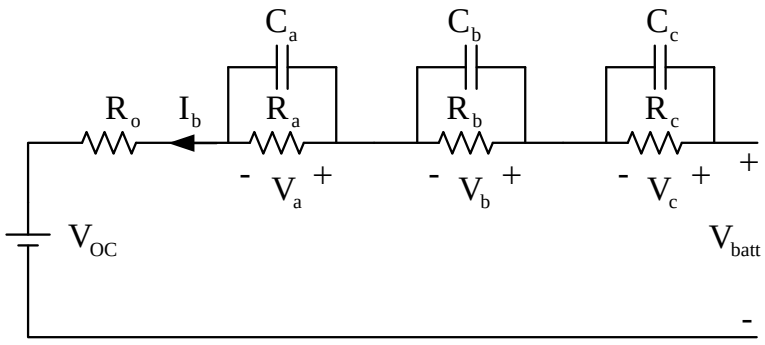

Figure 6.1: Battery cell equivalent circuit model

connects battery pack/cells and ultracapacitor pack/cells together without power-electronic circuits to split/control power flow. Active HESS topologies use a variety of power electronic circuits to improve performance. Generally, the performance of an active HESS is better than a passive HESS design, but this greatly increases hardware/software complexity and cost (Gu *et al.*, 2015b). The focus of this chapter is on direct cell/module coupled battery/UC passive HESS designs.

Table 6.1: Battery and UC cell specifications

	Max Voltage (V)	Cost ($)	Weight (g)	Volume (mL)	Energy (Wh)	Peak Power (W)
18650 Battery (Panasonic, 2012)	4.2	8 [1]	47.5	17.55	10.8	45
310F Ultracap (Maxwell, 2013)	2.7	7.6 [2]	60	53.56	0.31	400

[1] Cost of battery is from http://www.orbtronic.com.

[2] Cost of ultracapacitor is from http://www.mouser.com.

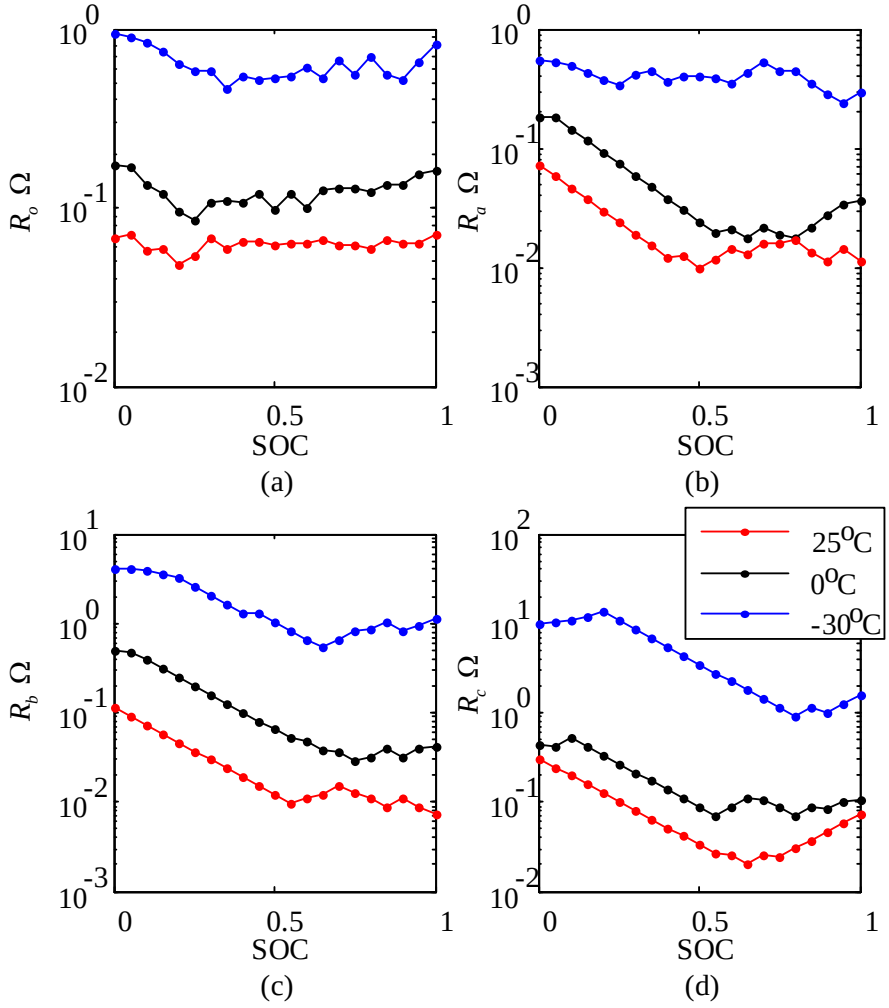

Figure 6.2: Fitted 18650-cell resistances (a) R_o, (b) R_a, (c) R_b, (d) R_c

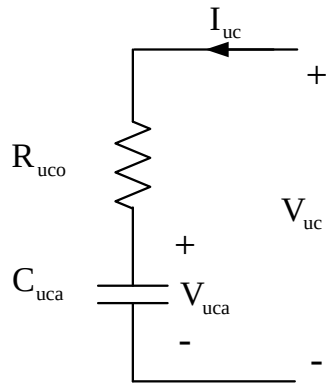

Figure 6.3: Ultracapacitor cell equivalent circuit model

A practical pack design requires cell balancing circuitry to compensate for cell-to-cell variations. A simplified case study is performed in this chapter by neglecting cell balancing hardware and cell-to-cell variations and focuses only on the energy storage elements.

The HESS pack structure is depicted in Fig. 6.4. N_{hybrid}^{series} represents the number of hybrid modules in series, and $N_{hybrid}^{parallel}$ represents the number of hybrid module branches/strings in parallel. There are multiple design possibilities for the hybrid module. For a battery only pack the hybrid module is a battery cell. Another simple approach is that the hybrid module is one battery cell direct coupled to one UC cell in a parallel fashion as shown in Fig. 6.5a); this approach can share the same balancing hardware. The most general approach is shown in Fig. 6.5b) where $N_{Batt}^{parallel}$ represents the number of battery branches, $N_{UC}^{parallel}$ represents the number of UC branches, N_{Batt}^{series} represents the number of battery cells in series, and N_{UC}^{series} represents the number of UC in series. Unequal values for the number of UC/battery cells in series may be necessitated to match voltage ranges of the cells. In these

topologies the battery and UC models depicted in Fig. 6.1 and Fig. 6.3 are employed.

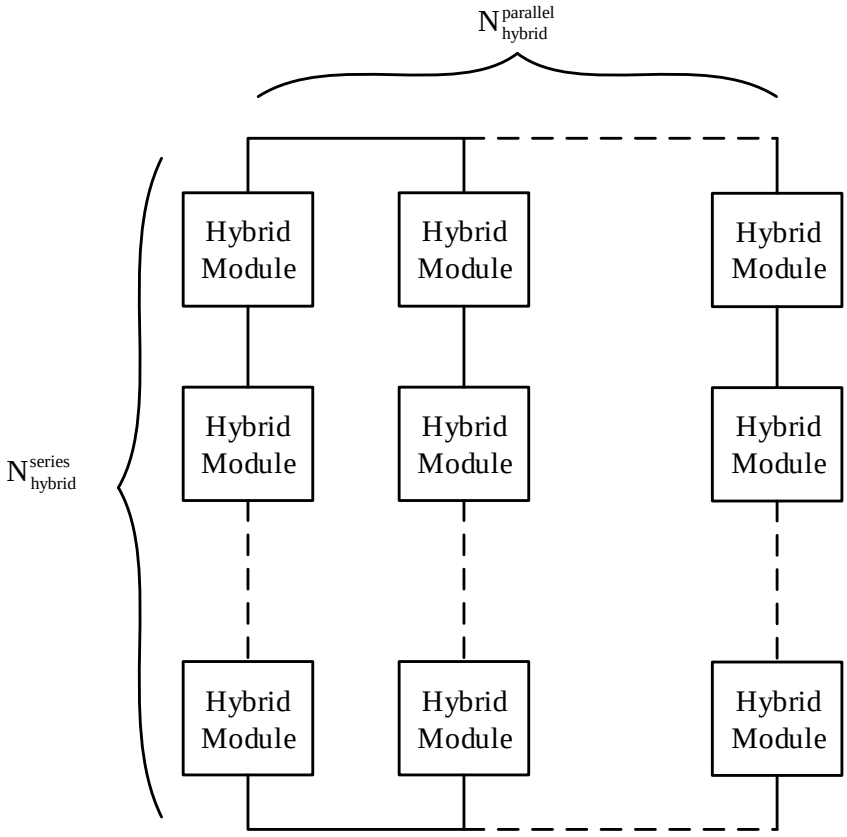

Figure 6.4: Hybrid energy storage system pack topology

6.3 Test procedures and design criteria

6.3.1 Maximum Energy Pulse Test Characterization

A power characterization test procedure employing MEPs of fixed duration is employed to generate power capability curves. An MEP is a combination of a constant current and constant voltage pulse. The maximum current allowed at the chosen

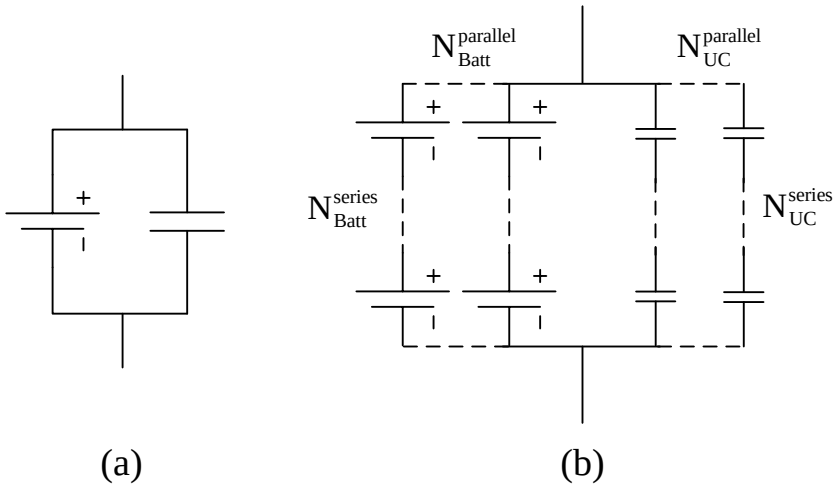

Figure 6.5: Hybrid module topologies, (a) simplest case, (b) general case

operating point is used until a voltage-limit is reached, then for the remaining duration of the pulse the voltage is held constant. This operates the battery at the extremes for the duration of the MEP and the resulting integrated energy is at its maximum. A common alternative test procedure is a hybrid pulse power characterization test (USABC, 2014a); it employs carefully chosen constant current pulses meant to get close to, but not hit or exceed, the voltage limit by the end of the pulse. HPPC based characterization inevitably involves guesswork in the choice of current magnitude and number of current magnitudes to test to assess maximum power and current dependency.

The MEP test procedure employs discharge and charge pulses at many SOC and temperature operating points. An example profile is depicted in Fig. 6.6. The MEP test method can provide a direct conservative measure of peak power availability while also providing system excitation at varying current magnitudes. Power capability of

discharge/charge can be directly obtained using the last point of each pulse, depicted as stars in the power vs time curve in Fig. 6.6. The pulse voltage and current profile are also used to fit equivalent circuit model parameters such as resistances. This procedure is employed via simulation on many hybrid module design candidates to generate power capability curves used later in the pack design process.

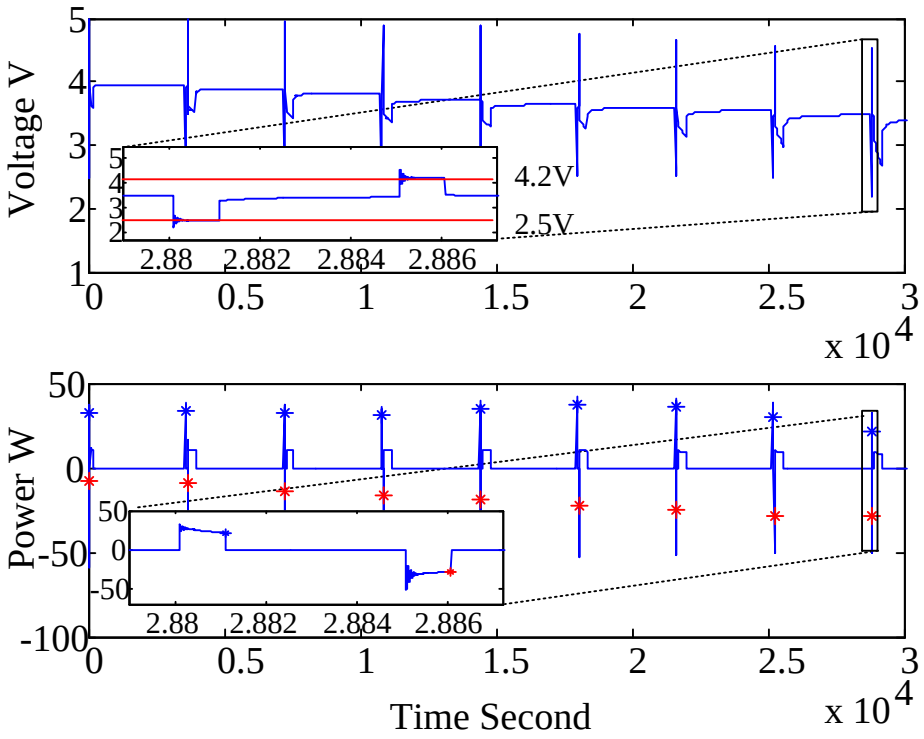

Figure 6.6: Example MEP test profile. The stars indicate the points used to report power capability

6.3.2 Power Capability vs Removed Energy Criteria

The results of the MEP test are used to generate hybrid module power capability vs removed energy graphs used for pack sizing design employing a graph-analytical method as described in (USABC, 2003, 2014a). For an energy storage system in a

PHEV, peak pulse power capability and available energy for charge depleting and charge sustaining modes are important metrics. Compare with an energy storage system in a PHEV, an energy storage system in a mild HEV does not have an all-electric mode, therefore, the target for the available energy is more straightforward. In this subsection, the graph-analytical method for PHEV is introduced as an example which can be extended to design an energy storage system in a HEV.

Energy storage system performance targets for PHEV-40 are shown in Table 6.2.

Table 6.2: PHEV-40 Performance Target (USABC, 2014d)

Characteristics	Units	Values
all-electric range (AER)	Miles	40
Discharge Pulse Power (10 sec)	kW	38
Discharge Pulse Power (2 sec)	kW	46
Regen Pulse Power (10 sec)	kW	25
Available Energy for CD Mode	kWh	11.6
Available Energy for CS mode	kWh	0.3
Maximum Operating Voltage	V	420
Minimum Operating Voltage	V	153

To describe the pack design criteria an illustrative example case considering only a battery cell as the unit hybrid module design element is described here. The concept of a scaling factor denoted as the battery size factor (BSF) is employed to relate cell (or hybrid module) quantities to pack level quantities, i.e.

$$Power_{requirement}^{module} = \frac{Power_{requirement}^{pack}}{BSF} \tag{6.1}$$

A candidate BSF value is first selected and used to draw power and energy lines on the cell (or hybrid module) power capability vs removed energy curve. An example

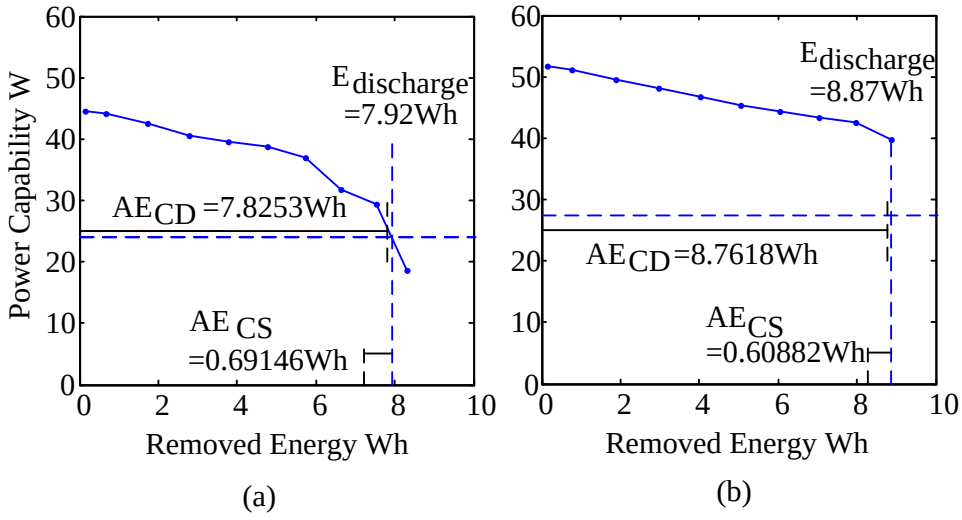

Figure 6.7: 10-sec power capability vs removed energy for a) single battery cell with BSF=16x99, b) hybrid module with $N_{batt}^{series} = N_{batt}^{parallel} = N_{UC}^{parallel} = 1, N_{UC}^{series} = 2$, and BSF= 14x99

is depicted in Fig. 6.7a) where for clarity only 10-second discharge power at 25^oC is drawn as the solid curve. A horizontal dashed line is then drawn to represent the 10-sec power requirement scaled down to the cell level using the BSF. An intersecting vertical dashed line is then drawn to denote the usable discharge energy $E_{discharge}$. The removed energy to the right of the $E_{discharge}$ line indicates unusable cell energy that represents an energy oversize in the pack design for the chosen BSF. Energy regions to the left indicate available energy for charge depleting (CD) and charge sustaining (CS) modes, they are calculated as

$$\begin{aligned} AE_{CD} &= E_{discharge} - \tfrac{1}{2}AE_{CS}^{target} \\ AE_{CS} &= E_{discharge} - (AE_{CD}^{target} - \tfrac{1}{2}AE_{CS}^{target}) \end{aligned} \tag{6.2}$$

where AE_{CD} and AE_{CS} are available energy for CD and CS modes, respectively, and

AE_{CD}^{target} and AE_{CS}^{target} are target energy requirement values scaled down from Table 6.2 using the BSF. The example in Fig. 6.7a) uses BSF=16x99, where 99 was initially selected to be close to the maximum voltage requirement. Given this number of cells in series, a minimum number of parallel strings is determined by checking power and energy requirements using the graph-analytic method for different values of $N_{hybrid}^{parallel}$. In this example a minimum of 16 parallel battery cell strings is needed to satisfy the pack power and energy requirements stated in Table 6.2. It is noted here that the USABC PHEV graph-analytical pack design method states that only a 25^oC power-capability vs removed energy curve is to be used for pack sizing design. This implies an expected battery operating temperature at room temperature. It can be argued that this is achievable in practice by employing a battery thermal management system and exploiting cell self-heating to ensure that most of the time the battery is close to room temperature during operation. Even in extremely cold climates the battery can be raised from -20^oC to 25^oC in as little as 15 minutes via thermal management and cell self-heating. However, for short trips and for systems employing weak or no battery heating the design must be repeated considering a more reasonable lower temperature bound. Repeating the graph-analytical pack design process using 0^oC power-capability vs removed energy curves and the 0^oC cell resistance in Fig. 6.2 yields required BSF=22x99, the additional parallel strings can be viewed as the needed battery oversize to compensate for power-loss and resistance-increase of the battery cell at lower temperatures.

6.3.3 Cold Cranking Criteria

Another important performance requirement of a PHEV pack is cold cranking power. This cold cranking test involves three steps (USABC, 2014a):

- Step 1: From a fully charged pack remove $AE_{CD}^{target} + \frac{1}{2}AE_{CS}^{target}$ of energy at 25^oC.
- Step 2: Reduce the ambient temperature to -30^oC and rest the battery to make sure it reaches thermal equilibrium.
- Step 3: Discharge pack with three 2 second 7kW constant power pulses.

The passing criteria is such that the terminal battery cell voltages cannot be lower than some defined level, e.g. 2.5 V, to avoid cell damage and abuse during Step 3. A simulated cold cranking test using the battery model in Fig. 1 and resistances in Fig. 6.2 is performed on the candidate 25^oC based pack design of BSF=16x99. The response is depicted in Fig. 6.8a) where the red line is the minimum allowed cell voltage, it is observed this design cannot meet cold cranking requirements. A modified pack design of BSF=18x99 is shown in Fig. 6.8b) to satisfy cold cranking.

In the remainder of the chapter two battery cell only pack designs will be used as benchmarks to compare against HESS pack designs. The first is denoted as the USABC design, it is based on 25^oC power capability vs removed energy criteria and -30^oC cold cranking; it results in BSF=18x99. The second is denoted as the cold-temperature design, it is based on 0^oC power capability vs removed energy criteria and -30^oC cold cranking; it results in BSF=22x99.

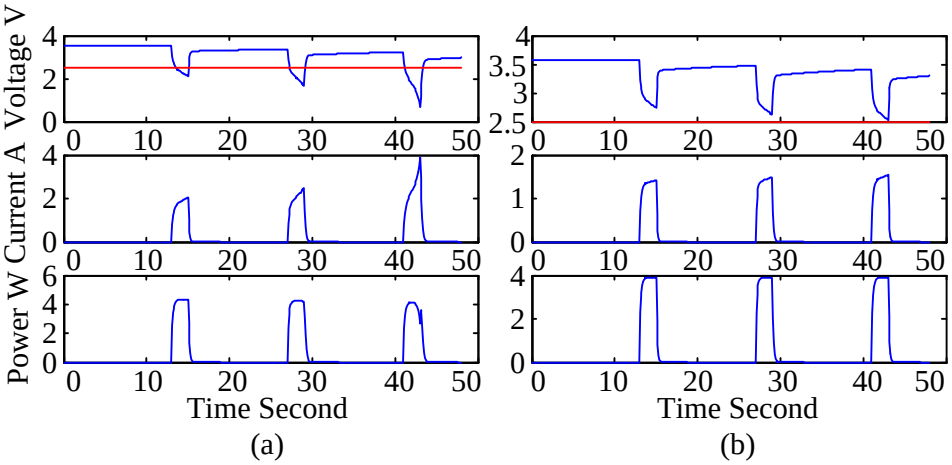

Figure 6.8: Cold cranking test profiles, (a) battery cell only with $BSF = 16 \times 99$, (b) battery cell only with $BSF = 18 \times 99$.

6.4 Comparative HESS Pack Analysis

A simple direct coupled HESS pack design involves coupling at the battery cell level. Considering the cells in Table 6.1, two UCs in series need to be used to connect to a single battery cell. The resulting power capability of the hybrid cell unit is shown in Fig. 6.7b) where there is a reduction in battery cells in pack design to 14x99 and an increase in power. However, the resulting pack energy storage cost more than doubles and the energy utilization of the UC is only 33% due to limited voltage range. An alternative pack design is proposed here based on a hybrid module design unit concept. The design steps are as follows:

1. Match battery/UC voltages at module level to determine N_{batt}^{series} and N_{UC}^{series}.

2. Determine $N_{hybrid^{s}eries}$ based on pack voltage requirement. Initialize $N_{hybrid}^{parallel}$=0.

3. Define unit hybrid module design candidate by assigning values for $N_{batt}^{parallel}$ and $N_{UC}^{parallel}$.

4. Define standard operating temperature.

5. Obtain power capability curves of HESS module candidate via Maximum Energy Pulse simulation

6. Increment $N_{hybrid}^{parallel}$ by one

7. Check if power/energy requirements satisfied by graphical design procedure on power capability curves, if it fail then go to Step 6

8. Check cold cranking simulation, if cold cranking requirement fails then go to step 6

9. Report $N_{hybrid}^{parallel}$

6.4.1 PHEV-40

Using the above methodology, Step 1 yields optimal values of N_{batt}^{series}=9 and N_{UC}^{series}=14. This results in near optimal UC energy utilization of 65%. For step 2 the maximum pack voltage requirement in Table 6.2 is used and results in N_{hybrid}^{series}=11. Many hybrid module design candidates were considered by sweeping ranges of $N_{batt}^{parallel}$ from 1 to 20 and $N_{UC}^{parallel}$ from 1 to 5. Standard operating temperatures of 25^oC (USABC design) and 0^oC (cold temperature design) were used. In total 200 combinations and repetitions of the proposed HESS pack design process were performed. The required numbers of $N_{hybrid}^{parallel}$ hybrid modules for a requirement passing HESS pack design are given in Table 6.3 and Table 6.4.

A select number of leading HESS pack design candidates are explored by comparing them in Fig. 6.9 and Fig. 6.10 on the following metrics: relative cost, weight, volume, usable/unusable energy, 2/10 second power, and power-to-cost ratio. The battery/UC parallel string ratios are calculated as $N_{hybrid}^{parallel} \times N_{batt}^{parallel} - N_{hybrid}^{parallel} \times N_{UC}^{parallel}$, e.g. the hybrid module design of $N_{batt}^{parallel}$=2 and $N_{UC}^{parallel}$=1 in Table 6.3 corresponds to 14-7 in Fig. 6.9. It is noted here the red dashed lines in Fig. 6.9 and Fig. 6.10 represent power/energy requirements from Table II. The unusable energy in Fig. 6.9 d) and Fig. 6.10 d) represent a low SOC operating region of the pack that cannot provide enough discharge power, its size reflects a type of pack over-design. The power subplots in Fig. 6.9 e)f)h)i) and Fig. 6.10 e)f)h)i) indicate the power range over an operating window that corresponds to the usable energy range of the pack. The size between maximum power and minimum power in these plots illustrate another kind of pack over-design.

From Fig. 6.9 it is seen there exist replacement tradeoffs that can marginally reduce cost and keep weight approximately the same. The leading designs are HESS packs with battery/UC parallel string ratios of 16-1 and 15-2; these show greater power-to-cost ratio in Fig. 6.9 g) and better energy utilization in Fig. 6.9 d) compared to a battery only design using 18 parallel strings. In this example the UC strings are able to offset the oversize that resulted from meeting cold-cranking requirements described in Section III-C. Although cold-cranking at -30^oC has been considered in the designs in Fig. 6.9, cold temperature performance of these packs at 0^oC is shown to not satisfy requirements in Fig. 6.9 h) and Fig. 6.9 i). This illustrates the need to thermally management the pack to operate at or near room temperature. When the cold-temperature pack design method is used, the battery only design results in

large pack energy oversize, as seen in Fig. 6.10 d), to compensate for the increased battery resistance. In Fig. 6.10 it is seen a significant number of UC strings are required to replace just a single battery string. The limiting design factor for this case study is the 10-sec power requirement. Due to the low energy content of UC cells (more than 25x less than the 18650-cell) the studied HESS pack designs have limited ability to improve 10 sec power. On the other hand 2-sec power is greatly enhanced via hybridization. The leading cold-temperature HESS pack design candidates are also significantly greater in terms of relative cost, weight, and volume. If UC cell technology is improved such that targets of 1/3 cost, 1/3 weight, and 1/8 volume are achieved then HESS pack designs start to be more attractive for PHEV applications; this is illustrated by noting the UC_{Target} metrics in Fig. 6.10 a)-c).

Table 6.3: $N_{hybrid}^{parallel}$ of a passive HESS has $N_{hybrid}^{series} = 11$ for 25^oC system

$N_{UC}^p \backslash N_{Batt}^p$	1	2	3	4	5	6	7	8	9	10	11	12	13	14	15	16	17	18	19	20
1	14	7	5	4	3	3	3	2	2	2	2	2	2	2	2	1	1	1	1	1
2	13	7	5	4	3	3	3	2	2	2	2	2	2	2	1	1	1	1	1	1
3	13	7	5	4	3	3	3	2	2	2	2	2	2	2	1	1	1	1	1	1
4	12	7	5	4	3	3	2	2	2	2	2	2	2	2	1	1	1	1	1	1
5	12	7	5	4	3	3	2	2	2	2	2	2	2	2	1	1	1	1	1	1

Table 6.4: $N_{hybrid}^{parallel}$ of a passive HESS has $N_{hybrid}^{series} = 11$ for 0^oC system

$N_{UC}^p \backslash N_{Batt}^p$	1	2	3	4	5	6	7	8	9	10	11	12	13	14	15	16	17	18	19	20
1	15	10	7	6	5	4	4	3	3	3	2	2	2	2	2	2	2	2	2	2
2	14	8	6	5	4	4	4	3	3	3	2	2	2	2	2	2	2	2	2	2
3	13	7	5	4	4	4	3	3	3	3	2	2	2	2	2	2	2	2	2	2
4	13	7	5	4	4	3	3	3	3	2	2	2	2	2	2	2	2	2	2	2
5	12	7	5	4	3	3	3	2	2	2	2	2	2	2	2	2	2	2	2	2

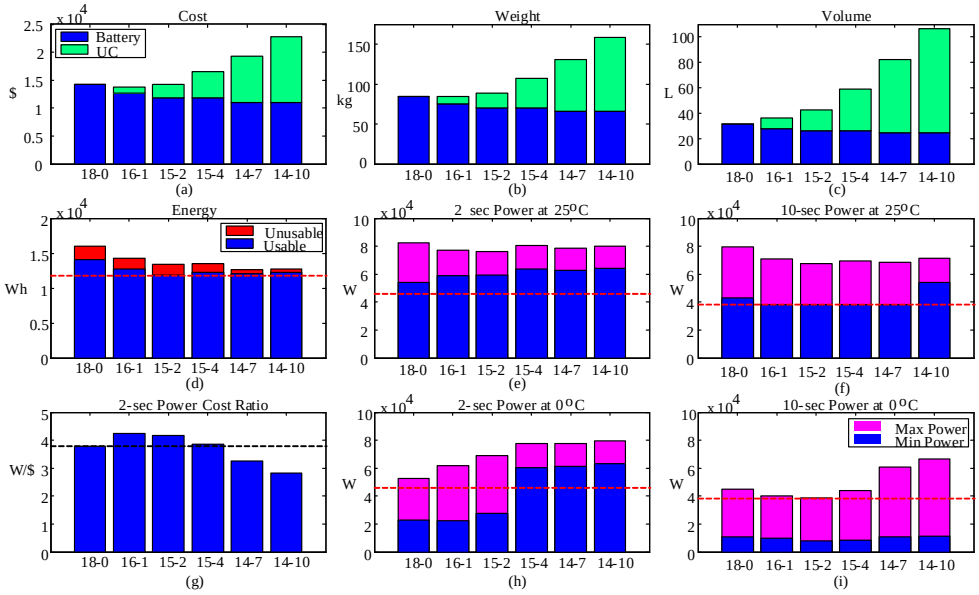

Figure 6.9: Comparison of pack designs based on USABC design guidelines, the x-axis states the ratio of battery strings in parallel with UC strings.

6.4.2 HEV

Energy storage system performance targets for the power-assist and 48V mild HEV are shown in Table 6.5.

The above design methodology can be also used to design an energy storage system in a mild HEV. The main different is that the mild HEV just needs to satisfy one total available energy target when the PHEV needs to satisfy the available energy targets for CD and CS modes in (6.2). The total available energy is calculated as

$$AE = E_{discharge} - E_{regen} \tag{6.3}$$

Similar to $E_{discharge}$ in Fig. 6.7, the usable discharge energy $E_{discharge}$ and usable regenerative energy E_{regen} for a HEV can be obtained from the power capability vs

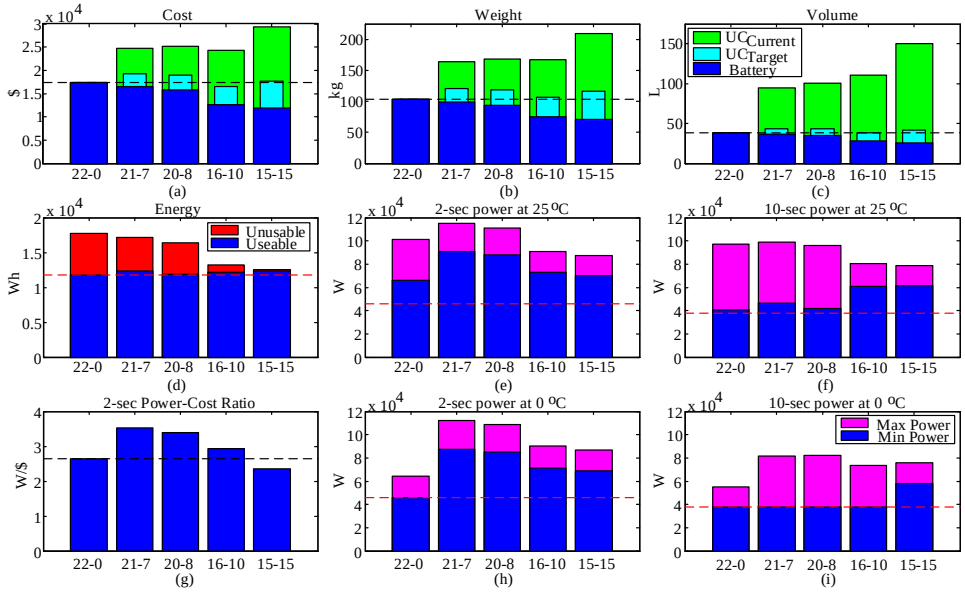

Figure 6.10: Comparison of pack designs based on cold temperature design, the x-axis states the ratio of battery strings in parallel with UC strings.

Table 6.5: Power-assist and 48V Mild HEV Performance Targets (USABC, 2002, 2014c)

Characteristics	Units	Power-assist (Max)	48V
Discharge Pulse Power	kW	40 (10 sec)	9 (10 sec)
Regen Pulse Power	kW	35 (10 sec)	11 (5 sec)
Total available Energy (over DOD range where power goals are met)	kWh	0.5	0.105
Maximum Operating Voltage	V	400	52
Minimum Operating Voltage	V	220	26

removed energy curves.

- Power-assist HEV (Max)

  Fig. 6.11 shows the 10 second regenerative/discharge power capability vs removed energy curves for a single battery cell and a selected hybrid module for the power-assist mild HEV. The solid red lines are the regenerative power capability curves and the solid blue lines are the discharge power capability curves. The red and blue horizontal dashed lines represent the regenerative and discharge power requirements scaled down to the cell level using the BSF respectively. The removed energy of the intersection of the solid and dashed blue lines represents $E_{discharge}$. E_{regen} can be obtained by the intersection of the solid and dashed red lines. The total available energy is limited by the regenerative and discharge power requirements as the arrow lines marked in this figure. If a cell works out of the range, it cannot meet the discharge/regenerative power targets. Fig. 6.11 (a) depicts that if a power-assist system just uses battery cells, the BSF is 12×90 and only a small portion of energy is utilized. The hybrid module example in Fig. 6.11 (b) increases the energy utilization of the entire system by using more ultracapacitors and less batteries.

  Step 1 in the design methodology for the power-assist mild HEV is similar to Step 1 for the PHEV-40 design, the optimal values of N_{batt}^{series} and N_{UC}^{series} are 9 and 14 which can use 65% energy of UC. To match the operating voltage range in Step 2, $N_{hybrid}^{series} = 10$ was selected. The hybrid module design candidates by sweeping range of $N_{batt}^{parallel}$ from 1 to 20 and $N_{UC}^{parallel}$ from 1 to 5 were also considered. For the mild HEV design, standard operating temperatures of 25^oC were used. The power capability curves of total 100 HESS module candidates

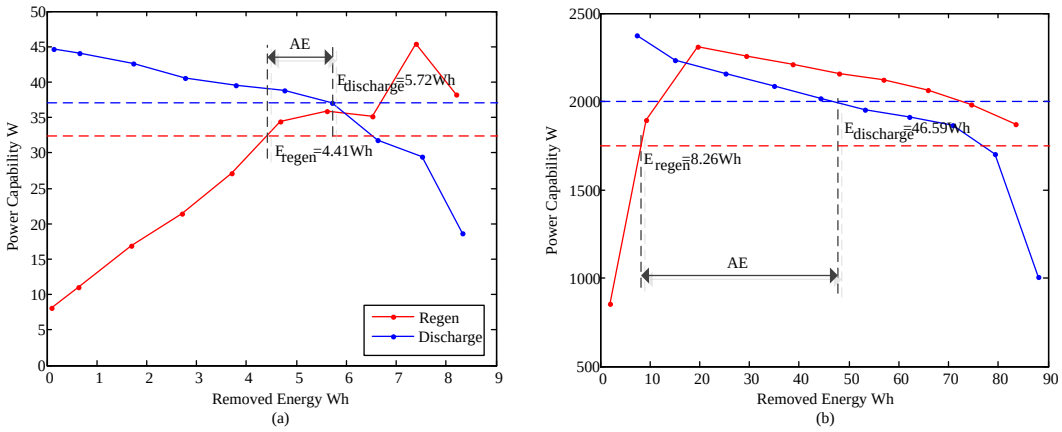

Figure 6.11: 10-sec power capability vs removed energy for a) single battery cell with BSF=12x90, b) hybrid module with $N_{batt}^{series} = 9, N_{batt}^{parallel} = 1, N_{UC}^{parallel} = 14, N_{UC}^{series} = 4$, and BSF= 2x10

via MEP simulation were obtained and used to derive the number of hybrid modules in parallel $N_{hybrid}^{parallel}$ which were shown in Table 6.6.

Table 6.6: $N_{hybrid}^{parallel}$ of a passive HESS has $N_{hybrid}^{series} = 11$ for power-assist mild HEV 25^oC system

$N_{UC}^p \backslash N_{Batt}^p$	1	2	3	4	5	6	7	8	9	10	11	12	13	14	15	16	17	18	19	20
1	6	5	4	4	3	3	2	2	2	2	1	1	1	1	1	1	1	1	1	1
2	4	4	3	3	2	2	2	2	2	2	1	1	1	1	1	1	1	1	1	1
3	3	3	3	2	2	2	2	2	2	2	1	1	1	1	1	1	1	1	1	1
4	2	2	2	2	2	2	2	2	2	1	1	1	1	1	1	1	1	1	1	1
5	2	2	2	2	2	2	2	2	1	1	1	1	1	1	1	1	1	1	1	1

Fig. 6.12 compares a select number of leading HESS pack design candidates for power-assist mild HEV on the following metrics: relative cost, weight, volume, usable/unusable energy, 10-second discharge power, and 10-second regenerative power. The energy requirement of HEV is different with the requirements of PHEV, the usable energy range in the total energy and utilization ratio are

shown in Fig. 6.12 (d). The 10 second discharge and regenerative power capability are shown in Fig. 6.12 (e) and (f). The HESS pack with battery/UC parallel string ratio of 2-8 is a leading design which spends similar price to the battery pack and has a higher energy utilization ratio and higher power capability.

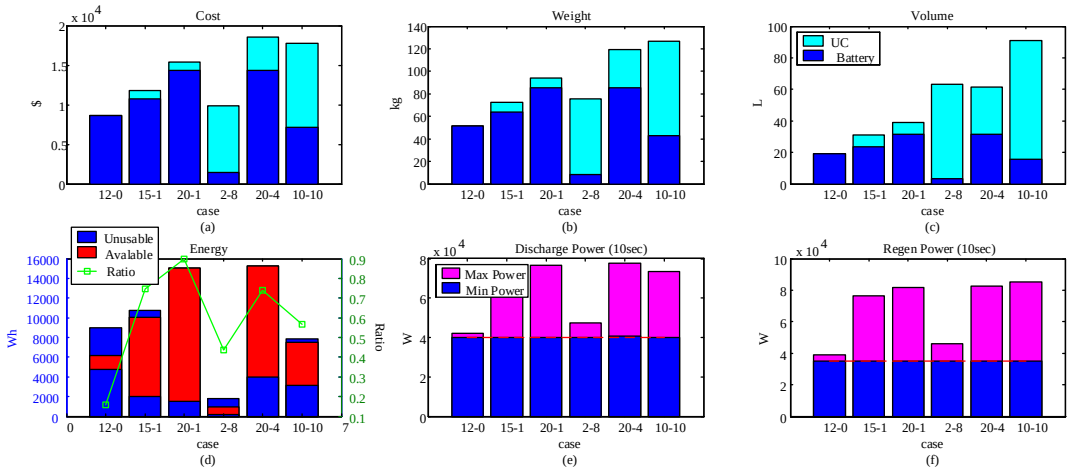

Figure 6.12: Comparison of pack designs based on FreeCAR power-assist design guidelines, the x-axis states the ratio of battery strings in parallel with UC strings.

- 48V mild HEV

  For the 48V mild HEV, the 5-second regenerative/ 10-second discharge power capability vs removed energy curves for a single battery cell and a selected hybrid module are shown in Fig. 6.13. Due to the low voltage requirement, $N_{batt}^{series} = 12$ and $N_{UC}^{sereis} = 18$ are selected. Fig. 6.13 (a) indicates that if a 48V system just uses battery cells, the BSF is 24×12 and only a small portion of energy is utilized. The hybrid module example in Fig. 6.13 (b) can also increase the energy utilization of the entire system by direct coupling ultracapacitors and

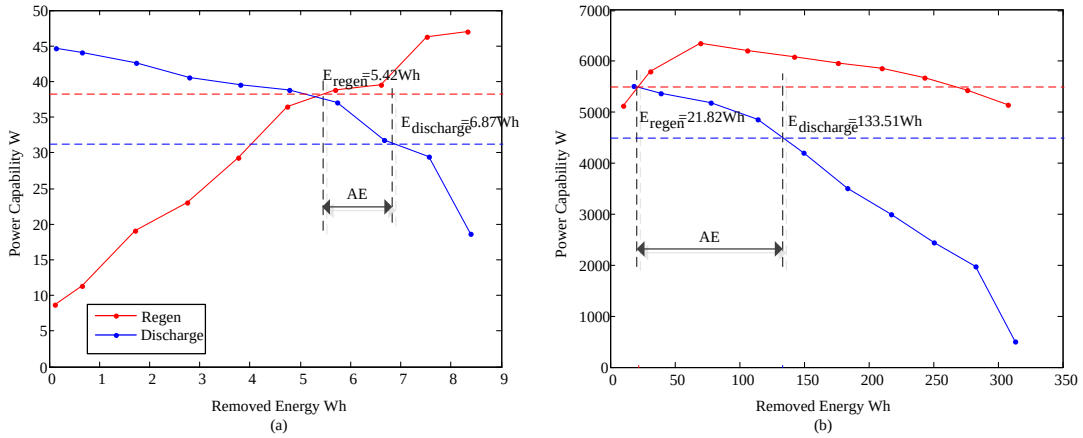

Figure 6.13: 10-sec discharge/5-sec regen power capability vs removed energy for a) single battery cell with BSF=24x12, b) hybrid module with $N_{batt}^{series} = 12, N_{batt}^{parallel} = 3, N_{UC}^{parallel} = 5, N_{UC}^{series} = 18$, and BSF= 2x1

batteries. Table 6.7 shows the derived number of hybrid modules in parallel for the 100 HESS module candidates.

Table 6.7: $N_{hybrid}^{parallel}$ of a passive HESS has $N_{hybrid}^{series} = 1$ for 48V mild HEV 25^oC system

$N_{UC}^p \backslash N_{Batt}^p$	1	2	3	4	5	6	7	8	9	10	11	12	13	14	15	16	17	18	19	20
1	10	9	7	6	5	4	4	3	3	2	2	2	2	2	2	2	2	2	2	2
2	10	6	5	5	4	3	3	3	2	2	2	2	2	2	2	2	2	2	2	2
3	7	4	4	3	3	3	3	3	2	2	2	2	2	2	2	2	2	2	2	2
4	5	3	3	3	3	3	3	3	2	2	2	2	2	2	2	2	2	2	1	1
5	4	3	2	2	2	2	2	2	2	2	2	2	2	2	2	2	2	2	1	1

Fig. 6.14 compares a select number of leading HESS pack design candidates for 48V mild HEV on the same metrics to the power-assist system. HESS packs with battery/UC parallel strings ratios of 10-20 and 36-20 have high energy utilization ratio and high power capability. However, these two candidates sacrifice price, weight, and volume. The design candidates with the ratio of 6-10 and 8-10 have better performance on power/energy capabilities without

much high price, weight, and volume, especially the 6-10 case is cheaper than the battery pack design.

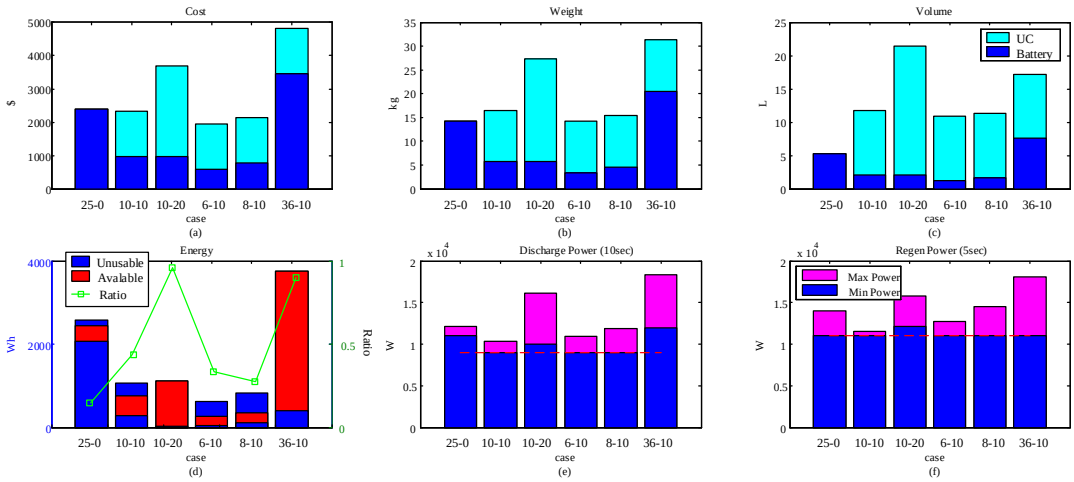

Figure 6.14: Comparison of pack designs based on 48V HEV design guidelines, the x-axis states the ratio of battery strings in parallel with UC strings.

6.5 Comparative analysis of the battery pack and HESS pack in PHEV-40 under driving cycles

From Table 6.3 and Fig. 6.9, using 16-1 HESS pack enables the energy storage system meets the requirements of PHEV-40, reduces cost, and relieves the oversize factor. The dynamic performance of the 16-1 HESS pack and 18-0 battery pack with fresh and aged battery cells are analyzed under UDDS and HWY driving cycles based on simulation in terms of voltage, SOC, distance, and energy. The battery and HESS packs are discharged from 95% SOC. The lower SOC limit and voltage limit are respectively set as 10% and 250V. Once SOCs or terminal voltages of batteries

achieve the limits, the tests are finished.

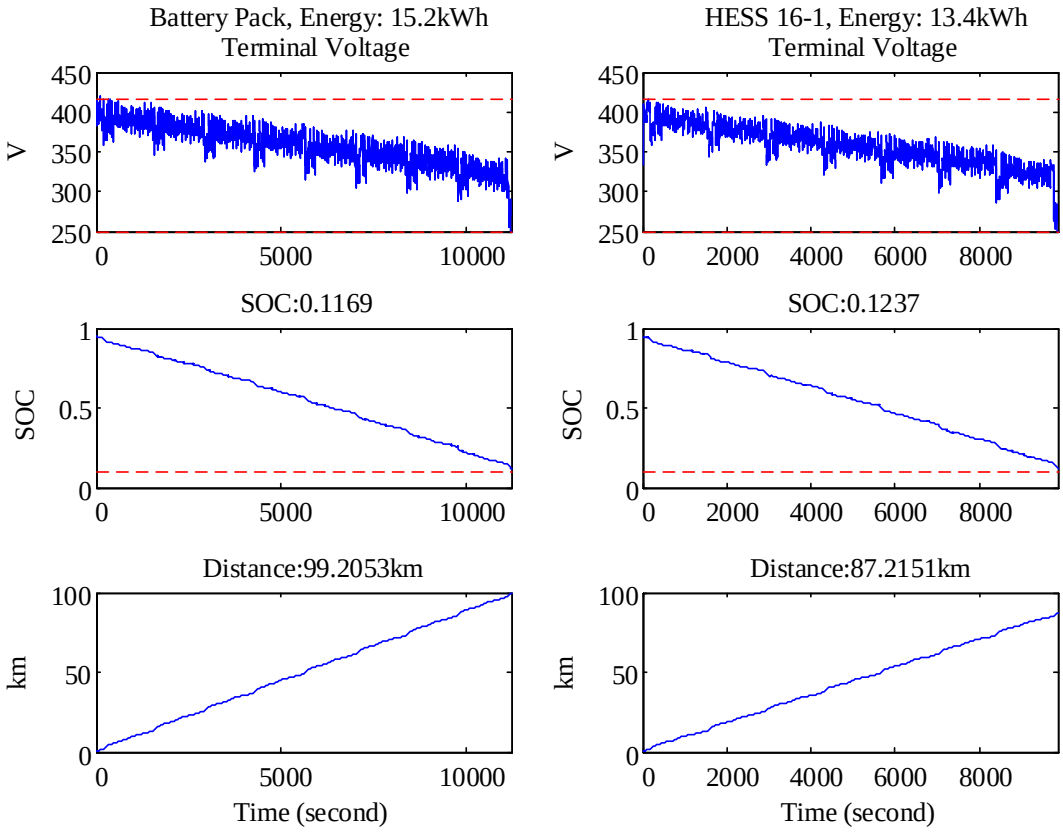

Figure 6.15: Results of 18-0 battery pack and 16-1 HESS pack with fresh battery cells under UDDS driving cycle

Fig. 6.15 and Fig. 6.16 show the test results for fresh cells under UDDS and HWY driving cycles. The left three figures present the voltage, SOC, and distance profiles of 18-0 battery pack. The right three figures present profiles of 16-1 HESS pack. The red dashed lines represent SOC or voltage lower limits. These two packs are stopped because the terminal voltages of them touch the lower voltage limit as shown in the voltage curve figures. These figures depict that the all-electric range of the two systems are longer than the required 40 mile (64km) and the 18-0 battery pack has

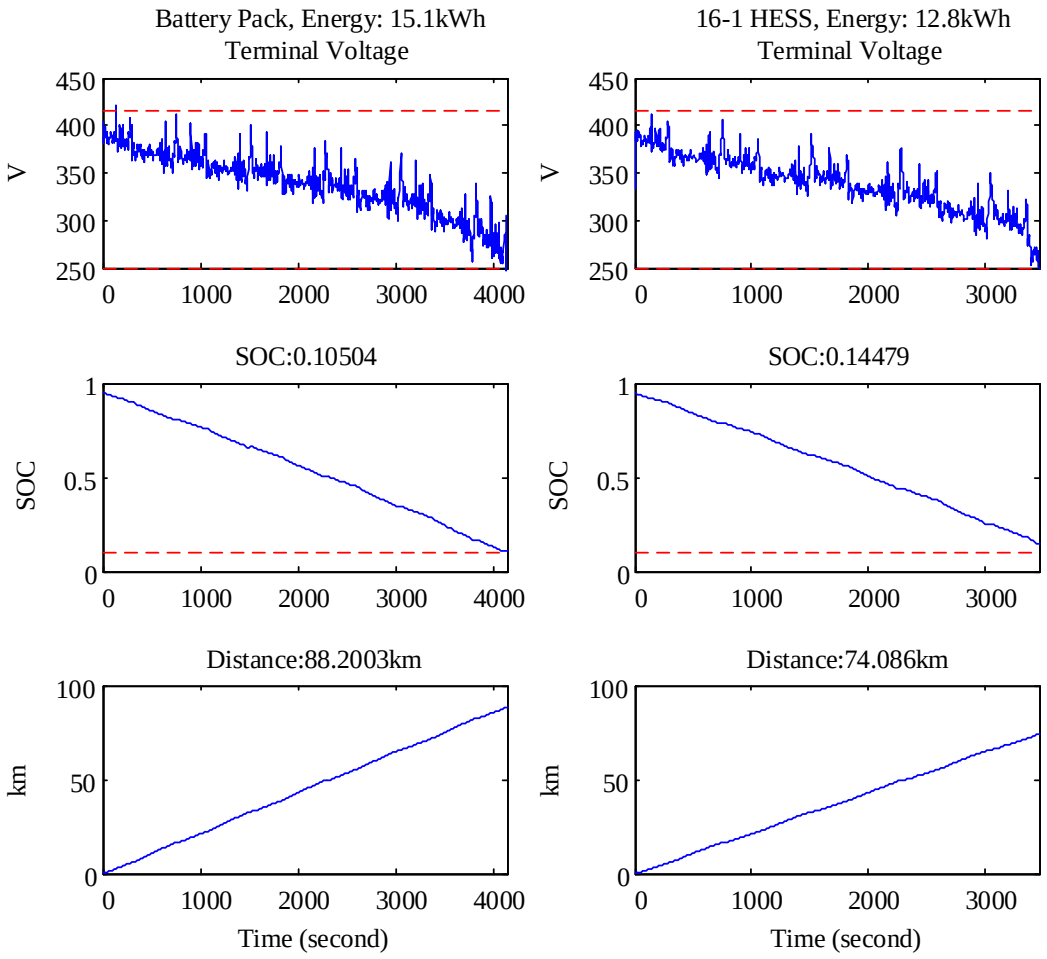

Figure 6.16: Results of 18-0 battery pack and 16-1 HESS pack with fresh battery cells under HWY driving cycle

a longer all-electric range than the 16-1 HESS pack due to more high energy density batteries and the oversized pack.

HESS pack shows the improvements in Fig. 6.17 and Fig. 6.18 when the battery cells are aged. From the fitted ohmic resistance of an aged battery cell in Fig. 5.19, the ohmic resistance is increased by 1.8 times. Owing to the high voltage drop on the high internal resistance, the terminal voltage of an aged battery achieves the lower voltage limit faster. The all-electric range suffers a sharp decrease. All-electric ranges of the battery pack under UDDS and HWY driving cycles are 13.4km and 38.7km, respectively. However, the 16-1 HESS pack can prolong all-electric ranges under UDDS and HWY to 37.5km and 46.5km, respectively. Details of the comparative analysis for the battery pack and 16-1 HESS pack are summarized in Table 6.8.

Table 6.8: Comparative analysis for the battery pack and 16-1 HESS pack

	Battery pack (fresh)	Battery pack (aged)	16-1 HESS pack (fresh)	16-1 HESS pack (aged)
Cost (USD)	14,256		13,508	
Weight (kg)	84.6		81.8	
Volume (L)	31.3		33.7	
Total energy (kWh)	16		14.3	
AER UDDS (km)	99.2	13.4	87.2	37.5
AER HWY (km)	88.2	38.7	74.1	46.5
Used energy UDDS (kWh)	15.2	2.1	13.4	5.7
Used energy HWY (kWh)	15.1	6.6	12.8	8.1

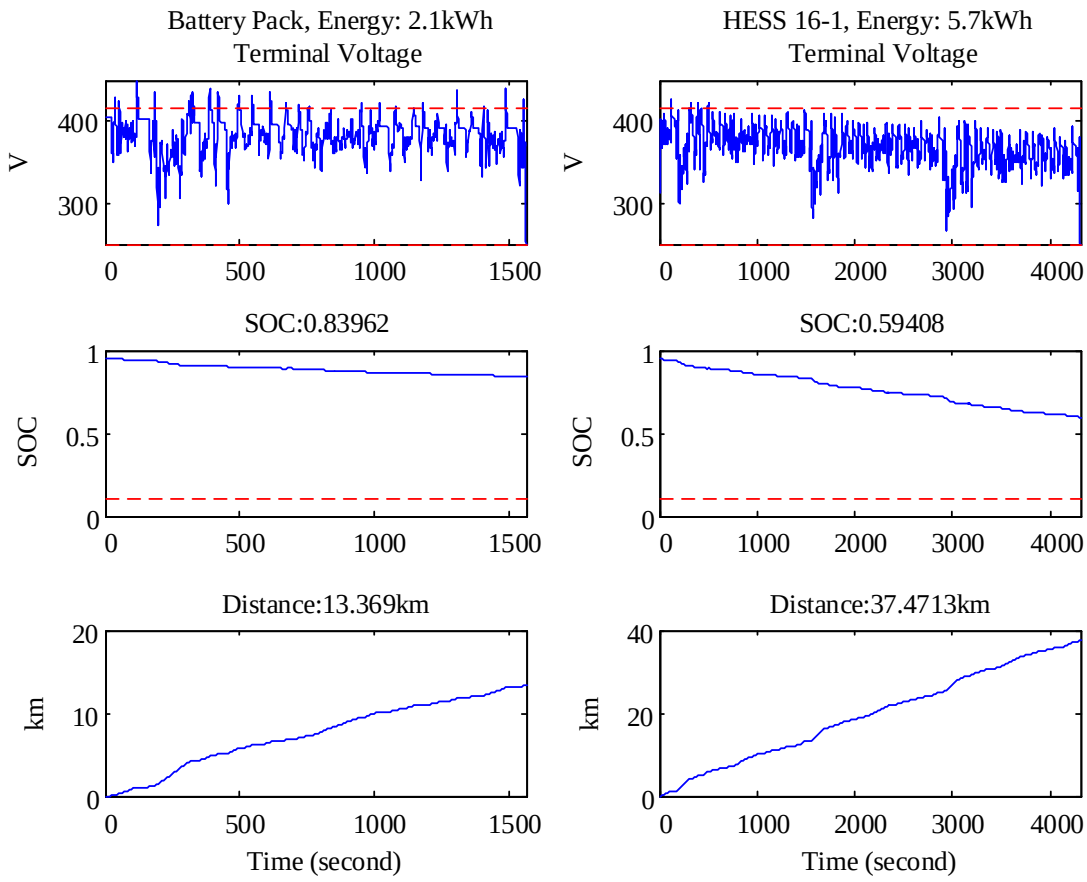

Figure 6.17: Results of 18-0 battery pack and 16-1 HESS pack with aged battery cells under UDDS driving cycle

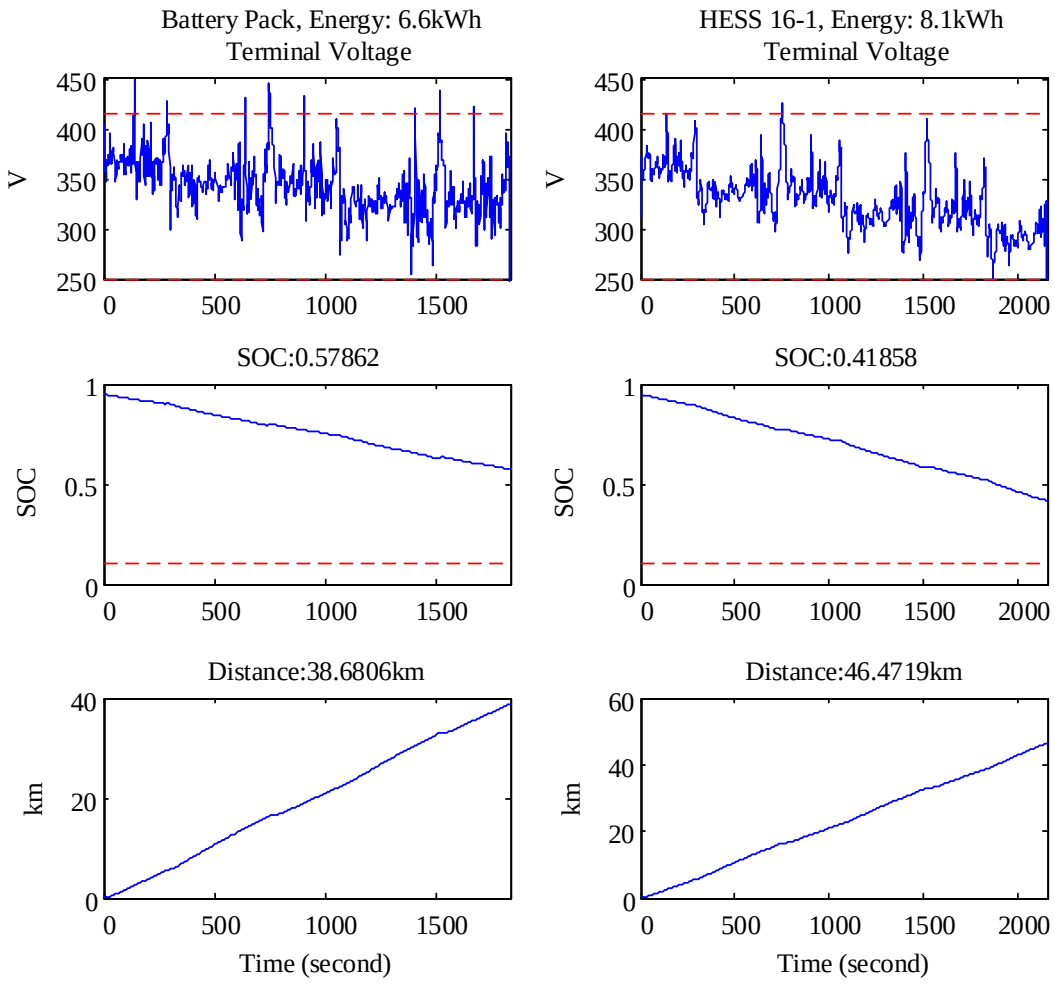

Figure 6.18: Results of 18-0 battery pack and 16-1 HESS pack with aged battery cells under HWY driving cycle

6.6 Conclusions

A direct coupled HESS pack design methodology was proposed and used in a case study to explore the replacement tradeoffs between battery and UC cells based on specifications on commonly available lithium-ion NMC 18650 cells and non-aqueous, symmetric UCs from Maxwell. A hybrid module design unit concept and a HESS pack design methodology were proposed that employed temperature dependent cell models from characterization data, simulated power capability and cold cranking responses from hypothetical hybrid module designs. USABC design guidelines for the PHEV-40, power-assist hybrid, and 48V hybrid vehicles were employed in the case study.

For the HESS packs in the PHEV-40 system that operate predominately at or above room temperature, UCs show potential to be viable as a replacement strategy. However, a case study design based on stricter low temperature requirements illustrate that significant improvements in terms of cost, weight, and volume are needed for the selected UC used in the analysis. For an energy storage system in a power-assist or 48V mild HEV system, the direct coupled hybrid modules show outperform features due to the low energy and high power targets for a mild HEV. Considering the specific power and specific energy, the 16-1 HESS pack for PHEV-40 design owns a high 2-second pulse specific power from $717 W/kg$ to $905 W/kg$ and a relatively high specific energy $185 Wh/kg$. This HESS pack is compared to other energy storage devices and USABC targets in the Ragone plot in Fig. 6.19. The case study presented can serve as an illustrative example; it can easily be repeated and generalized to other cell technologies and electrified vehicle applications.

For the PHEV-40 system design, the 18-0 battery pack and 16-1 HESS pack which

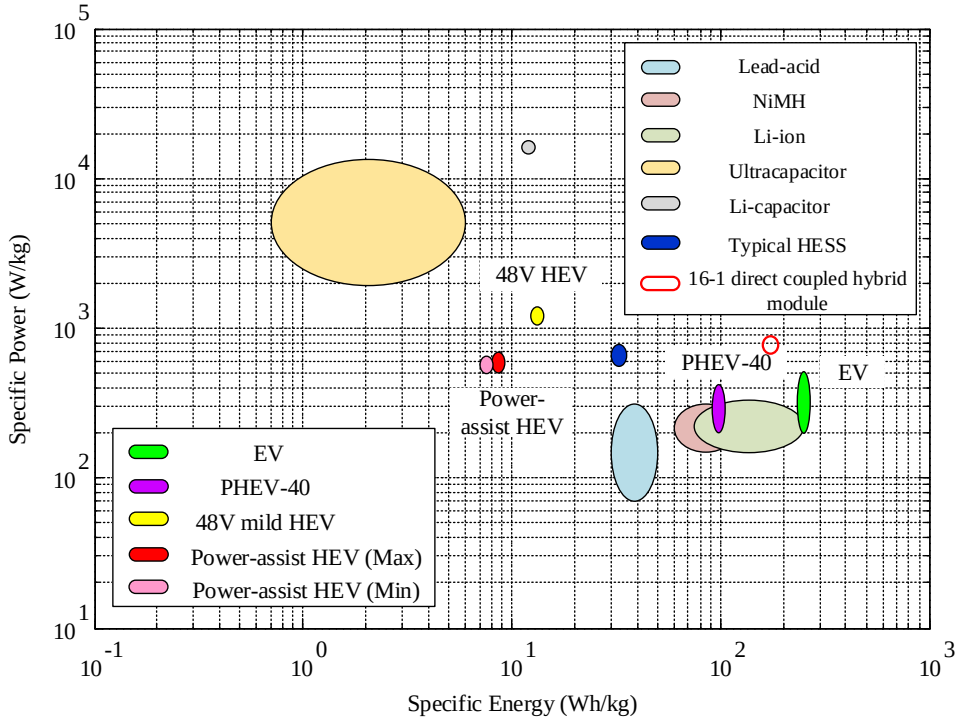

Figure 6.19: Ragone plot includes 1-16 HESS pack

have met the requirements at beginning of life are tested under UDDS and HWY with fresh and aged battery cells. With aged battery cells, the comparative test results indicate that the 16-1 HESS pack increases all-electric range 24.1km under UDDS and 7.8km under HWY, while the aged battery pack cannot meet the all-electric range goal. Therefore, the direct coupled HESS pack has potential to reduce the replacement cost of the energy storage system.

The scope of the case study in the section considered only the energy storage components of the pack. Practical aspects such as cost/complexity of cell/module balancing, thermal management, reliability, and safety will be explored and quantified in an improved cast study in the future.

Chapter 7

Conclusions and Future work

7.1 Conclusions

In this thesis, a physics-based single particle modeling is presented to analyze a proposed direct coupled hybrid energy storage module using lithium-ion battery and ultracapacitor.

A summary of the energy storage system in the electrified vehicles have been presented. Several energy storage elements and hybrid energy storage systems are compared to the performance targets of the energy storage systems in electric, hybrid electric, and plug-in hybrid electric vehicles. The Ragone plot Fig. 2.16 shows that the lithium-ion batteries are close to, or even exceed, the required specific energy of EV and PHEV but the specific power of them is just half of the required or less. For an energy storage system in HEV, a battery pack must be oversized to meet the high specific power requirements. Ultracapaciors and lithium-ion capacitors have outstanding specific power and become strong competitors for HEV but not for PHEV and EV owing to the poor specific energy. Typical hybrid energy storage systems have

not been widely used into commercial electrified vehicles because of the poor specific energy and complicated topologies.

Based on the performance of the 96 cells battery pack two-level balancing topologies analysis, balancing time, energy loss, effect on plug-in charge and component counts are evaluated. Balancing time and energy loss in two modes of F/F (synchronous fly-back topology for both module and pack level) with 6 modules and F/R (synchronous fly-back topology for module and ring shunting topology for pack level) with 6 modules outperform others. Compared with other mixed topologies, F/D (synchronous fly-back topology for module and dissipative shunting resistor topology for pack level) with 6 modules has the fastest balancing time. The passive balancing topology (dissipative shunting resistor topology for both module and pack level) and D/F (dissipative shunting resistor topology for module and synchronous fly-back topology for pack level) with 16 modules need less components compared to others.

The physics-based single particle modeling embedded with a solid-electrolyte interface growth model for a lithium-ion battery has been developed for battery management system. A novel parametrization method has been proposed which just needs to fit the diffusion coefficient of the positive electrode $D_{s,p}$, radius of the positive spherical particle $R_{s,p}$, reaction rate of the positive electrode k_p, and ohmic resistance R_f. According to the effects of the number of shells in a spherical particle analysis, a spherical particle with 20 shells has been used in the single particle model to obtain a high accuracy. The experimental results of an NCR18650A lithium-ion battery show an acceptable accuracy that the mean absolute error of the model can achieve 3.811mV under the UDDS driving cycle which is more accurate than the equivalent

circuit model (9.7874mV). Moreover, the SEI layer growth model has also been validated by aging experiments. Furthermore, the proposed SOC-SOH joint estimation algorithm based on the observable hybrid single particle model has been tested with a +5% initial SOC error and a 0.3Ω initial ohmic resistance. The estimation results show that the MAE of the estimated SOC is 0.43% and the MAE of the estimated ohmic resistance is $6m\Omega$.

Then the physics-based modeling has been applied to analyze the performance of the proposed direct coupled hybrid energy storage module topology based on the NCR18650A lithium-ion battery and Maxwell BCAP0350 ultracapacitor. There are many ways to directly connect battery cells and ultracapacitor cells in a module which would influence the performance of the module. The energy utilization of ultracapacitor in a module has 9 cells in a battery string and 14 cells in an ultracapacitor string can achieve 65% and outperform others. More ultracapacitor strings connected in parallel would increase the power density but reduce the energy density. For a direct coupled hybrid module has one battery string with 9 cells in series and five ultracapacitor strings with 14 ultracapacitor cells in series, the power density for 2-second pulse at 3.7V is $766W/kg$ and the energy density is just $31Wh/kg$. For a module has one battery string and one ultracapacitor string, the power density is $670W/kg$ and the energy density is $84Wh/kg$. Moreover, the simulation and experimental results of an one battery and two ultracapactors hybrid module indicate that the direct coupled hybrid modules can extend the operating range and slow the capacity fade of lithium-ion battery. The SOC-SOH joint estimation algorithm for the hybrid modules based on the physics-based modeling has also been developed. The MAE of the estimated SOC is 0.24% and the MAE of the estimated ohmic resistance is $13.4m\Omega$.

For the battery packs or the proposed direct coupled topologies, a pack design methodology has been proposed to meet U.S. Advanced Battery Consortium LLC PHEV-40, power-assist, and 48V HEV performance targets. In order to explore replacement tradeoffs between the battery and ultracapacitor, a case study of the direct coupled topologies has been presented. From the case study, ultracapacitors enhance the power capability for short term pulse power and marginally reduce the cost of an entire energy storage system, even though the energy specific cost ($\$/Wh$) of ultracapacitor is much higher than the lithium-ion battery. Considering the specific power and specific energy in a HESS pack, the 16-1 topology for the PHEV-40 design owns a high specific power for 2-second pulse from $717W/kg$ to $905W/kg$ and a relatively high specific energy $185Wh/kg$. In addition, the hybrid module topologies can keep a relatively long all-electric range when the batteries degrade. For the PHEV-40 system design, the 16-1 HESS pack with aged battery cells enables a vehicle to drive more 24.1km for UDDS and 7.8km for HWY than an 18-0 battery pack does. The direct coupled hybrid module shows the potential to reduce the replacement cost of the entire energy storage system.

7.2 Future work

In this thesis, the lithium-ion batteries and the ultracapacitors are used in the direct coupled hybrid module. Future work can attempt to use the lithium-ion capacitors to replace the ultracapacitors as the high power density energy storage device because the lithium-ion capacitors own higher specific power and specific energy than the ultracapacitors.

The effects of temperature on the battery and the battery in a hybrid module

could be considered. The physics-based model of a battery at different temperatures needs to be developed in terms of the variations of the parameters in the model.

In the single particle model, the diffusion equation in a spherical particle is solved by the even spaced discretization finite difference method. To reduce the order of the model and keep a relatively high accuracy, the uneven space discretization could be considered. Moreover, other reduced order models could be developed for the energy management system.

A tool box will be developed to analyze the performance of the direct couple hybrid module in terms of the current curve, voltage curve, SOC curve, and all-electric range. The tool box will have the capabilities to combine different energy storage devices together in the direct coupled topology and consider the aging effects on each energy storage devices.

Due to the high order of the single particle model, tuning the process matrix Q in EKF for the SOC and SOH estimation is a big challenge. An adaptive filter could be used to track the states of a battery.

For an energy storage system consists of the direct coupled hybrid modules, the balancing performance could be discussed. Moreover, the balancing circuits for the system need to be considered. Lithium-ion batteries and ultracapacitors are combined in a hybrid module, only one pack level balancing circuit is needed in the energy storage system to reduce the module to module differences. In a hybrid module, both of lithium-ion battery and ultracapacitor strings need balancing circuits.

Bibliography

Ahmed, R., Sayed, M. E., Arasaratnam, I., Tjong, J., and Habibi, S. (2014a). Reduced-order electrochemical model parameters identification and soc estimation for healthy and aged li-ion batteries part i: Parameterization model development for healthy batteries. *IEEE Trans. Emerg. Sel. Topics Power Electron.*, **2**(3), 659–677.

Ahmed, R., Sayed, M. E., Arasaratnam, I., Tjong, J., and Habibi, S. (2014b). Reduced-order electrochemical model parameters identification and state of charge estimation for healthy and aged li-ion batteries part ii: Aged battery model and state of charge estimation. *IEEE Trans. Emerg. Sel. Topics Power Electron.*, **2**(3), 678–690.

ALABC (2013). Do hybrid electric vehicles use lead-acid batteries? yes! here's why.

Baba, N., Yoshida, H., Nagaoka, M., Okuda, C., and Kawauchi, S. (2014). Numerical simulation of thermal behavior of lithium-ion secondary batteries using the enhanced single particle model. *Journal of Power Sources*, **252**, 214–228.

Baronti, F., Roncella, R., and Saletti, R. (2014). Performance comparison of active

balancing techniques for lithium-ion batteries. *Jounrnal of Power Sources*, **267**, 603–609.

Barsukov, Y. and Qian, J. (2013). *Battery Power Management For Portable Devices*. Artech House.

Bilgin, B., Magne, P., Malysz, P., Yang, Y., Pantelic, V., Preindl, M., Korobkine, A., Jiang, W., Lawford, M., and Emadi, A. (2015). Making the case for electrified transportation. *IEEE Trans. Transport. Electrific.*, **1**(1), 4 – 17.

Bonfiglio, C. and Roessler, W. (2009). A cost optimized battery management system with active cell balancing for lithium ion battery stacks. In *Vehicle Power and Propulsion Conference, 2009. VPPC '09. IEEE*, pages 304–309. IEEE.

Boovaragavan, V., Harinipriya, S., and Subramanian, V. R. (2008). Towards real-time (milliseconds) parameter estimation of lithium-ion batteries using reformulated physics-based models. *Journal of Power Sources*, **183**, 361–365.

Bradbury, K. (2010). Energy storage technology review. Technical report, Duke University.

Buchmann, I. (2011). *Batteries in a Portable World*, chapter 2. Cadex Electronics Inc., 3rd edition.

Cai, L. and White, R. E. (2009). Reduction of model order based on proper orthogonal decomposition for lithium-ion battery simulations. *Journal of The Electrochemical Society*, **156**(3), A154–A161.

Cao, J. and Emadi, A. (2011). A new battery/ultracapacitor hybrid energy storage

system for electric, hybrid, and plug-in hybrid electric vehicles. *IEEE Trans. Power Electron.*, **27**, 122–132.

Cao, J. and Emadi, A. (2012). A new battery/ultracapacitor hybrid energy storage system for electric, hybrid, and plug-in hybrid electric vehicles. *IEEE Trans. Power Electron.*, **27**(1), 122–132.

Cao, J., Schofield, N., and Emadi, A. (2008). Battery balancing methods: A comprehensive review. In *Vehicle Power and Propulsion Conference, 2008. VPPC '08. IEEE*, pages 1–6. IEEE.

Chaturvedi, N. A., Klein, R., Christensen, J., Ahmed, J., and Kojic, A. (2010). Algorithms for advanced battery-management systems. $IEEE_{MC}S, \mathbf{30}(3), 49--68$.

Corporation, L. T. (2013). *LTC3300-1 - High Efficiency Bidirectional Multicell Battery Balancer*. Linear Technology Corporation.

Dao, T.-S., Vyasarayani, C. P., and McPhee, J. (2012). Simplification and order reduction of lithium-ion battery model based on porous-electrode theory. *Journal of Power Sources*, **198**, 329–337.

Daowd, M., Omar, N., Van Den Bossche, P., and Van Mierlo, J. (2011). Passive and active battery balancing comparison based on matlab simulation. In *Vehicle Power and Propulsion Conference (VPPC), 2011 IEEE*, pages 1–7. IEEE.

Daowd, M., Antoine, M., Omar, N., Lataire, P., Bossche, P. V. D., and Mierlo, J. V. (2014). Battery management system-balancing modularization based on a single switched capacitor and bi-directional dc/dc converter with the auxiliary battery. *Energies*, **7**, 2897–2937.

Di Domenico, D., Pognant-Gros, P., Petit, M., and Creff, Y. (2015). State of health estimation for nca-c lithium-ion cells. In *Proc. ELSEVIER International Federation of Automatic Control Papers Online (IFAC'15)*, pages 376–382. ELSEVIER.

Domenico, D. D., Fiengo, G., and Stefanopoulou, A. (2008). Lithium-ion battery state of charge estimation with a kalman filter based on a electrochemical model. In *Control Applications, 2008. CCA 2008. IEEE International Conference on*, pages 702–707. IEEE.

Domenico, D. D., Stefanopoulou, A., and Fiengo, G. (2010). Lithium-ion battery state of charge and critical surface charge estimation using an electrochemical model-based extended kalman filter. *Journal of Dynamic Systems, Measurement, and Control*, **132**(6), 061302–1–061302–11.

Dougal, R., Liu, S., and White, R. E. (2002). Power and life extension of battery-ultracapacitor hybrids. *IEEE Trans. Compon. Packag. Technol.*, **25**, 120–131.

Doyle, M., Fuller, T. F., and Newman, J. (1993). Modeling of galvanostatic charge and discharge of the lithium/polymer/insertion cell. *Journal of The Electrochemical Society*, **140**(6), 1526–1533.

Doyle, M., Newman, J., Gozdz, A. S., Schmutz, C. N., and Tarascon, J. M. (1996). Comparison of modeling predictions with experimental data from plastic lithium ion cells. *Journal of The Electrochemical Society*, **143**(6), 1890–1903.

Ehsani, M., Gao, Y., and Emadi, A. (2009). *Modern electric, Hybrid Electric, and Fuel Cell Vehicles: Fundamentals, Theory, and Design*. CRC Press.

Einhorn, M., Roessler, W., and Fleig, J. (2011). Improved performance of serially connected li-ion batteries with active cell balancing in electric vehicles. *Vehicular Technology*, **60**(6), 2448–2457.

Elgowainy, A., Burnham, A., Wang, M., Molburg, J., and Rousseau, A. (2009). Well-to-wheels energy use and greenhouse gas emissions analysis of plug-in hybrid electric vehicles.

Emadi, A. (2011). Transportation 2.0. *IEEE Power Energy Mag.*, **9**(4), 18–29.

Emadi, A. (2014). *Advanced Electric Drive Vehicles*, chapter 7, pages 237–282. CRC Press, Boca Raton, FL. ISBN: 978-1-4665-9769-3.

EPA (1996). Federal test procedure revisions. [Online]. Available: https://www3.epa.gov/.

EPA (2016). Inventory of u.s. greenhouse gas emissions and sinks: 1900-2014.

Forman, J. C., Bashash, S., Stein, J. L., and Fathy, H. K. (2011). Reduction of an electrochemistry-based li-ion battery model via quasi-linearization and pad approximation. *Journal of The Electrochemical Society*, **158**(2), A93–A101.

Fuller, T. F., Doyle, M., and Newman, J. (1994). Simulation and optimization of the dual lithium ion insertion cell. *Journal of The Electrochemical Society*, **141**(1), 1–10.

German, J. (2015). Hybrid vehicles technology development and cost reduction. *International Council on Clean Transportation*, **1**, 1–18.

Govindaraj, A., King, M., and Lukic, A. M. (2010). Performance characterization and optimization of various circuit topologies to combine batteries and ultra-capacitors. In *IECON 2010 - 36th Annual Conference on IEEE Industrial Electronics Society*, pages 1850 – 1857. IEEE.

Gu, R., Malysz, P., Preindl, M., Yang, H., and Emadi, A. (2015a). Linear programming based design and analysis of battery pack balancing topologies. In *Proc. IEEE Transportation Electrification Conference and Expo (ITEC '15)*, pages 1 – 7, Dearborn.

Gu, R., Malysz, P., and Emadi, A. (2015b). A novel battery/ ultracapacitor hybrid energy storage system analysis based on physics-based lithium-ion battery modeling. In *Proc. IEEE Transportation Electrification Conference and Expo (ITEC '15)*, pages 1 – 6, Dearborn.

Gu, R., Malysz, P., Wang, D., Wang, W., Yang, H., and Emadi, A. (2016a). On the design of a direct cell coupled hybrid energy storage system for plug-in hybrid electric vehicles. In *Proc. IEEE Transportation Electrification Conference and Expo (ITEC '16)*, pages 1 – 8, Dearborn.

Gu, R., Malysz, P., Yang, H., and Emadi, A. (2016b). On the suitability of physics-based modeling for lithium-ion batteries. *IEEE Trans. Transport. Electrific.* submitted for publication.

Gully, A., Liu, H., Srinivasan, S., Sethurajan, A. K., Schougaard, S., and Protas, B. (2014). Effective transport properties of porous electrochemical materials - a homogenization approach. *Journal of The Electrochemical Society*, **161**(8), E3066–E3077.

Guo, M., Sikha, G., and Whitea, R. E. (2011). Single-particle model for a lithium-ion cell: Thermal behavior. *Journal of The Electrochemical Society*, **158**(2), A122–A132.

Han, H., Xu, H., Yuan, Z., and Zhao, Y. (2014). Modeling for lithium-ion battery used in electric vehicles. In *Transportation Electrification Asia-Pacific (ITEC Asia-Pacific), 2014 IEEE Conference and Expo*, pages 1 – 5. IEEE.

He, H., Xiong, R., and Fan, J. (2011). Evaluation of lithium-ion battery equivalent circuit models for state of charge estimation by an experimental approach. *Energies*, **4**(4), 582–598.

Hu, X., Li, S., and Peng, H. (2012). A comparative study of equivalent circuit models for li-ion batteries. *Journal of power sources*, **198**, 359–367.

Hutchinson, T., Burgess, S., and Hermann, G. (2014). Current hybrid-electric powertrain architectures: Applying empirical design data to life cycle assessment and whole-life cost analysis. *Applied Eenrgy*, **119**, 314–329.

Jacobsen, T. and West, K. (1995). Diffusion impedance in planar, cylindrical and spherical symmetry. *Electrochimica Acta*, **40**(2), 255–262.

Kalman, R. E. *et al.* (1960). A new approach to linear filtering and prediction problems. *Journal of basic Engineering*, **82**(1), 35–45.

Kemper, P. and Kum, D. (2013). Extended single particle model of li-ion batteries towards high current applications. In *Vehicle Power and Propulsion Conference (VPPC), 2013 IEEE*, pages 1 – 6. IEEE.

Khaligh, A. and Li, Z. (2010). Battery, ultracapacitor, fuel cell, and hybrid energy storage systems for electric, hybrid electric, fuel cell, and plug-in hybrid electric vehicles: State of the art. $IEEE_{JV}T, \mathbf{59}(6), 2806 - -2814$.

Khaligh, A., Cao, J., and Lee, Y. (2009). A multiple-input dcdc converter topology. *IEEE Trans. Power Electron.*, **24**, 862–868.

Kochhan, R., Fuchs, S., Reuter, B., Burda, P., Matz, S., and Lienkamp, M. (2014). An overview of costs for vehicle components, fuels and greenhouse gas emissions.

Lee, T., Kim, Y., Stefanopoulou, A., and Filipi, Z. S. (2011). Hybrid electric vehicle supervisory control design reflecting estimated lithium-ion battery electrochemical dynamics. In *American Control Conference (ACC), 2011*, pages 388–395. IEEE.

Lee, Y.-S. and Cheng, M.-W. (2005). Intelligent control battery equalization for series connected lithium-ion battery strings. *Industrial Electronics, IEEE Transactions on*, **52**(5), 1297–1307.

Leea, J. L., Chemistruckb, A., and Plett, G. L. (2012a). Discrete-time realization of transcendental impedance models, with application to modeling spherical solid diffusion. *Journal of Power Sources*, **206**, 367–377.

Leea, J. L., Chemistruckb, A., and Plett, G. L. (2012b). One-dimensional physics-based reduced-order model of lithium-ion dynamics. *Journal of Power Sources*, **220**, 430–448.

Li, Z., Onar, O., Khaligh, A., and Schaltz, E. (2009). Design, control, and power management of a battery/ultra-capacitor hybrid system for small electric vehicles. In *Proc. SAE World Congress and Exhxhibition*, Detroit, MI. 2009-01-1387.

Lin, X., Park, J., Liu, L., Lee, Y., Sastry, A. M., and Lu, W. (2013). A comprehensive capacity fade model and analysis for li-ion batteries. *Journal of The Electrochemical Society*, **160**(10), A1701–A1710.

Lukic, S. M., Wirasingha, S. G., Rodriguez, F., Cao, J., and Emadi, A. (2006). Power management of an ultracapacitor/battery hybrid energy storage system in an hev. In *Proc. IEEE Vehicle Power and Propulsion Conference (VPPC '06)*, pages 1 – 6, Windsor.

Lukic, S. M., Cao, J., Bansal, R. C., Rodriguez, F., and Emadi, A. (2008). Energy storage systems for automotive applications. *IEEE Trans. Ind. Electron.*, **55**(6), 2258–2267.

Malysz, P., Gu, R., Ye, J., Yang, H., and Emadi, A. (2016). State-of-charge and state-of-health estimation with state constraints and current sensor bias correction for electrified powertrain vehicle batteries. *IET Electrical Systems in Transportation*, pages 1–9.

Manla, E., Mandic, G., and Nasiri, A. (2011). Testing and modeling of lithium-ion ultracapacitors. In *2011 IEEE Energy Conversion Congress and Exposition*, pages 2957–2962. IEEE.

Mathworks (1998). *Linear Programming Solver*. The MathWorks, Inc. MATLAB R2012b.

Maxwell (2013). Bc series ultracapacitors datasheet. 1017105.4.

Metz, B., Davidson, O., Bosch, P., Dave, R., and Meyer, L., editors (2007). *Contribution of Working Group III to the Fourth Assessment Report of the Intergovernmental Panel on Climate Change*, chapter 5. Cambridge University Press.

Mohan, S., Kim, Y., and Stefanopoulou, A. G. (2015). Estimating the power capability of li-ion batteries using informationally partitioned estimators. *IEEE Trans. Control Syst. Technol.*, **11**(99), 1–12.

Muenzel, V., Hollenkamp, A. F., Bhatt, A. I., de Hoog, J., Brazil, M., Thomas, D. A., and Mareels, I. (2015). Comment on a comparative testing study of commercial 18650-format lithium-ion battery cells [j. electrochem. soc., 162, a1592 (2015)]. *Journal of The Electrochemical Society*, **162**(12), Y11–Y12.

Najmabadi, A. (2013). Evaluation of active balancing algorithms and an improved method for a deployed active battery balancer as well as physical implementation.

Narayanaswamy, S., Steinhoust, S., Lukasiewycz, M., Kauer, M., and Chakraborty, S. (2014). Optimal dimensioning of active cell balancing architectures. In *Design, Automation and Test in Europe Conference and Exhibition (DATE)*, pages 1–6, Dresden. IEEE.

Newman, J. and Tiedemann, W. (1975). Porous-electrode theory with battery applications. *AIChE J.*, **21**(1), 25–41.

Ning, G., White, R. E., and Popov, B. N. (2006). A generalized cycle life model of rechargeable li-ion batteries. *Electrochimica Acta*, **51**(10), 2012–2022.

Nishijima, K., Sakamoto, H., and Harada, K. (2000). A pwm controlled simple and

high performance battery balancing system. In *Power Electronics Specialists Conference, 2000. PESC 00. 2000 IEEE 31st Annual (Volume:1)*, pages 517–520, Galway. IEEE.

Omar, N., Daowd, M., Hegazy, O., Sakka, M. A., coosemans, T., den Bossche, P. V., and Mierlo, J. V. (2012). Assessment of lithium-ion capacitor for using in battery electric vehicle and hybrid electric vehicle applications. *Electrochimica Acta*, **86**, 305–315.

Onar, O. and Khaligh, A. (2008). Dynamic modeling and control of a cascaded active battery/ultra-capacitor based vehicular power system. In *Proc. IEEE Vehicle Power and Propulsion Conference (VPPC '08)*, pages 1 – 4, Harbin.

Ortuzar, M., Moreno, J., and Dixon, J. (2007). Ultracapacitor-based auxiliary energy system for an electric vehicle: Implementation and evaluation. *IEEE Trans. Ind. Electron.*, **54**, 2147–2156.

Ostadi, A. and Kazerani, M. (2014). Optimal sizing of the battery unit in a plug-in electric vehicle. *IEEE Trans. Veh. Technol.*, **63**(7), 30773084.

Panasonic (2012). Ncr18650a data sheet. Version 13.11 R1.

Pattipati, B., Sankavaram, C., and Pattipati, K. R. (2011). System identification and estimation framework for pivotal automotive battery management system characteristics. *Systems, Man, and Cybernetics, Part C: Applications and Reviews, IEEE Trans. on*, **41**(6), 869 – 884.

Pei, L., Zhu, C., Wang, T., Lu, R., and Chan, C. (2014). Online peak power prediction based on a parameter and state estimator for lithium-ion batteries in electric vehicles. *Eenrgy*, **66**(1), 766–778.

Plett, G. L. (2004). Extended kalman filtering for battery management systems of lipb-based hev battery packs: Part 2. modeling and identification. *Journal of power sources*, **134**(2), 262–276.

Prasad, G. K. and Rahn, C. D. (2012). Development of a first principles equivalent circuit model for a lithium ion battery. In *ASME Dynamic Systems and Control Conference, 2012*, pages 1–7. ASME.

Preindl, M., Danielson, C., and Borrelli, F. (2013). Performance evaluation of battery balancing hardware. In *Control Conference (ECC), 2013 European*, pages 4065–4070. IEEE.

Rahimian, S. K., Rayman, S., and White, R. E. (2013). Extension of physics-based single particle model for higher chargedischarge rates. *Journal of Power Sources*, **224**, 180–194.

Rahn, C. D. and Wang, C.-Y. (2013). *Battery Systems Engineering*. Wiley. ISBN: 978-1-119-97950-0.

Ramadass, P., Haran, B., Gomadam, P. M., White, R., and Popov, B. N. (2004). Development of first principles capacity fade model for li-ion cells. *Journal of The Electrochemical Society*, **151**(2), A196–A203.

Ramadesigan, V., Northrop, P. W. C., De, S., Braatz, S. S. R. D., and Subramanian,

V. R. (2012). Modeling and simulation of lithium-ion batteries from a systems engineering perspective. *Journal of The Electrochemical Society*, **159**, R31–R45.

Rawlinson, P. D. (2012). Vehicle battery pack ballistic shield.

Rawlinson, P. D. (2014). Integration system for a vehicle battery pack.

Ronasmans, J. and Lalande, B. (2015). Combining energy with power: Lithium-ion capacitors. In *Proc. IEEE Electrical Systems for Aircraft, Railway, Ship Propulsion and Road Vehicles (ESARS '15)*, pages 1 – 4, Aachen.

Safari, M., Morcrette, M., Teyssot, A., and Delacourt, C. (2009). Multimodal physics-bsed aging model for life prediction of li-ion batteries. *Journal of The Electrochemical Society*, **156**(3), A145–A153.

Santhanagopalan, S. and White, R. E. (2006). Online estimation of the state of charge of a lithium ion cell. *Journal of Power Sources*, **161**, 1346–1355.

Seaman, A., Dao, T.-S., and McPhee, J. (2014). A survey of mathematics-based equivalent-circuit and electrochemical battery models for hybrid and electric vehicle simulation. *Journal of Power Sources*, **256**, 410–423.

Shi, L. and Crow, M. L. (2008). Comparison of ultracapacitor electric circuit models. In *Power and Energy Society General Meeting - Conversion and Delivery of Electrical Energy in the 21st Century, 2008 IEEE*, pages 1 – 6. IEEE.

Simpson, A. and Markel, T. (2006). Cost-benefit analysis of plug-in hybridelectric vehicle technology. In *22nd International Electric Vehicle Symposium*. National Renewable Energy Laboratory.

Smith, K. A., Rahn, C. D., and Wang, C.-Y. (2007). Control oriented 1d electrochemical model of lithium ion battery. *Energy conversion and Management*, **48**, 2565–2578.

Smith, K. A., Rahn, C. D., and Wang, C.-Y. (2008). Model order reduction of 1d diffusion systems via residue grouping. *Journal of Dynamic System, Measurement, and Control*, **130**(1), 011012–1–8.

Solero, L., Lidozzi, A., and Pomilio, J. A. (2005). Design of multiple-input power converter for hybrid vehicles. *IEEE Trans. Power Electron.*, **20**, 1007–1016.

Straubel, J., Berdichevsky, E., Lyons, D., Colson, T., Eberhard, M., Wright, I., and Ferber, R. (2007). Method and apparatus for mounting, cooling, connecting and protecting batteries.

Subramanian, V. R., Diwakar, V. D., and Tapriyalv, D. (2005). Efficient macro-micro scale coupled modeling of batteries. *Journal of The Electrochemical Society*, **152**(10), A2002–A2008.

Subramanian, V. R., Boovaragavan, V., and Diwakar, V. D. (2007). Toward real-time simulation of physics based lithium-ion battery models. *Electrochemical and Solid-State Letters*, **10**(11), A255–A260.

Subramanian, V. R., Boovaragavan, V., Ramadesigan, V., and Arabandi, M. (2009). Mathematical model reformulation for lithium-ion battery simulations: Galvanostatic boundary conditions. *Journal of The Electrochemical Society*, **156**(4), A260–A271.

Tao, Y. and Li, Z. (2014). Study on modeling and application of ultracapacitor. In *Advanced Research and Technology in Industry Applications (WARTIA), 2014 IEEE Workshop on*, pages 999–1002. IEEE.

Tu, C. and Emadi, A. (2012). A novel series-parallel reconfigurable hybrid energy storage system for electrified vehicles. In *Proc. IEEE Transportation Electrification Conference and Expo (VPPC '12)*, pages 1 – 4, Dearborn, MI.

USABC (2002). *FreedomCAR Energy Storage System Performance Goals for Power-Assist Hybrid Electric Vehicles*. FreedomCAR.

USABC (2003). *FreedomCAR battery test manual for power-assist hybrid electric vehiles*. FreedomCAR.

USABC (2014a). *Battery Test Manual For Plug-In Hybrid Electric Vehicles*. U.S. Department of Energy. version 3.

USABC (2014b). *USABC Goals for Advanced Batteries for 12V Start Stop Vehicle Applications*. United States Council for Automotive Research LLC.

USABC (2014c). *USABC Goals for Advanced Batteries for 48V Hybrid Electric Vehicle Applications*. United States Council for Automotive Research LLC.

USABC (2014d). *USABC Goals for Advanced Batteries for PHEVs for FY 2018 to 2020 Commercialization*. United States Council for Automotive Research LLC.

USABC (2015). *USABC Goals for Advanced Batteries for EVs - CY 2020 Commercialization*. United States Council for Automotive Research LLC.

Vellucci, F., Pede, G., DAnnibale, F., Mariani, A., Roncella, R., Saletti, R., Baronti, F., and Fantechi, G. (2013). Development and realization of lithium-ion battery modules for starting applications and traction of off-road electric vehicles. In *Electric Vehicle Symposium and Exhibition (EVS27), 2013 World*, pages 1 – 10. IEEE.

Welch, G. and Bishop, G. (2006). State estimation for linear and non-linear equality-constrained systems. *Citesseer*, **7**, 1–16.

Yan, J., Cheng, Z., Xu, G., Qian, H., and Xu, Y. (2010). Fuzzy control for battery equalization based on state of charge. In *Vehicular Technology Conference Fall (VTC 2010-Fall), 2010 IEEE 72nd*, pages 1–7. IEEE.

Yun, J., Yeo, T., and Park, J. (2013). High efficiency active cell balancing circuit with soft-switching technique for series-connected battery string. In *Applied Power Electronics Conference and Exposition (APEC)*, pages 3301–3304. IEEE.